UNIVERSITY OF KWAZULU-NATAL

LIDAR and satellite observation of aerosols and clouds over South Africa

By

Lerato David Shikwambana
212562477

A thesis submitted in partial fulfilment of the requirements for the degree of Doctor of Philosophy

College of Agriculture, Engineering and Science
School of Chemistry and Physics,
University of KwaZulu-Natal

Supervisor: Prof. Venkataraman Sivakumar

August, 2017

PREFACE

This research was motivated by the lack of reporting of aerosols and clouds in South Africa. The work described by this thesis was carried out at the University of KwaZulu-Natal and the Council for Scientific and Industrial Research from September 2012 until August 2017, under the supervision of Professor Venkataraman Sivakumar.

This work has resulted in three publications which form part of the thesis in Chapters 4, 5 and 6. Chapter 4 has already been published: *Lerato Shikwambana and Venkataraman Sivakumar, "Observation of Clouds Using the CSIR Transportable LIDAR: A Case Study over Durban, South Africa," Advances in Meteorology, vol. 2016, Article ID 4184512, 9 pages, 2016. doi:10.1155/2016/4184512*, whereas Chapters 5 and 6 are still under review. The work has also resulted in five peer reviewed conference proceedings.

I encountered a few challenges in this research both in data collection and in data analysis. However, this process has made me strong and has helped me build my confidence.

I hope you enjoy your reading like I enjoyed preparing this.

Lerato Shikwambana

Durban, August, 2017.

DECLARATION 1 - PLAGIARISM

I **LERATO DAVID SHIKWAMBANA** declare that:

(i) The research reported in this thesis, except where otherwise indicated, is my original research.

(ii) This thesis has not been submitted for any degree or examination at any other university.

(iii) This thesis does not contain other persons' data, pictures, graphs or other information, unless specifically acknowledged as being sourced from other persons.

(iv) This thesis does not contain other persons' writing, unless specifically acknowledged as being sourced from other researchers. Where other written sources have been quoted, then:

a) their words have been re-written but the general information attributed to them has been referenced;

b) where their exact words have been used, their writing has been placed inside quotation marks, and referenced.

(v) Where I have reproduced a publication of which I am author, co-author or editor, I have indicated in detail which part of the publication was actually written by myself alone and have fully referenced such publications.

(vi) This thesis does not contain text, graphics or tables copied and pasted from the Internet, unless specifically acknowledged, and the source being detailed in the thesis and in the References sections.

Signed:

DECLARATION 2 - PUBLICATIONS

DETAILS OF CONTRIBUTION TO PUBLICATIONS that form part and/or include research presented in this thesis (include publications in preparation, submitted, in press and published and give details of the contributions of each author to the experimental work and writing of each publication)

Publication 1

- Lerato Shikwambana and Venkataraman Sivakumar, "*Observation of Clouds Using the CSIR Transportable LIDAR: A Case Study over Durban, South Africa*," Advances in Meteorology, vol. 2016, Article ID 4184512, 9 pages, 2016. doi:10.1155/2016/4184512 (Impact factor 1.107)

Publication 2

- Lerato Shikwambana and Venkataraman Sivakumar, "*Investigation of various aerosols over different locations in South Africa using satellite, model simulation and LIDAR*", Meteorological Applications, 2017. (Revised and Submitted).

Publication 3

- Lerato Shikwambana and Venkataraman Sivakumar, "*Long-range transport of volcanic aerosols over South Africa: A case study of the Calbuco volcano eruption in April 2015*", South African Geographical Journal, 2017. (Submitted, still under review).
-

Signed:

ARTICLES IN PEER-REVIEWED NATIONAL/INTERNATIONAL CONFERENCE PROCEEDINGS

- **Lerato Shikwambana**, Venkataraman Sivakumar, *Estimates of the aerosol optical depth over Pretoria using the CSIR mobile LIDAR.* 29th Annual conference of South African Society for Atmospheric Sciences, ISBN 978 0 620 56626 1, 26-27 September 2013, Durban, South Africa, 153 - 155.
- **Lerato Shikwambana**, Venkataraman Sivakumar, *Aerosol optical depth measurements over Pretoria using CSIR LIDAR and sun-photometer: A case study*, ISBN 978-0-620-62777-1, 30th Annual conference of South African Society for Atmospheric Sciences, 01-02 October 2014, POTCHEFSTROOM, South Africa, 138-141.
- **Lerato Shikwambana**, Venkataraman Sivakumar, *Campaign measurements in the North West Province using the CSIR mobile LIDAR*, ISBN: 978-0-620-63067-2, Proceedings of the 10th International Conference of AARSE, University of Johannesburg, South Africa October 2014, 75-83.
- **Lerato Shikwambana**, Venkataraman Sivakumar, *Five year climatological trends of AOD over coastal and inland towns of South Africa retrieved by MODIS*, ISBN: 978-0-620-67825-4, 31st Annual conference of South African Society for Atmospheric Sciences, 21 - 22 September 2015, Hennops River Valley, South Africa, 57 – 60.
- Venkataraman. Sivakumar, Jeremiah A. Ogunniyi, Joseph A. Adesina, Priyanka. Singh and **Lerato. Shikwambana**, *A new 2-D Scan portable Durban LiDAR for atmospheric studies – System Description and first scientific result*, ISBN: 978-0-620-67825-4, 31st Annual conference of South African Society for Atmospheric Sciences, 21 - 22 September 2015, Hennops River Valley, South Africa, 17 – 19.

Signed:

ACKNOWLEDGEMENTS

I would like to thank the following people for their sincere support and encouragement in making this work possible:

1. Prof. Sivakumar Venkataraman, S*upervisor,* University of KwaZulu Natal, for his vast knowledge of the subject and guidance throughout the duration of this project. I would also like to thank him for his patience and also availing himself to help me.

2. Dr. Paul Motalane, *Mentor*, Council for Scientific and Industrial Research (CSIR), for his support since day one until present on this current work. I would also like to thank him for introducing me to this subject as I am thoroughly enjoying it.

3. Mr. Henk van Wyk, C*hief technician,* Council for Scientific and Industrial Research (CSIR) National Laser Centre, for his expertise on the LIDAR system. I thank him that he made sure that the system was always operating flawlessly.

4. Mr. Ameeth Sharma, *Engineer*, Council for Scientific and Industrial Research (CSIR) National Laser Centre, for teaching me about the system and availing himself whenever I had technical problems with the system.

5. The Council for Scientific and Industrial Research (CSIR) National Laser Centre, for the opportunity given to me to conduct my research in that organisation. I thank them for the support given to me both technically and financially.

7. The National Research Foundation (NRF) for their financial support.

DEDICATIONS

I would like to dedicate this thesis to my wife Boitumelo Shikwambana and to my children Tintswalo and Tiyani Shikwambana. I am very grateful for their support and endurance.

I would also like to dedicate this thesis to my parents Andrew “Malombo” and Flora Shikwambana for their support, and to my sister, Tinyiko Shikwambana, who took interest in my work and supported me.

ABSTRACT

An increase in anthropogenic emission can affect the global climate change. Clouds may warm or cool the atmosphere depending on their microphysical properties and heights; and these properties are subject to changes due to cloud – aerosol interactions. Therefore understanding the altitude and optical characteristics of clouds becomes very important. In this study, we present the result obtained for studying aerosol and cloud over South Africa (SA) using different satellite, ground-based (LIDAR) and model observations.

Campaign measurements were carried out in Durban (29.9° S, 30.9° E) to study the low altitude clouds. Low level clouds were observed on 20 – 22 November 2012 and high level clouds were observed on 23 November 2012. The measured optical depth showed a high variability for 20 and 21 November 2012. This indicates a change in the composition and/or thickness of the cloud. For 22 and 23 November 2012 almost similar values of optical depth were observed. Cloud-Aerosol Lidar and Infrared Pathfinder Satellite Observations (CALIPSO) revealed high level clouds while the Council for Scientific and Industrial Research (CSIR) Light Detection And Ranging (LIDAR) could not.

Later, the Goddard Chemistry Aerosol Radiation and Transport (GOCART) model was used to study the black carbon and sulfates, over different locations in SA. The GOCART model showed that sulfates contributed the most in Lephalale, Potchefstroom, Bloemhof, Mafikeng, Rustenburg and Vryburg with black carbon (BC) also having some contributions. The GOCART model also indicated that there was no significant change in the sulfate AOD from 2004 to 2007. The highest sulfate AOD was observed in the summer season while the lowest sulfate AOD was observed in the winter season. Based on the extreme change in AOD in Lephalale a case study using the CSIR mobile LIDAR was carried out. The LIDAR showed a consistent layer of aerosol every morning at altitudes of ~4 km. The Hybrid Single-Particle Lagrangian Integrated Trajectory (HYSPLIT) model suggested that the 3000 m air masses might have transported dust to the area. However, CALIPSO confirmed

that the measurements by the CSIR mobile LIDAR were aerosols and that those aerosols could be classified as polluted dust and smoke. The major contributor to the smoke could be from the coal fired power station in the area.

Finally, we also report on the long range transport of volcanic aerosols over South Africa. A large amount of sulphur dioxide (SO_2) aerosols was observed over South Africa (SA) during April 2015. This study was carried out to explain the origin and/or contribution to such an increase. It is known that SO_2 is a by-product of any volcanic eruption, so we investigate the possible transport of SO_2 from the Calbuco volcano eruption, which occurred in 22 April 2015, over SA using models and satellite data. On 22 April 2015, the Hybrid Single Particle Lagrangian Integrated Trajectory (HYSPLIT) model forward trajectory revealed air masses leaving Calbuco at a height of 12000 m and travelling over SA on 28 April 2015 at a height of 8000 m. The extinction coefficient profile and total backscatter height-time-colour map from the CALIPSO also confirmed the presence of aerosols at a height of 8 km on 28 April 2015. The vertical feature mask and aerosol type from CALIPSO were used to classify the particles as a mixture of cloud and aerosols polluted dust which corresponds with presence of SO_2. The time averaged maps of SO_2 and aerosols optical depth (AOD) from Ozone Monitoring Instrument (OMI) and Moderate Resolution Imaging Spectroradiometer (MODIS) respectively, showed SO_2 and AOD leaving Calbuco and arriving in SA. There is a strong possibility that the cause to the increase in SO_2 over SA is due to the long-range transport of SO_2 from the Calbuco volcanic eruption.

TABLE OF CONTENT

Chapter 1

Introduction and statement problem

1.1 Introduction

South Africa is a developing country with a vast number of economic activities which include mining, agriculture and food processing, service industry, manufacturing, tourism and financial services. Although some sectors like mining, manufacturing and service industry are crucial to the economy of the country they contribute proportionally towards air pollution. In the last twenty years the growth of the economy in South Africa has also led to an increase in the number of vehicles on the road which also contributes towards air pollution.

The South African National Environmental Management: Air Quality Act 20 of 2014 defines “air pollution" as any change in the composition of the air caused by smoke, soot, dust (including fly ash), cinders, solid particles of any kind, gases, fumes, aerosols and odorous substances. Air pollution has impacts in the;

(i) Environment: Ground-level ozone damages vegetation, including crops, flowers, shrubs and forests.
(ii) Climate change: An increase in the emission of greenhouse gases, traps more heat and leads to an increase in average temperatures around the world.
(iii) Human health: Fine particulate matter ($PM_{2.5}$) and ground-level ozone (O_3) can affect human respiratory and cardiovascular systems.
(iv) Economy: The health effects from $PM_{2.5}$ and ground-level ozone can reduce work attendance and overall participation in the labour force.

The World Health Organisation (WHO) stated that the pollutants of major public health concern include particulate matter; carbon monoxide (CO), ozone, nitrogen dioxide (NO_2) and sulfur dioxide (SO_2).

Particulate matter (PM) is a broad term used to describe the fine particles found in the atmosphere, including soil dust, dirt, soot, smoke, pollen, ash, aerosols and liquid droplets. PM_{10} particles are larger than 2.5 μm and smaller than 10 μm in diameter, these are usually inhalable coarse particles. $PM_{2.5}$ describes particulate matter that is 2.5 μm in diameter and smaller.

CO is a deadly, colourless, odourless, poisonous gas. CO can cause harmful health effects by reducing oxygen delivery to the body's organs (like the heart and brain) and tissues.

NO_2 is a highly reactive gas that is formed when fuel is burned at high temperatures. The reaction of NO_2 and water results in the formation of nitric acid which may contribute to acid rain. Some effects of low levels of NO_2 include nausea, slight cough and mild fatigue. However, high NO_2 concentrations can lead to abdominal pains, sever coughing and shortness of breath.

SO_2 is a toxic gas with a rotten smell that enters the atmosphere as a result of natural phenomena (such as volcanic eruption) and anthropogenic activities (such as biomass burning). SO_2 affects human health when it is inhaled; it irritates the nose, throat, and airways to cause coughing, wheezing and shortness of breath. Long term exposure to SO_2 can results in respiratory effects including bronchoconstriction and increased asthma symptoms.

Different parts of South Africa (SA) have various concentrations of PM, CO, SO_2, and NO_2 depending on the economic activities occurring in those areas. As an example Fig. 1.1 shows the PM_{10} concentrations between 2013 and 2014 of two stations situated in Middleburg (red) and Camden (blue) both in the Mpumalanga province in SA. The two stations show a similar trend throughout the year but Camden station has a higher concentration compared to the Middelburg station.

It is well known that aerosols have a major impact on the climate, human health and environment. It is therefore important to monitor the levels of these aerosols as to prevent them from reaching levels of toxicity. SA as a developing country has witnessed an increase in industrial activities which leads to an increase in the production of aerosols. It is for these reasons why it is important to study the

distribution of aerosols in SA. Several authors have reported on various aerosols studies in SA such as biomass burning aerosols (Aurela et al, 2016; Tesfaye et al, 2014), dust aerosols (Tesfaye et al, 2015) and PM (Hersey et al, 2015) to name a few. However, in this work the main aim is to study the distributions of aerosols in SA using LIDAR, satellite and models. Equally as important is to study aerosols being transported into SA. There are limited reports on clouds studies in SA using LIDAR. This study will help in understanding clouds optical properties using LIDAR and satellite observations.

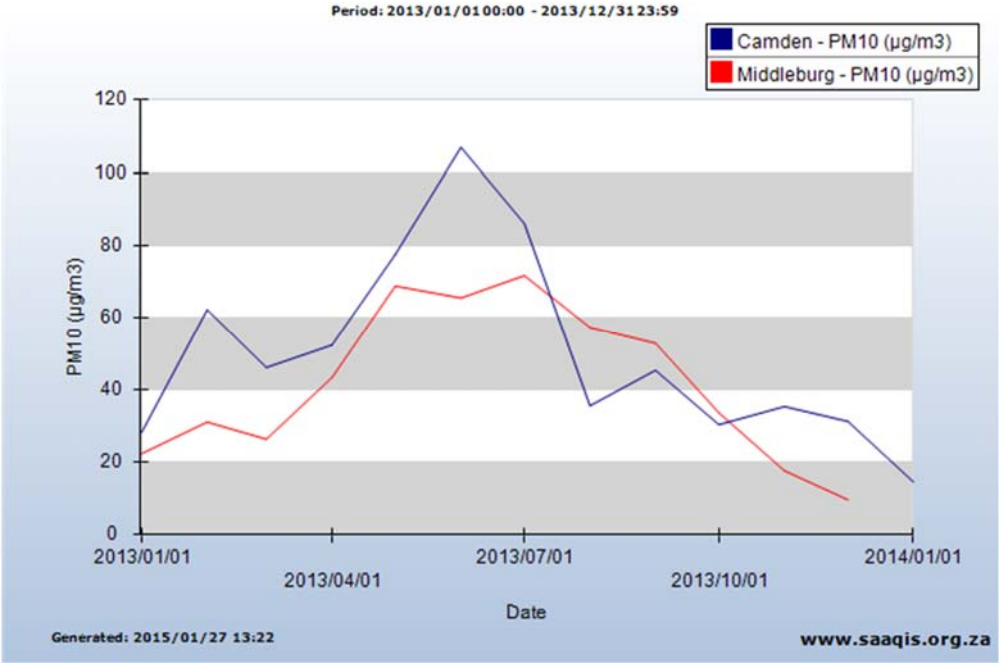

Fig. 1.1: Monthly averaged PM_{10} concentration from 2013 to 2014 in the Camden and Middleburg stations (http://www.saaqis.org.za, date accessed on 08/03/2017).

1.2 Problem statement

Climate change is a topical subject in both developed and developing countries because the consequences of it include melting ice and rising sea, extreme weather and a risk in human health which affects the whole globe. It is for these reasons

that scientists from all over the world have taken a decision to study the causes and impacts of this phenomenon.

Africa is vulnerable to climate change because of the lack of resources needed to deal with the effects that come with it. Climate change in Africa is not only a conservation problem but is a socio-economic issue that must be dealt with at a global scale (Case, 2006). Therefore it is important that Africa be better prepared to deal with the consequences of climate change and better policies be put in place. Water availability and food security are the crucial factors that already affect Africa but it is anticipated that climate change will elevate the situation further.

South Africa, like any other country, is affected and contributes towards climate change. The South African government "acknowledges and regards climate change as one of the greatest threats to sustainable development" – COP17/ CMP7. From the COP17/CMP7confernce held in South Africa in 2011, the South African government has committed to address climate change on a national level by:

- Mapping a socio-economic transition to a climate-resilient and low-carbon economy and society;
- Limiting the global temperature increase to below 2°C above pre-industrial levels;
- Making sure that the greenhouse gas emissions stop growing at the latest by 2020-2025, stabilize for up to ten years, and then decline in absolute terms.

To insure that this commitment set out by the South African government come to pass, direct and indirect ways of monitoring and observation of the atmosphere must be placed for action.

1.3 Key research objectives

There are three main objectives of this thesis which have been answered in chapters 4, 5 and 6. The objectives are listed below:

1. The main objective of chapter 4 is to study the optical properties of clouds using LIDAR and satellite.
2. Chapter 5 focused to study the aerosol optical characteristics and distribution of various aerosols in South Africa. This study will be carried out using LIDAR, satellite data and models.
3. The objective of chapter 6 is to study aerosols being transported into South Africa. A case study of the Calbuco volcano eruption was carried out to illustrate the transport of aerosols from one continent to another.

Reference

Aurela M., Beukes J.P., Van Zyl P., Vakkari V., Teinilä K., Saarikoski S., Vakkari V., Teinilä K., Saarikoski S., Laakso L., 2016. The composition of ambient and fresh biomass burning aerosols at a savannah site, South Africa. South African Journal of Science 112, 8 pages. http://dx.doi.org/10.17159/ sajs.2016/20150223

Case M., 2006. Climate Change Impacts on East Africa: A Review of the Scientific Literature, WWF-World Wide Fund for Nature, 1-12.

Hersey S. P., Garland R. M., Crosbie E., Shingler T., Sorooshian A., Piketh S., Burger R., 2015. An overview of regional and local characteristics of aerosols in South Africa using satellite, ground, and modeling data, Atmospheric Chemistry and Physics 15, 4259–4278.

Tesfaye M., Botai J. Sivakumar V., Tsidu G. M., 2014. Simulation of biomass burning aerosols mass distributions and their direct and semi-direct effects over South Africa using a regional climate model. Meteorology and Atmospheric Physics, 125, 177–195.

Tesfaye M., Tsidu G. M., Botai J., Sivakumar V., de W Rautenbach C. J., 2015. Mineral dust aerosol distributions, its direct and semi-direct effects over South Africa based on regional climate model simulation. Journal of Arid Environments, 114, 22-40.

Chapter 2

Background

2.1 Structure of the atmosphere

Generally, the word atmosphere defined as “the envelope of gases surrounding the earth or another planet”. The Earth’s atmosphere is retained by gravity and its main purpose is to protect the life on earth by absorbing ultraviolet solar radiation. The atmosphere is divided into four layers according to major changes in temperature, density and pressure (see Fig 2.1).

The troposphere is the atmospheric layer closest to the planet and contains the largest percentage of the mass of the total atmosphere. It contains 99 % of the water vapor and aerosols in the atmosphere. Water vapor is important because its major role is in regulating air temperature by absorbing solar energy and thermal radiation from the planet's surface. The trapping of solar energy and thermal radiation results in the warming of the planet popularly known as global warming. A small amount of carbon dioxide is also found in the troposphere. Like water vapour, carbon dioxide also absorbs solar energy and thermal radiation and prevents its release into space. A steady decrease in temperature with an increasing height is observed in the troposphere. However, there is a critical height called the tropopause where the temperature starts to increase with increasing height. The tropopause is characterized by an abrupt change in lapse rate from a decreasing temperature with height to neutral or constant or increasing temperature with height.

The stratosphere is the region of the atmosphere where most of the ozone is found. Ozone is a trioxygen (O_3) inorganic unstable molecule formed by the reaction of dioxygen (O_2) with ultraviolet light and is presented in low concentrations throughout the Earth's atmosphere. The ozone layer (as it is commonly known) is very important to life on earth because it absorbs some of the harmful ultraviolet radiation emitted by the sun. However, it has been discovered that the ozone is

depleting as a result of anthropogenic pollutants (Sivasakthivel and Reddy, 2011). Chlorofluorocarbons (CFCs) are responsible for the breaking down of ozone. (Sivasakthivel and Reddy, 2011). When the CFCs are in the stratosphere the ultraviolet radiation breaks them down to release chlorine. These free chlorine atoms rip oxygen atoms off the ozone, leaving ordinary oxygen gas.

$$Cl + O_3 \rightarrow ClO + O_2$$

Free oxygen atom (O_1) will break apart the chlorine monoxide, releasing the chlorine atom back into the stratosphere to degrade more ozone.

$$ClO + O_1 \rightarrow O_2 + Cl$$

Some effects of ozone depletion include an increase in skin cancer, an increase in cataracts and sun burning, and cooling of the earth's stratosphere and possibly some surface climatic effect.

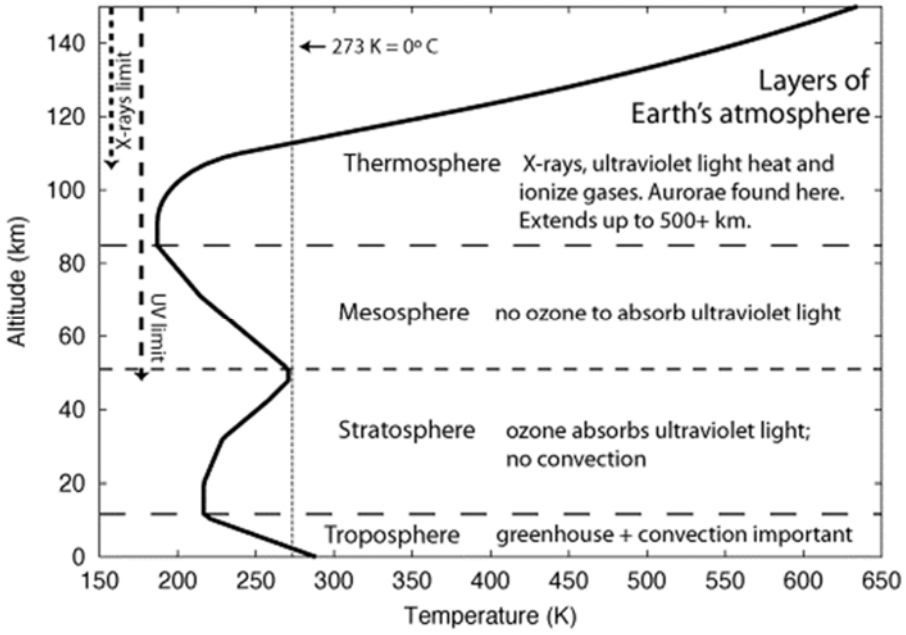

Fig. 2.1: Height profile of atmospheric temperature (obtained from a Standard model atmosphere from Steven Pietrobon at Small World Communications; http://www.astronomynotes.com/solarsys/s3c.htm, date accessed on 08/03/2017).

The mesosphere (meaning middle sphere) is characterized by decreasing temperatures, which may reach 190-180 K at an altitude of 80 km. The mesosphere is the coldest of the atmospheric layers. In this region, concentrations of ozone and water vapour are negligible. The mesosphere is also the layer in which a lot of meteors burn up while entering the earth's atmosphere.

The thermosphere has a low air density and comprises of high temperatures. The solar activity influences the temperature in the thermosphere. High-energy solar photons also tear electrons away from gas particles in the thermosphere, creating electrically-charged ions of atoms and molecules. Moving ions, dragged along by collisions with the electrically neutral gases, produce powerful electrical currents in some parts of the thermosphere.

2.2 Atmospheric aerosols

The main focus in this work is to study the distribution of aerosols in different parts of South Africa. It is therefore important that we introduce the theory of aerosols and explain the different types of aerosol parameters. In this section, we shall provide more in detail as it may form basis for the results presented in the Chapters 4, 5 and 6.

2.2.1 Definition of Aerosols

Atmospheric aerosols are solid or liquid particles suspended in the air with particle diameters in the range of 10^{-9}–10^{-4} m (Pöschl, 2005). They differ greatly in chemical composition, amount and distribution in space and time, and how long they persist in the atmosphere. Atmospheric aerosols can be divided into two types; primary aerosols and secondary aerosols. Primary aerosols are particulates that are emitted directly into the atmosphere. Examples of such particulates are sea-salt, soil dust, volcanic dust, smoke, soot and some organics. Secondary aerosols are particulates that are formed in the atmosphere by gas-to-particles conversion processes. Examples of such particulates are the sulfates, nitrates and some organics. From the definitions of primary and secondary aerosols it is clear

that origins of aerosols are both natural and anthropogenic. However, both the natural and anthropogenic aerosols have similar properties. Atmospheric aerosols main physical properties are that:

(i) they can absorb or scatter emitted electromagnetic radiation,
(ii) they can act as cloud nuclei.

The main chemical property of the atmospheric aerosols is that they act as medium upon which chemical reactions can occur.

Atmospheric aerosols can be classified by their particle size, chemical deposition, geographical location as well as location in the atmosphere. Aerosol particles can be classified by their diameter as either fine mode ($d < 2.5\mu m$) and coarse mode ($d > 2.5\mu m$). The fine mode can further be divided into the nuclei mode ($0.005\mu m < d < 0.1\mu m$), and the accumulation mode ($0.1\mu m < d < 2.5\mu m$). Fig. 2.2 illustrates the production, growth, transport and removal of atmospheric aerosols in the atmosphere. It can be seen that nucleation of gas molecules leads to the production of ultrafine aerosols. These ultrafine aerosols grow by the process of coagulation and condensation and are called accumulation aerosols. These aerosols are then taken up by cloud droplets and removed from the atmosphere as rainout. Coarse particles emitted by wind action are similarly removed by rainout.

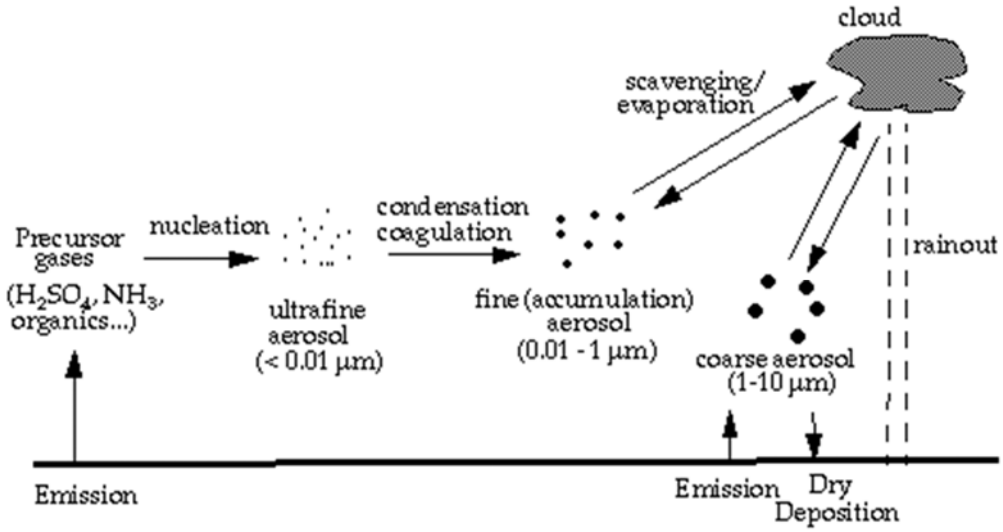

Fig. 2.2: Production, growth, and removal of atmospheric aerosols (Obtained from http://acmg.seas.harvard.edu/people/faculty/djj/book/bookchap8.html, date accessed on 08/03/2017)

Aerosols also vary according to their geographical location hence we may find them in marine, continental, rural, industrial, polar and desert aerosols. Aerosols also differ according to their location in the atmosphere, for example, stratosphere and troposphere have different types of aerosols.

2.2.2 Effects of atmospheric aerosols

Atmospheric aerosols have a direct and indirect effect in the globe. The direct effects of aerosols are seen in the environment, climate, human health and atmospheric visibility to name a few. One of the main environmental impacts have observed PM2.5 particles settling in water which in turn results in an increase in the acidity of streams and lakes. This in turn leads to the death of fish populations. (http://www.socaar.utoronto.ca/about/FAQ.htm, *date accessed on 08/03/2017)*. Particulate matter also contributes to acid deposition which contributes to vegetation damage, corrosion and nutrient depletion in soil. Particulate matter has also been reported to cause damage to local ecosystems (https://www.unece.org/fileadmin/DAM/env/documents/2013/air/wge/CEH_IMPACT_ENGLISH_single_page_website.pdf, *date accessed on 08/03/2017)*.

Aerosols influence the climate and weather in two ways; through aerosol direct effects and aerosol indirect effects. They have an effect on the energy balance of the atmosphere either by directly scattering and absorbing radiation, by serving as condensation nuclei during cloud formation, and by influencing precipitation (http://www.esrl.noaa.gov/research/themes/aerosols/, date accessed on 08/03/2017); IPCC, 2001).

Different types of aerosols have different effects on the human health. However, what is common to all the effects is that they may result in death. Fine mode particles are particularly dangerous when it comes down to human health. These particles are invasive and can penetrate the vital organs in humans. This in turn can lead to the damage of that particular organ which may result in death. For example, fine mode particles such as Sulphur dioxide affect human health when it is inhaled; it irritates the nose, throat, and airways to cause coughing, wheezing and shortness of breath. Long term exposure of SO_2 can results in respiratory effects including bronchoconstriction and increased asthma symptoms.

Atmospheric visibility is defined as the greatest distance in a given direction at which an object can be visually identified with unaided eyes (Lee et al, 2005). Visibility is determined by the mass and size distribution of aerosols in the air. It is important in many sectors especially in transport. All forms of transport such as air, rail, road and sea are affected heavily by atmospheric visibility. For aviation visibility is important for take-off and landing, for trains, cars and ships visibility is also of great importance as a clear view of the way head is necessary. However, atmospheric visibility is impaired by aerosols such as haze, smoke and fog. Visibility impairments have been observed in mega urban cities such as Delhi in India (Tiwari et al, 2011; Singh and Dey, 2012), Beijing in China (Zhou et al, 2012) and Kaohsiung City in Taiwan (Lee et al, 2005).

2.3 Scattering Theory

In the context of this work scattering can be described as a physical process caused by a deviation of radiation from a straight trajectory by one or more paths due to localized non-uniformities in the medium through which they pass. There

are many types of light scattering such as Rayleigh, Mie, Raman, Brillouin and Tyndall. However, for this work only the Rayleigh and Mie scattering processes will be discussed. Based on the dimensionless size parameter, the models of light scattering can be divided into three domains; β is then defined as (http://en.wikipedia.org/wiki/Scattering, *date accessed on 08/03/2017*)

$$\beta = \pi D_p / \lambda \tag{2.1}$$

where πD_p is the circumference of a particle and λ is the wavelength of the incident radiation. Based on the value of β, these domains are:

$\beta \ll 1$: Rayleigh scattering (small particle compared to wavelength of light);

$\beta \approx 1$: Mie scattering (particle about the same size as wavelength of light, valid only for spheres);

$\beta \gg 1$: geometric scattering (particle much larger than wavelength of light).

2.3.1 Rayleigh scattering

Rayleigh scattering is an elastic scattering process of electromagnetic radiation by particles with dimensions much smaller than the wavelength of the radiation. The sizes of atmospheric molecules are much smaller than the wavelengths of solar radiation and this result in Rayleigh scattering. In the Rayleigh scattering approximation, a molecule is considered as an individual dipole.

If we consider a small spherical particle that is homogeneous with size smaller than the wavelength of incident radiation $\vec{E}_0$, and we let $\vec{P}_0$ be the induced dipole moment, then from the classical electromagnetic theory we have

$$\vec{P}_0 = \alpha \vec{E}_0 \tag{2.2}$$

where α is the polarizability of the particle.

The scattered electric field at the large distance r (called far field scattering) from the dipole is given by

$$\vec{E} = \frac{1}{c^2}\frac{1}{r}\frac{\partial^2 \vec{P}}{\partial t^2}\sin(\gamma) \tag{2.3}$$

where c is the velocity of the radiation in the medium, γ is the angle between the scattered dipole moment $\vec{P}$ and the direction of observation, an illustration is shown in Fig 2.3

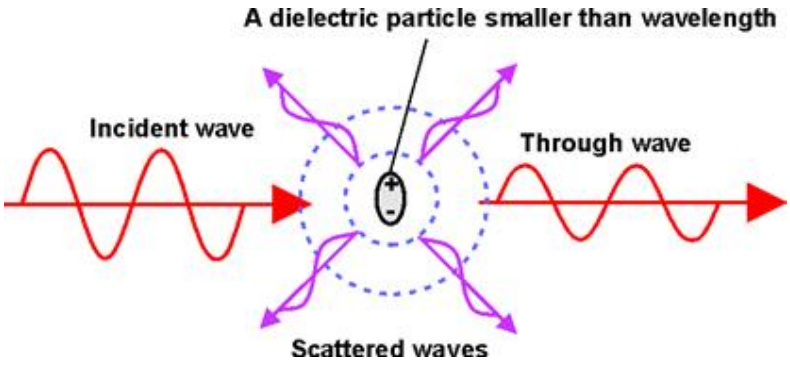

Fig 2.3: Illustration of Rayleigh scattering effect (http://www.invocom.et.put.poznan.pl/~invocom/C/P1-9/swiatlowody_en/p1-1_2_2.htm), date accessed on 10/08/2017).

In oscillating periodic field, the dipole moment is given in terms of induced dipole moment by

$$\vec{P} = \vec{P}_0 \exp\left(-ik\left(r - ct\right)\right) \tag{2.4}$$

and thus the electrical field is

$$\vec{E} = -\vec{E}_0 \frac{\exp\left(-ik\left(r - ct\right)\right)}{r} k^2 \alpha \sin(\gamma). \tag{2.5}$$

Decomposing the electrical vector on two orthogonal components perpendicular and parallel to the plane of scattering (a plane containing the incident and scattering beams) (see Fig 2.4) gives

$$E_r = -E_{0r} \frac{\exp\left(-ik\left(r - ct\right)\right)}{r} k^2 \alpha \sin(\gamma_1) \tag{2.6}$$

$$E_l = -E_{0l} \frac{\exp\left(-ik\left(r - ct\right)\right)}{r} k^2 \alpha \sin(\gamma_2). \tag{2.7}$$

$$\gamma_1 = \frac{\pi}{2}; \gamma_2 = \frac{\pi}{2} - \Theta$$

where $\Theta = 0^o$ is called forward scattering and $\Theta = 180^o$ is called backscattering.

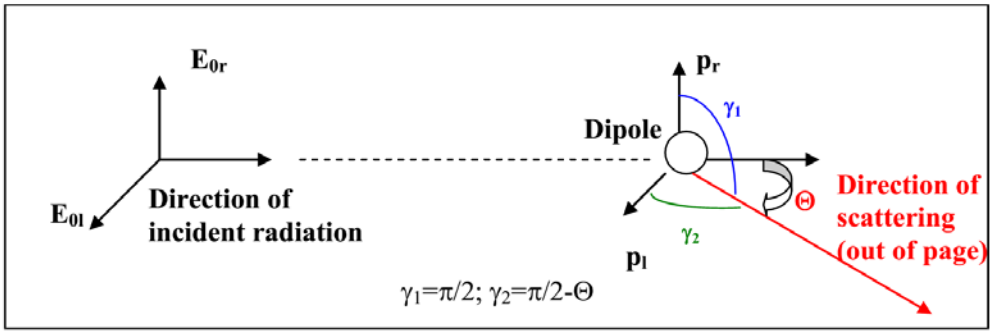

Fig 2.4: Illustration of plane containing the incident beam and scattered beam in the direction of observation, (http://irina.eas.gatech.edu/EAS8803_Fall2009/Lec14.pdf, date accessed 10/08/2017).

Using that

$$I = \frac{1}{\Delta\Omega}\frac{c}{4\pi}|E|^2, \tag{2.8}$$

where $\Delta\Omega$ is the solid angle, then the perpendicular and parallel intensities are

$$I_r = \frac{I_{0r}k^4\alpha^2}{r^2} \tag{2.9}$$

$$I_l = \frac{I_{0l}k^4\alpha^2\cos^2(\Theta)}{r^2}. \tag{2.10}$$

Assuming that the natural light (incident beam) is not polarized $(I_{0r} = I_{0l} = I_0/2)$ and that $k = 2\pi/\lambda$, then

$$I = I_r + I_l = \frac{I_0}{r^2}\alpha^2\left(\frac{2\pi}{\lambda}\right)^4\frac{1+\cos^2\Theta}{2}. \tag{2.11}$$

Equation (2.11) gives the intensity scattered by molecules (Rayleigh scattering) for unpolarized incident light.

2.3.2 Mie scattering

Mie scattering, like Rayleigh scattering, is an elastic process however Mie scattering applies to particles that have a diameter similar to or larger than the wavelength of the incident light.

Lorentz in 1890 and Mie in 1908 developed the theory to describe the scattering of light by aerosols. However, this theory can only be applied to spherical or ellipsoid particles. The Mie theory solves Maxwell's equations for electromagnetic (EM) fields within a dielectric sphere in terms of the algebric expansion in spherical harmonics and Bessel functions. The angular characteristics of Mie scattering for all particles and sizes and wavelengths are expressed in two intensity distribution functions i_1 and i_2. The light scattered by a particle at an observational angle of θ may be treated as consisting of two components, which are polarized perpendicular and parallel to the plane of polarization of the incident EM. The intensity functions depend on the size parameter, α , the refractive index, m , and the angle θ. They are calculated from an infinite series and given by

$$i_1 = \left| \sum_{n=1}^{\infty} \frac{2n+1}{n(n+1)} \left[a_n \pi_n(\cos\theta) + b_n \tau_n(\cos\theta) \right] \right|^2 \tag{2.12}$$

$$i_2 = \left| \sum_{n=1}^{\infty} \frac{2n+1}{n(n+1)} \left[a_n \tau_n(\cos\theta) + b_n \pi_n(\cos\theta) \right] \right|^2 \tag{2.13}$$

where a_n and b_n are complex functions given as

$$a_n = \frac{\Psi_n(\alpha)\Psi_n'(m\alpha) - m\Psi_n(m\alpha)\Psi_n'(\alpha)}{\xi(\alpha)\Psi_n(m\alpha) - m\Psi_n(m\alpha)\xi_n(\alpha)} \tag{2.14}$$

$$b_n = \frac{m\Psi_n(\alpha)\Psi_n'(m\alpha) - \Psi_n(m\alpha)\Psi_n'(\alpha)}{m\xi(\alpha)\Psi_n'(m\alpha) - \Psi_n(m\alpha)\xi(\alpha)} \tag{2.15}$$

ψ and ζ are the Ricatti-Bessel functions, they are defined in terms of the half-integer-order Bessel function of the first kind

(http://plaza.ufl.edu/dwhahn/Rayleigh%20and%20Mie%20Light%20Scattering.pdf, *date accessed on 10/08/2017).*

When a particle is illuminated by unpolarised light represented by two electric vectors of equal magnitude perpendicular and parallel to the plane of observation but having no coherent relationship (see Fig. 2.5), the scatter light consists of two incoherent components given as

$$I(\theta) = E\frac{\lambda^2}{4\pi^2}\left(\frac{i_1 + i_2}{2}\right) \tag{2.16}$$

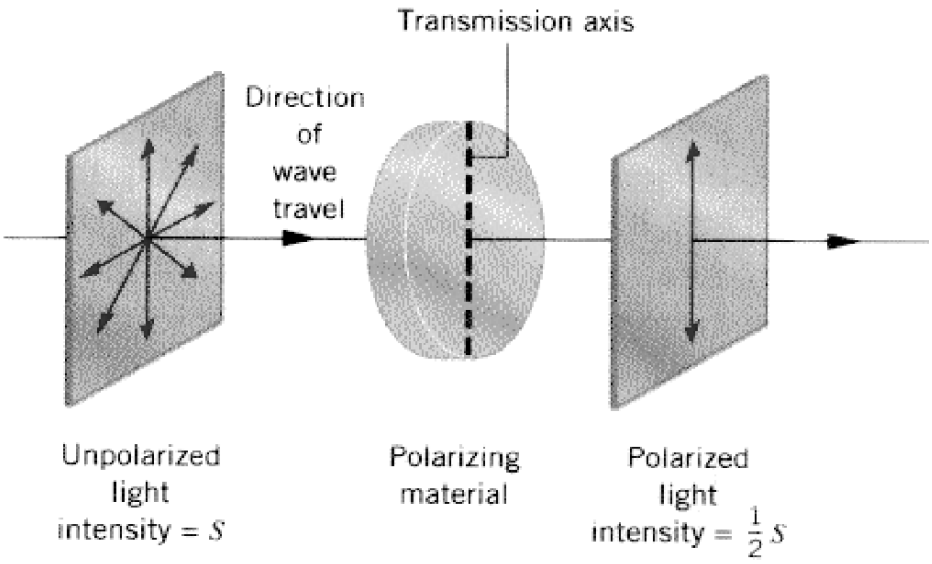

Fig 2.5: Illustration of an unpolarized light on linear polarizer (http://www.phys.hawaii.edu/~morse/P272fall10-23_pdf.pdf, date accessed 10/08/2017).

For Rayleigh scattering we can obtain the angular scattering coefficient as

$$\sigma_p(\theta) = \frac{I(\theta)}{E_0} = \frac{\lambda^2}{4\pi^2}\left(\frac{i_1 + i_2}{2}\right). \tag{2.17}$$

The total scattering coefficient is then obtained by integrating the above equation by 4π steradians.

$$\sigma_p = \frac{\lambda^2}{4\pi}\int_0^{\pi}(i_1 + i_2)\sin\theta d\theta \tag{2.18}$$

The above equation is usually represented in terms of a_n and b_n as

$$\sigma_p = \frac{\lambda^2}{2\pi}\sum_{n=1}^{\infty}(2n+1)\left(|a_n|^2 + |b_n|^2\right) \tag{2.19}$$

(Hahn, 2009; http://plaza.ufl.edu/dwhahn/Rayleigh%20and%20Mie%20Light%20Scattering.pdf, *date accessed 10/08/2017*).

2.4 Aerosols optical properties

2.4.1 Size distribution

The information of aerosol size distribution is important for understanding the physical processes relating to the studies in weather, climate, atmospheric electricity, air pollution and aerosol physics. Aerosol size distributions can also help to understand how atmospheric aerosol particles evolve under the influence of processes such as nucleation, coagulation, and condensational growth (Chan and Mozurkewich, 2007). The size distribution of aerosols is often found to be a log-normal distribution (Fig. 2.6). The important properties of aerosols, which are related to the size distribution, include the number, surface area and the mass of particles (Mahowald et al, 2014). There are different techniques that can be used to measure size distribution. Mobility size particle spectrometers have been used for observations of atmospheric particle number size distributions in the sub-micrometer diameter range. Depending on the instrument, mobility particle size spectrometers cover diameter ranges from 3 to 800 nm for regular atmospheric observations (Wiedensohler et al, 2012). These spectrometers are commonly known as the differential mobility particle sizers (DMPS). The DMPS system extracts small mobility electrical increments from the sample air using a differential mobility analyser and transfers it to a condensation particle counter (Dal Maso et al, 2005).

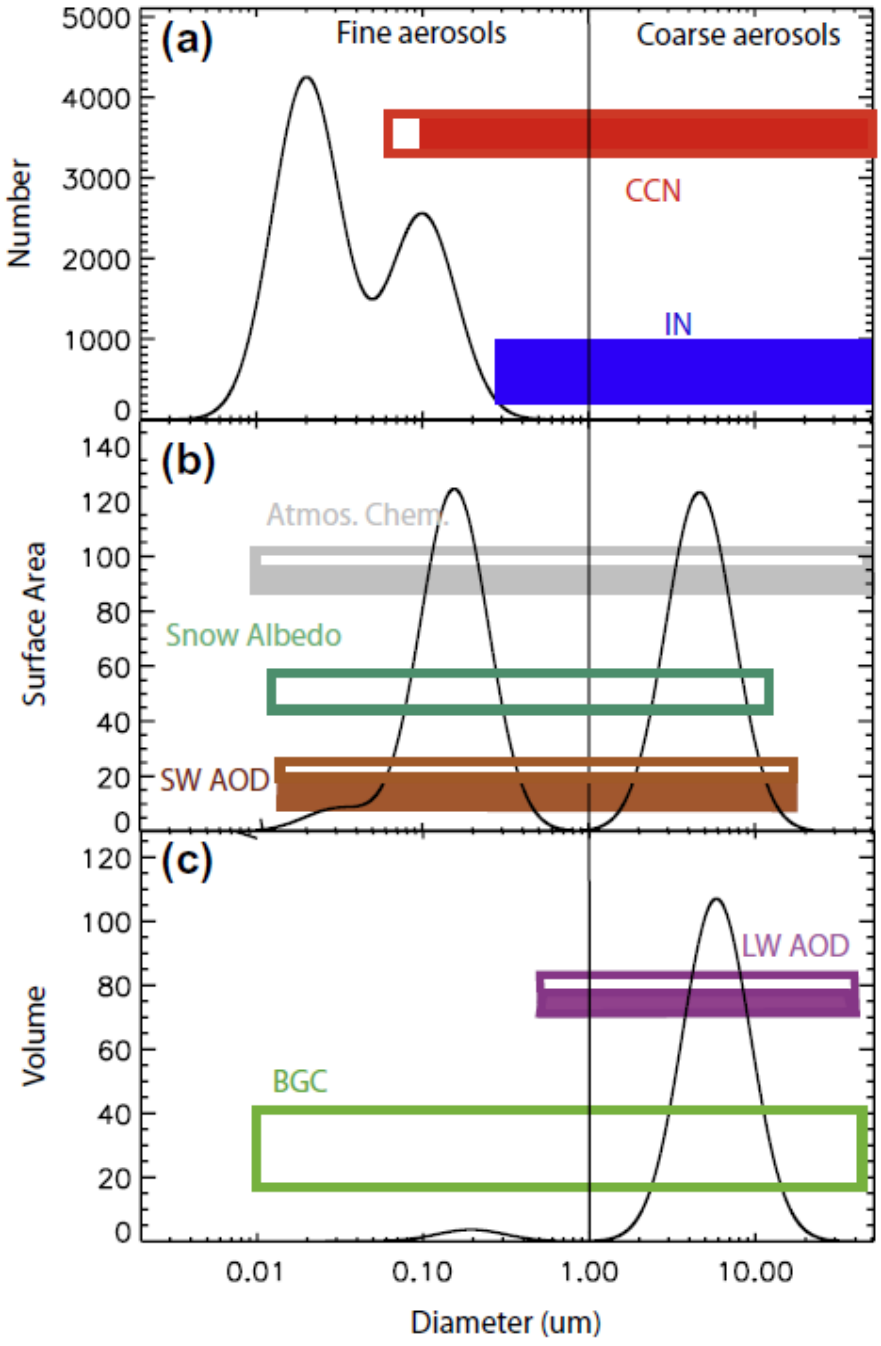

Fig 2.6: A diagram showing a log-normal distribution of fine and coarse aerosols for (a) Aerosol number, (b) surface area, and (c) volume for a typical trimodal aerosol distribution (obtained from Mahowald et al, 2014).

2.4.2 Aerosol extinction coefficient

The extinction of light is given by the Lambert-Beer law:

$$\frac{I(\lambda)}{I_0(\lambda)} = \exp(\sigma_e(\lambda)L) \tag{2.20}$$

where I_0 is the incident light intensity, I is the light intensity traversing the aerosol, σ_e is the extinction coefficient of the aerosol and L is the path length of the light through the aerosol. Fig 2.7 illustrates the process of light extinction by aerosols.

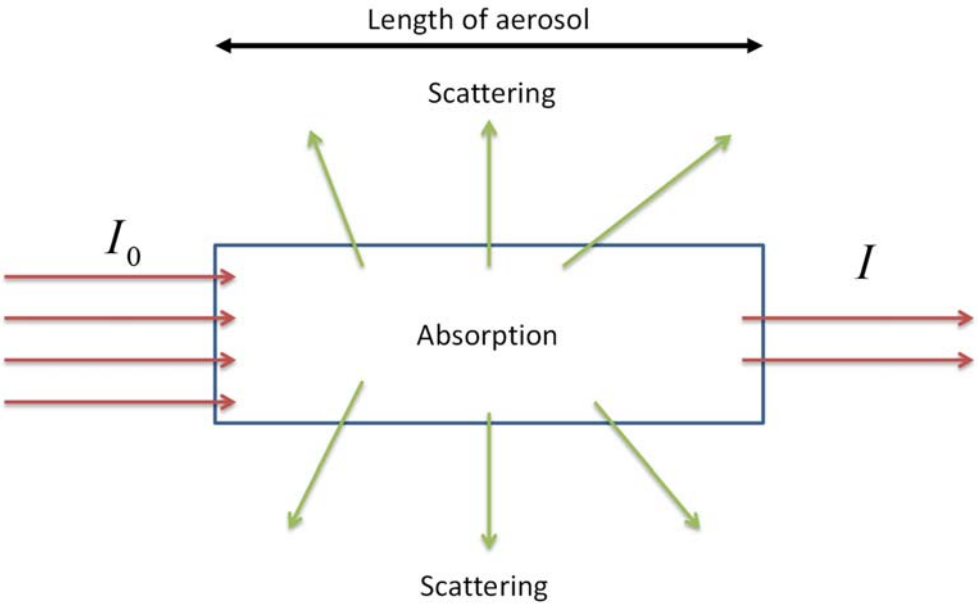

Fig. 2.7: A schematic diagram illustrating the process of light extinction by aerosols.

The light-extinction coefficient, σ_e, can be expressed as a sum

$$\sigma_e = \sigma_{scat} + \sigma_{abs} = \sigma_{sg} + \sigma_{sp} + \sigma_{ag} + \sigma_{ap} \tag{2.21}$$

where σ_{scat} is the sum of scattering by gases and scattering by particles and σ_{abs} is the sum of absorption by gases and particles. σ_{sg} refers to scattering by gases described by Rayleigh scattering, σ_{sp} refers to scattering by particles (both fine and coarse aerosol species), σ_{ag} refers to absorption due to gases and σ_{ap} refers to the absorption due to particles.

2.4.3 Aerosol single scattering albedo

The aerosol single scattering albedo (SSA), ω_0, is defined as the fraction of the aerosol light scattering over the extinction (Akpootu and Momoh, 2013),

$$\omega_0 = \frac{\beta(\lambda)}{\gamma(\lambda)} \tag{2.22}$$

where $\beta(\lambda)$ is the scattering coefficient and $\gamma(\lambda)$ is the extinction coefficient. The SSA is important in (1) determining aerosol climatic effects, (2) explaining differences between calculated and measured down welling radiative fluxes and (3) determining the relationship between satellite-measured radiance and aerosol optical depth (Russell et al, 2002).

Figure 2.8 is an example of a plot showing the aerosol single scattering albedo retrieved with the GIST multi-wavelength Raman LIDAR at 532 nm and the aerosol single scattering albedo retrieved from the Aerosol Robotics Network (AERONET) sun photometer observations at 440, 675, 870, and 1020 nm. Using the depolarization ratio from LIDAR for dust and non-dust aerosols mixed Asian dust plume, Shin et al (2014) extracted vertical profiles of both extinction and backscatter coefficients. An inversion algorithm was used to retrieve the SSAs of non-dust aerosols by putting the vertical profiles of backscatter and extinction coefficients of non-dust particles. These results were then compared to AERONET measurements. SSA values retrieved from LIDAR and AERONET were in good agreement.

2.4.4 Aerosol Optical Depth

Aerosol Optical Depth (AOD) is a measure of aerosols distributed within a column of air from an instrument to the top of the atmosphere (if the instrument is ground based). AOD is also defined as the integrated extinction coefficient over a vertical column of unit cross section. In essence AOD is the degree to which aerosols prevent the transmission of light by absorption or scattering of light. There are various instruments, space-borne and ground-based, that can be used to determine AOD in the atmosphere. AOD is unitless but each value has meaning to it. For example observations from the Moderate Resolution Imaging Spectroradiometer (MODIS) would indicate AOD of less than 0.1 as having clear sky with maximum visibility, whereas AOD of 1 would indicate hazy conditions (see Fig. 2.9).

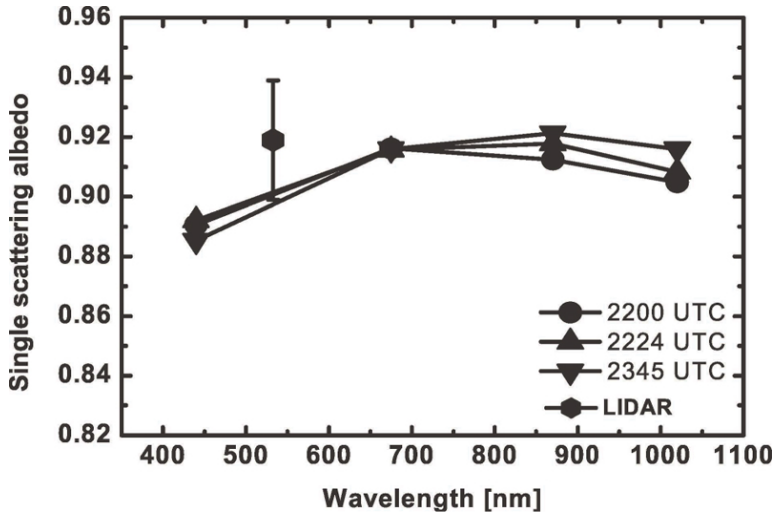

Fig. 2.8: The single scattering albedo of the total mixed dust plume retrieved with GIST multi-wavelength Raman LIDAR (solid hexagon) and the single scattering albedo derived from AERONET sun photometer observations (Level 2.0 data) at 440, 675, 870, and 1020 nm (obtained from Shin et al, 2004).

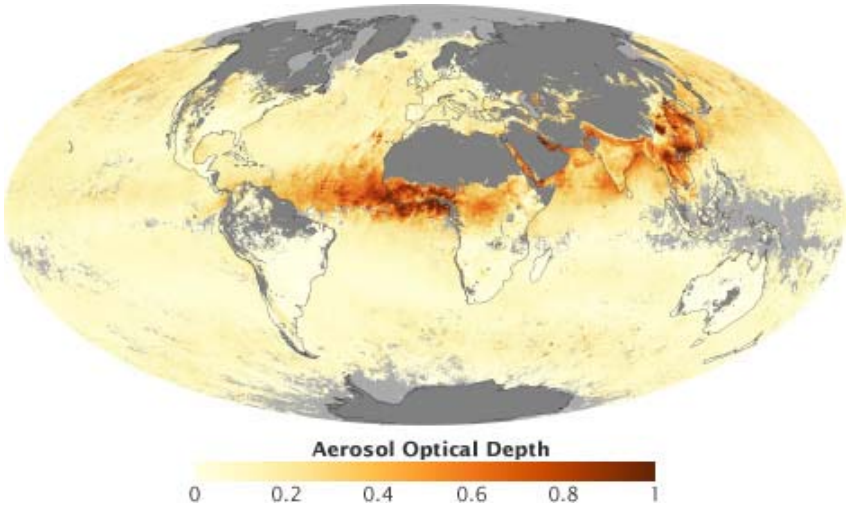

Fig. 2.9: Map from MODIS showing AOD data from around the world on March 2012. (http://earthobservatory.nasa.gov/blogs/earthmatters/2012/04/11/this-weeks-earth-indicator-76/, date accessed on 08/03/2017).

2.4.5 Aerosol Angstrom exponent

The aerosols angstrom exponent is defined as an exponent that expresses the spectral dependence of AOD (τ) with the wavelength of incident light (λ). The Angstrom exponent (α) dependence of AOD (τ), depending on the particle size distribution, can be approximated as

$$\tau_\lambda = \tau_{\lambda 0}\left(\frac{\lambda}{\lambda_0}\right)^{-\alpha} \tag{2.23}$$

where τ_λ is the optical thickness at wavelength λ and $\tau_{\lambda 0}$ is the optical thickness at the reference wavelength λ_0. Angstrom exponent provides additional information on the particle size, aerosol phase function and the relative magnitude of aerosol radiances at different wavelengths. The values of $\alpha \leq 1$ shows aerosol particle size distributions dominated by coarse mode aerosols (radii ≥0.5 mm) that are typically associated with dust and sea salt. Values of $\alpha \leq 2$ show size distributions dominated by fine mode aerosols (radii ≤0.5 mm) that are usually

associated with biomass burning and urban pollution (Schuster et al, 2006). Fig. 2.10 is an example of a plot showing the seasonal Angstrom exponent variation in northeast of China during the 2004 – 2007 periods. The change in the Angstrom exponent seasonally implies the changes of aerosol type.

2.4.6 Aerosol fine mode fraction

Aerosol fine mode fraction (FMF) is defined as the ratio of fine mode (in the micron region) AOD to the total AOD. The FMF value (ranges from 0 to 1) provides quantitative information on the nature of the size distribution of aerosol particles in the atmosphere. FMF= 1 represents anthropogenic AOD dominated by fine (small) -mode aerosols. FMF=0 represents single coarse mode particles originating from natural sources such as wind-blown mineral dust and sea salt (Jones and Christopher, 2007; http://web.iitd.ac.in/~sagnik/SN7.pdf, *date accessed on 08/03/2017*).

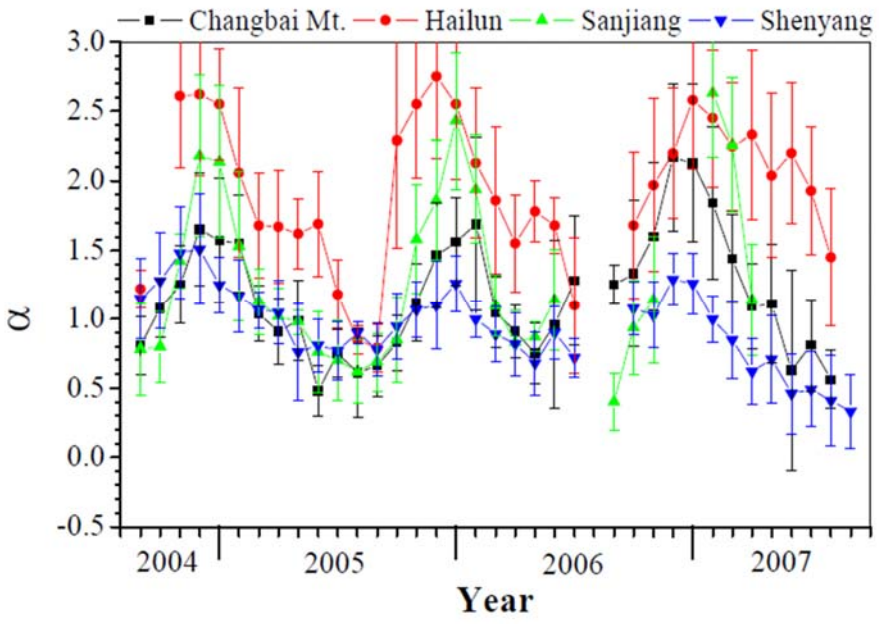

Fig. 2.10: seasonal variation in monthly averaged Angstrom exponent (Obtained from Wang et al, 2008).

2.4.7 Aerosol radiative force

Aerosol radiative forcing (ARF) is defined as the effect of anthropogenic aerosols on the radiative fluxes at the top of the atmosphere (TOA) and at the surface and on the absorption of radiation within the atmosphere (Chung, 2012). The various aerosol types have different effects on the sign and magnitude of the ARF (Alam et al, 2011). Fig. 2.11 shows the RF values in 2005 due to emissions and changes since 1750. (S) and (T) next to gas species represent stratospheric and tropospheric changes, respectively (IPCC, 2007). Fig 2.8 shows the results of RF terms associated with each principal emission including indirect RFs related to perturbations of other forcing agents.

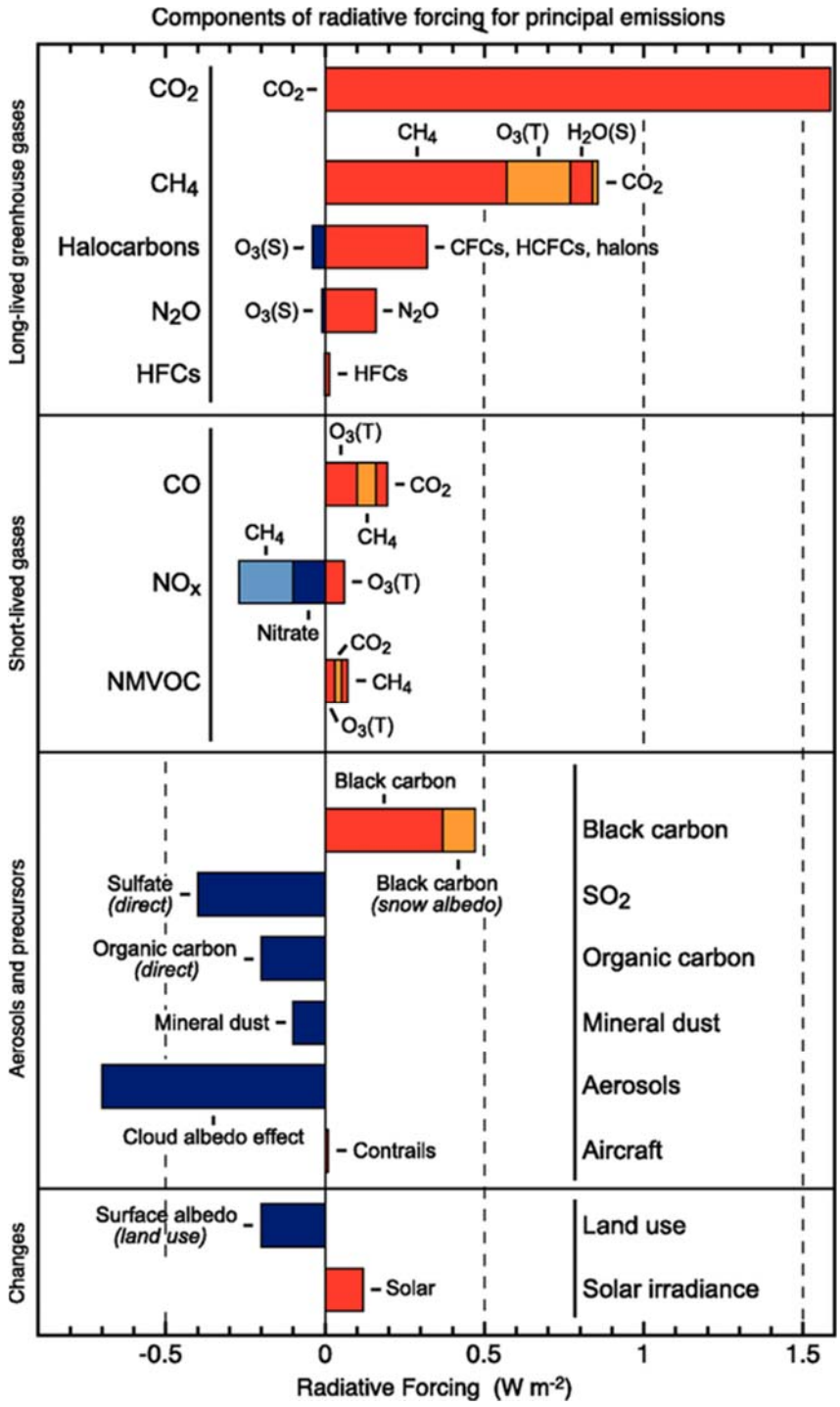

Fig: 2.11: Components of RF for emissions of principal gases, aerosols and aerosol precursors and other changes.Values represent RF in 2005 due to emissions and changes since 1750 (obtained from IPCC, 2007).

The globally averaged direct aerosol radiative forcing, ΔF_R, can be expressed as (Chylek and Wong, 1995),

$$\Delta F_R = -\frac{S_0}{4} T_{atm}^2 (1-N)(1-a)^2 2\beta\tau_{sc} \tag{2.24}$$

where S_0 is the solar constant, T_{atm} is the transmittance of the atmosphere above the aerosol layer, N is the fraction of sky covered by clouds, a is the albedo of underlying surface, β is the fraction of radiation scattered by aerosols into the upper hemisphere and τ_{sc} is the aerosol layer scattering optical thickness.

The last term in equation (2.24)

$$(1-a)^2 2\beta\tau_{sc} \tag{2.25}$$

represents the albedo increase due to a non-absorbing layer. The radiative transfer equation for an optically thin atmosphere leads to the following expression for the planar albedo $R(\mu_0)$ and transmission $T(\mu_0)$ of an isolated optically thin aerosol layer illuminated by a mono-directional beam (Chylek and Wong, 1995),

$$R(\mu_0) = \frac{\tau\omega\beta(\mu_0)}{\mu_0} \tag{2.26}$$

$$T(\mu_0) = 1 - \frac{\tau}{\mu_0}[1-\omega+\omega\beta(\mu_0)] \tag{2.27}$$

where μ_0 is a direction cosine of incoming radiation with respect to the normal to the layer, τ is the extinction optical depth, ω is a single scattering albedo and $\omega\beta(\mu_o)$ is a fraction of radiation scattered into the upper hemisphere. The total reflectance R and total transmittance T of a layer is obtained by integrating equation (2.25) and (2.26) over all angles of incoming radiation. From the absorbance $A=1-T-R$ we obtain

$$R = 2\tau\omega\beta = 2\beta\tau_{sc} \tag{2.28}$$

$$A = 2\tau(1-\omega) = 2\tau_{abs} \tag{2.29}$$

where $\beta = \int \beta(\mu_0) d\mu_0$. Using equation (2.28) with an appropriate expansion of an optically thin layer we obtain

$$\Delta R = (1-a)^2 R - 2aA = (1-a)^2 2\beta\tau_{sc} - 4a\tau_{abs} \tag{2.30}$$

So equation (2.24) can be modified to a more general form valid for absorbing aerosols as well

$$\Delta F = -\frac{S_0}{4} T_{atm}^2 (1-N)\left[(1-a)^2\, 2\,\beta\,\tau_{sc} - 4a\,\tau_{abs}\right] \tag{2.31}$$

For non-absorbing aerosols we have $\tau_{abs} = 0$.

2.5 Remote sensing

2.5.1 Introduction

Remote sensing (RS) is described as the science of identifying, observing, and measuring an object without coming into direct contact with it. In order for this to happen the information needs a physical carrier to travel from the object to the sensors through a medium. In most cases, the electromagnetic radiation is normally used as an information carrier in remote sensing. Two characteristics of electromagnetic radiation that are particularly important for understanding remote sensing are the wavelength and frequency. Therefore understanding the characteristics of electromagnetic radiation (EMR) in terms of their wavelength and frequency is crucial to understand the information to be extracted from remote sensing data.

2.5.2 Principles of remote sensing

Various objects emit or reflect different amounts of energy in different bands of the electromagnetic spectrum. The properties of the material and the incident energy determine the amount of energy being emitted or reflected. The basic

principles of remote sensing are shown in Fig. 2.12. The source is something that emits EMR into the atmosphere or the environment. The source could be natural like the sun or a device like a laser. The EMR released interacts with the object which results in another EMR of a different or similar wavelength being released. The secondary EMR is then detected by the sensor and moved to the data acquisition system. The collected data is stored in various data warehouses where it is then processed using software, algorithms and models. Images, graphs and tables are the resultants of data processing which are then used for analysis.

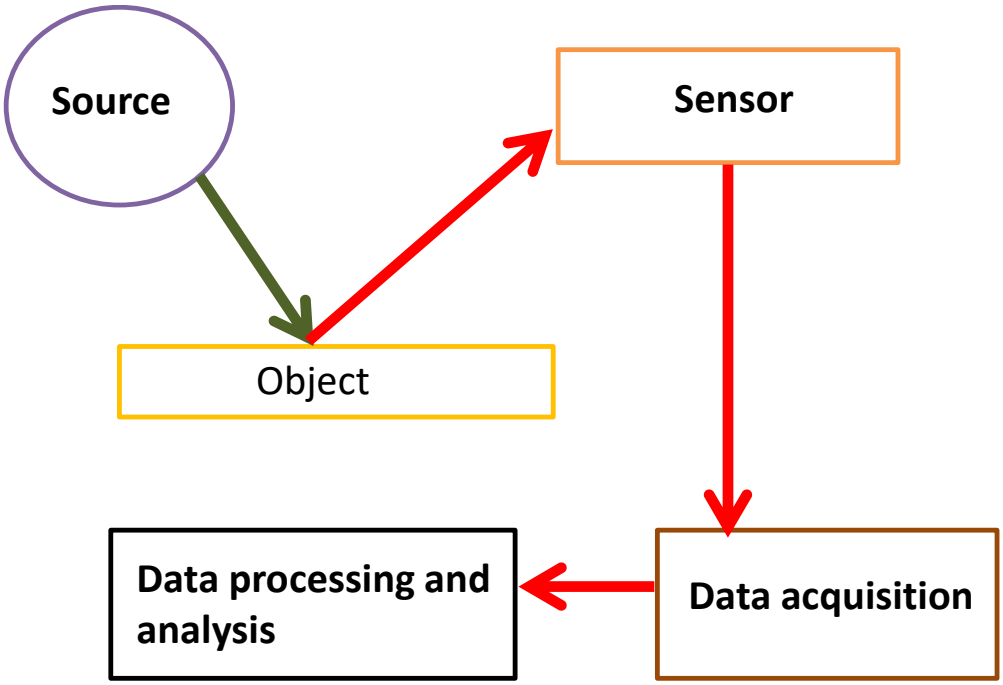

Fig: 2.12: Schematic diagram illustrating the principle of remote sensing.

There are two types of remote sensing systems; passive and active. Passive remote sensing involves the collection of energy from the environment, in most instances the energy source is the sun, see Fig 2.13. Passive systems have several advantages such as low electrical requirements and multiple wavelength information. One of the biggest disadvantages of passive remote sensing is the measurements can only be carried out during day time when the sun is present. In

a similar manner measurements are also depended on the weather conditions. For example, if it is raining and if there are thick clouds present, optical or remote measurements cannot be carried out due to the lack of signal being able to penetrate the clouds. Some examples of passive sensors are radiometers, charged-coupled devices and hyperspectral sensors.

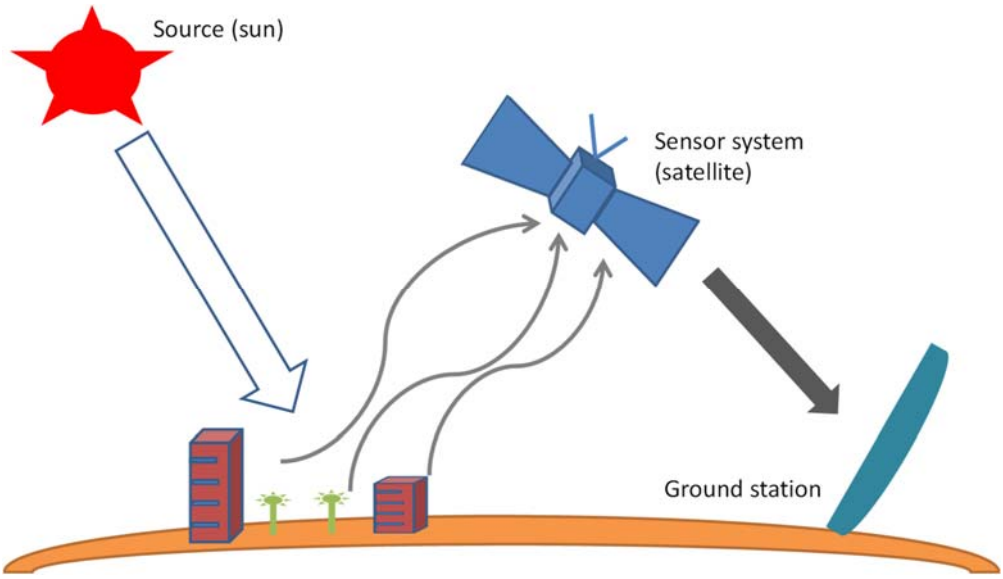

Fig 2.13: Drawing illustrating a remote sensing passive sensor system

Active remote sensing involves emitting energy and then measuring that energy when it is returned back into the instrument, see Fig 2.14. Active remote sensing has several advantages which include; being independent of weather (radiation can penetrate clouds, snow or rain), being independent of sunlight and it can give information about moisture content of soil layers. One of the biggest disadvantages of active remote sensing is that its pulse power is mostly low and can be influenced or interfered by other radiation sources.

Based on the elevation from the earth's surface, remote sensing can be classified at different platforms. These platforms are the ground remote sensing, aerial remote sensing and the space borne remote sensing. Some examples of active

remote sensing instruments are the LIght Detection And Ranging (LIDAR) and RAdio Detection And Ranging (RADAR).

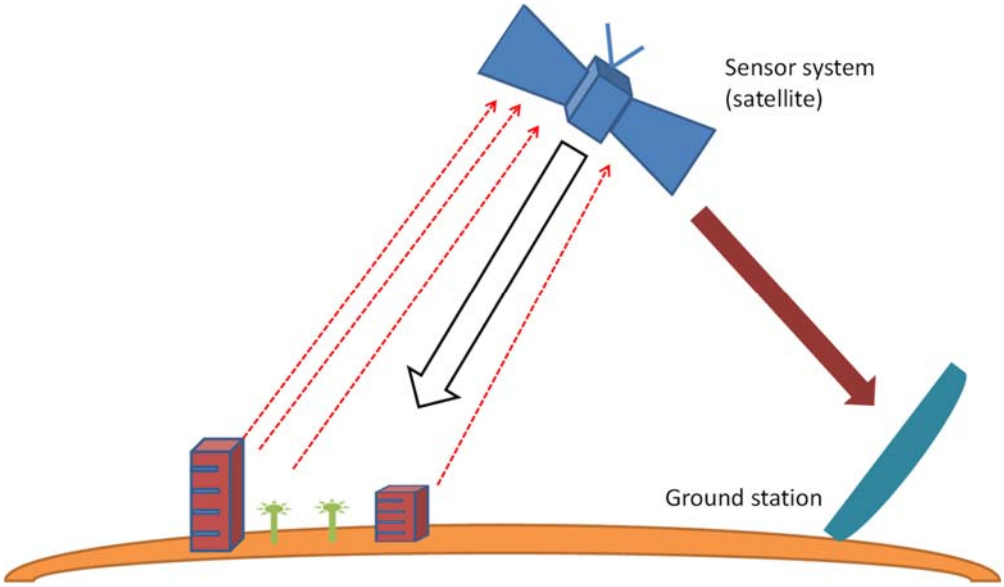

Fig 2.13: Drawing illustrating a remote sensing active sensor system

2.5.3 Remote sensing applications

Since remote sensing is considered as a science, it has fond of various applications in different areas of science which include earth sciences, atmospheric sciences as well as space sciences. Table 2.1 summarises the different applications of remote sensing. However, for this work the remote sensing application interest is on the atmosphere. Various atmospheric parameters such as AOD, FMF, aerosol extinction coefficients are measured using different instruments such as ground based LIDAR, Cloud-Aerosol Lidar and Infrared Pathfinder Satellite Observation (CALIPSO), Moderate Resolution Imaging Spectroradiometer (MODIS) and photo-meters.

Table 2.1: Remote sensing applications in the various disciplines of science

Remote sensing Application	**Description**
Atmosphere study	Study of atmospheric pressure, water vapour, temperature and wind velocity.
Oil and mineral exploration	Discovering slicks and natural oil seeps, mapping geological structures, monitoring oil field subsidence.
Military	Developing accurate maps for monitoring military infrastructure, monitoring ship and troop movements.
Climate	Effects of climate change on glaciers and Arctic and Antarctic regions.
Agriculture	Mapping of farm and land characteristics, soil sensing and agriculture estimation.
Atmosphere	Study different structures of the atmosphere, aerosols and clouds to name a few.

In Chapter 3 we discuss the different types of instruments used for remote sensing measurements of the atmosphere parameters.

References

Alam K., Trautmann T., Blaschke T., 2011. Aerosol optical properties and radiative forcing over mega-city Karachi. Atmospheric Research 101, 773–782

Akpootu D. O., Momoh M., 2013. The scattering coefficient, extinction coefficient and single scattering albedo of water soluble in the radiative forcing of urban aerosols. Archives of Applied Science Research 5 (2), 109-120. ISSN 0975-508X

Chan T. W., Mozurkewich M., 2007. Simplified representation of atmospheric aerosol size distributions using absolute principal component analysis. Atmospheric Chemistry and Physics 7, 875–886

Chung E. C., 2012. Aerosol Direct Radiative Forcing: A Review, Atmospheric Aerosols - Regional Characteristics - Chemistry and Physics, Dr. Hayder Abdul-Razzak (Ed.), ISBN: 978-953-51-0728-6, InTech, DOI: 10.5772/50248.

Chylek P., Wong J., 1995. Effects of absorbing aerosols on global radiation budget. Geophysical Research Letters 22, 929-931

Dal Maso M., Kulmala M., Riipinen L., Wagner R., Hussein T., Aalto P. P., Lehtinen K. E. J., 2005. Formation and growth of fresh atmospheric aerosols: eight years of aerosol sizedistribution data from SMEAR II, Hyytiälä, Finland. Boreal environmental research 10, 323-336, ISSN 1239-6095

Intergovernmental Panel on Climate Change. 2001. Climate Change 2001. Synthesis report. Cambridge University Press. Cambridge.

Jones T. A., Christopher S. A., 2007. MODIS derived fine mode fraction characteristics of marine, dust, and anthropogenic aerosols over the ocean, constrained by GOCART, MOPITT, and TOMS. Journal of Geophysical Research. 112, D22204, doi:10.1029/2007JD008974

Lee G-G., Yuan C-S., Chang J-C., Yuan C., 2005. Effects of Aerosol Species on Atmospheric Visibility in Kaohsiung City, Taiwan. Journal of the Air & Waste Management Association 55, 1031-1041

Lushnikov A. A., 2010. Introduction to Aerosols. Aerosols – Science and Technology, WILEY-VCH Verlag GmbH & Co. KGaA, Weinheim ISBN: 978-3-527-32660-0

Mahowald N., Albani S., Kok J. F., Engelstaeder S., Scanza R., Ward D. S., Flanner M. G., 2014. The size distribution of desert dust aerosols and its impact on the Earth system. Aeolian Research 15, 53–71

Pöschl U., 2005. Atmospheric Aerosols: Composition, Transformation, Climate and Health Effects. Atmospheric Chemistry 44, 7520 – 7540

Rusell P. B., Redemann J., Schmid B., Bergstrom R. W., Livingston J. M., Mcintosh D. M., Ramirez S. A., Hartley S, Hobbs P. V., Quinn P. K., Carrico C. M., Rood M. J., Östrom E., NOONE K. J., Von Hoyningen-Huene W., Remer L., 2002. Comparison of Aerosol Single Scattering Albedos Derived by Diverse Techniques in Two North Atlantic Experiments. Journal of the atmospheric sciences 59, 609-619

Schuster G. L., Dubovik O., Holben B. N., 2006. Angstrom exponent and bimodal aerosol size distributions. Journal of Geophysical Research 111, D07207, doi:10.1029/2005JD006328

Shin S., Noh Y. M, Lee K., Lee H.,, Müller D., Kim Y. J.,Kim K., Shin D., 2014. Retrieval of the Single Scattering Albedo of Asian Dust Mixed with Pollutants Using Lidar Observations. Advances in Atmospheric Sciences 31, 1417–1426

Singh A., Dey S., 2012. Influence of aerosol composition on visibility in megacity Delhi. Atmospheric Environment 62, 367-373

Sivasakthivel.T, Reddy K.K.S. K., 2011. Ozone Layer Depletion and Its Effects: A Review. International Journal of Environmental Science and Development 2, 30-37.

Tiwari S., Payra S., Mohan M., Verma S., Bisht D. S., 2011. Visibility degradation during foggy period due to anthropogenic urban aerosol at Delhi, India. Atmospheric Pollution Research 2, 116-120

Wang Y., Xin J., Li Z., Wang S., Wang P., Hao W. M., Nordgren B. L., Chen H., Wang L., Sun Y., 2008. Seasonal variations in aerosol optical properties over China. Atmospheric Chemistry and Physics Discussions 8, 8431–8453

Wiedensohler A., Birmili W., Nowak A., A. Sonntag, Weinhold K., Merkel M., Wehner B., Tuch T., Pfeifer S., Fiebig M., Fjäraa A. M., Asmi E., Sellegri K., Depuy R., Venzac H., Villani P., Laj P., Aalto P., Ogren J. A., Swietlicki E, Williams P., Roldin P., Quincey P., Hüglin C., Fierz-Schmidhauser R., Gysel M, Weingartner E., Riccobono F., Santos S., Grüning C., Faloon K., Beddows D., Harrison R., Monahan C., Jennings S. G., O'Dowd C. D., Marinoni A, Horn H –G., Keck L., Jiang J., Scheckman J., McMurry P. H., Deng Z., Zhao C. S., Moerman M., Henzing B., de Leeuw G., Löschau G., Bastian S., 2012. Mobility particle size spectrometers: harmonization of technical standards and data structure to facilitate high quality long-term observations of atmospheric particle number size distributions. Atmospheric Measurement Techniques 5, 657–685

Zhou J., Zhang R., Cao J., Chow J. C., Watson J. G., 2012. Carbonaceous and Ionic Components of Atmospheric Fine Particles in Beijing and Their Impact on Atmospheric Visibility. Aerosol and Air Quality Research 12, 492–502

Chapter 3

Instruments

3.1 Introduction

Remote sensing instruments can be classified into one of two major categories, either passive or active. Since remote sensing allows for measurements of objects without any physical contact, this has a few advantages such as; (1) avoiding hazard or difficulties to reach regions, (2) can measure a process without disturbance and (3) can smooth local fluctuations by averaging over a large volume. There are three broad categories of remote sensing platforms: ground-based, airborne, and space-borne. Table 3.1 shows a summary of the types of platforms. Ground-based instruments are usually used to monitor the lower part of the atmosphere. However, depending on the source some instruments can detect more than 100 km from the earth atmosphere. Airborne instruments are operated in the air and usually monitor anything in a downward direction toward the ground. Similar to airborne instruments are the space-borne instruments which also operate in the air but at higher altitudes, see Table 3.1. The ground-based, airborne and space-borne instruments are able to give information about the constituents in the different layers of the atmosphere. Different instruments are designed to measure and/or observe different constituents in the atmosphere.

In this chapter we will describe in detail the theory of operation and measurement techniques of the Council for Scientific and Industrial Research (CSIR) Light detection and Ranging (LIDAR) system. We will also briefly discuss some other instruments used in this work.

Table 3.1: Categories of remote sensing platforms and their altitudes

Category of remote sensing platforms	**Platform**	**Altitude**
Ground-based	Vehicle, ship, tower or ground	Platforms can reach levels up to 50 m (http://irina.eas.gatech.edu/EAS6145_Spring2007/Lecture2.pdf, date accessed on 12/04/2017)
Airborne	Airplanes, helicopters, high-altitude aircrafts, balloons	Platforms can reach levels up to 50 km (http://irina.eas.gatech.edu/EAS6145_Spring2007/Lecture2.pdf, date accessed on 12/04/2017)
Space-borne	Rockets, satellites, shuttle	100 km to 36000 km (http://www.academia.edu/12758731/REMOTE_SENSING_PLATFORMS, date accessed on 12/04/2017)

3.2 LIDAR

A LIDAR is an instrument that operates by emitting a laser signal and detecting the backscattered signal from the object. It has many applications in many areas such as military, oil and exploration, archaeology, and meteorology. In this work, it is focused on the application of LIDAR in meteorology.

3.2.1 Principle of LIDAR

The basic principle of LIDAR is shown in Fig. 3.1. The laser is the device that releases light in the form of radiation into atmosphere. The light then interacts with the object and it emits light of the same or different frequency, depending on the scattering process and is reemitted off with the same or different frequency, depending on the involved physical process. The scattered light then gets detected. There are two physical processes in LIDAR scattering; elastic and inelastic. Elastic scattering occurs when the incident light scatters from a particle and the

reflected light has the same frequency as the incident light. Rayleigh scattering from molecules and Mie scattering from small particles are examples of elastic scattering. On the other hand, inelastic scattering occurs when the incident light on an object experiences a shift in frequency.

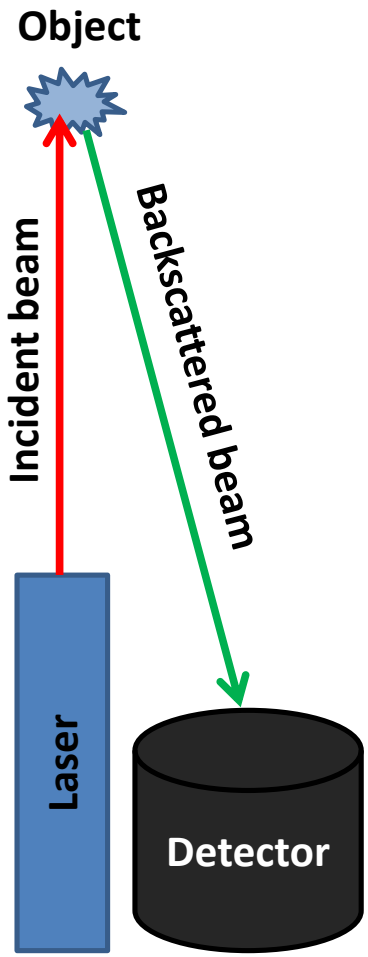

Fig. 3.1: Schematic diagram illustrating the principles of LIDAR.

3.2.2 Types of LIDAR systems

There are different types of LIDAR systems that measure different constituents in the atmosphere. Table 3.1 summarizes different kinds of LIDAR systems. The Mie LIDAR system uses the elastic scattering process and it is used to measure/study aerosols and clouds. This technique is often used in the low parts

of the atmosphere (troposphere) as that is where most aerosol particles and clouds are found. At higher altitudes (stratosphere) the atmosphere gets dominated by molecules. The Rayleigh LIDAR is then ideal to carry out measurements of molecule density to study the temperature in the stratosphere and mesosphere. It is well known that Raman signals are generally weak; however, Raman LIDAR can be used to study the lower atmospheric temperature, humidity, aerosols and clouds in the troposphere. Not all molecules and particles in the atmosphere scatter light; there are some that absorb light. The Differential Absorption LIDAR (DIAL) is used to detect gaseous pollutants; it can also be used to study ozone, water vapour and humidity. DIAL operates differently from the other LIDAR systems. DIAL operates on two wavelengths, one at resonance with the molecular vibrations and one off resonance with the molecular vibrations. The resonance wavelength will be absorbed by the molecule and identified whereas the off resonance one will be reflected back without absorption.

Table 3.2: Different types of LIDAR systems

Physical Process	**LIDAR system**	**Objective**
Elastic Scattering by Aerosols and Clouds	Mie Lidar	Aerosols, Clouds: Geometry, Thickness
Elastic Scattering by Air Molecules	Rayleigh Lidar	Stratosphere & Mesosphere Density & Temperature
Inelastic Scattering	Raman Lidar	Temperature in Lower Atmosphere, Humidity Aerosols, Clouds: Optical Density
Absorption by Atoms and Molecules	DIfferential Absorption LIDAR (DIAL)	Gaseous Pollutants Ozone Humidity

3.2.3 LIDAR equation

There are different LIDAR equations describing the different LIDAR systems showed in Table 3.1. In this part only the equation of the Mie LIDAR system will be discussed as that is the system that was used in this work. The general equation for a monostatic single wavelength pulsed LIDAR is given by (Klett, 1981)

$$p(r) = p_0 \frac{c\tau}{2} A \frac{\beta(r)}{r^2} \exp\left[-2\int_0^r \sigma(r')dr'\right] \tag{3.1}$$

where $p(r)$ is the instantaneous received power at time t, p_0 is the transmitted power, c is the velocity of light, τ is the pulse duration, A is the effective system receiver area, r is the range, $\beta(r)$ is the volume backscatter coefficient of the atmosphere and $\sigma(r)$ is the extinction coefficient of the atmosphere. In equation 3.1 we have two unknowns; $\beta(r)$ and $\sigma(r)$. This poses a problem as there is only one equation and two unknowns. There are several approaches to solve this equation but it has been found that the most stable solution was proposed by Fernald (1984) and Klett (1985) and it was derived for aerosol backscatter coefficient. The solution for equation 3.1 using Fernald method is

$$\beta_{aer}(r) + \beta_{mol}(r) = \frac{X(r)\exp\left[-2(S_{aer}(r) - S_{mol})\int_{r_c}^{r} \beta_{mol}(r)dr\right]}{\frac{X(r_c)}{\beta_{aer}(r_c) + \beta_{mol}(r_c)} - 2S_{aer}\{\int_{r_c}^{r} X(r)\exp[-2(S_{aer}(r) - S_{mol})\int_{r_c}^{r} \beta_{mol}(r')dr']dr\}} \tag{3.2}$$

where $X(r)$ is the range normalized signal given by $p(r)r^2$ and r_c is the reference height. When $r = r_c$ we obtain the stable far-end solution as shown in equation 3.2, in the far field $\beta(r)$=0.

3.2.4 CSIR mobile LIDAR

The CSIR mobile Mie LIDAR system was developed in 2007 in Pretoria with the intention of using it for the studies of aerosols and clouds. The layout of the system is shown in Fig. 3.2. The system is made up of three main sections; transmitter, receiver and data acquisition. Sharma et al (2009) and Sivakumar (2012) describe the CSIR mobile LIDAR system in detail, however, the major specifications are summarized in Table 3.3.

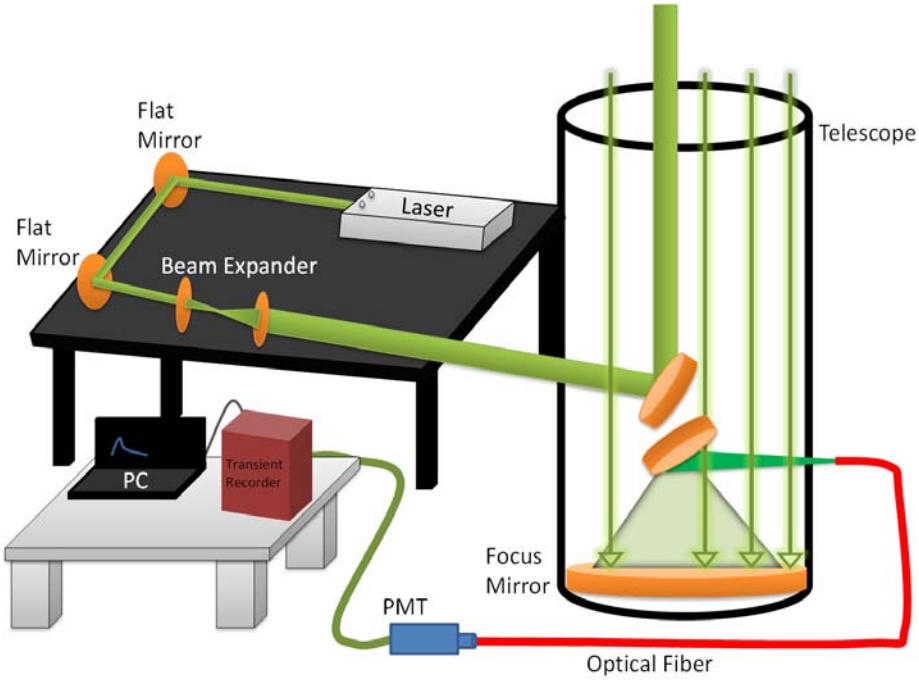

Fig. 3.2: Schematic diagram of the CSIR mobile LIDAR system.

Table 3.3: CSIR mobile LIDAR system major specifications

Emission		**Reception**	
Laser	Nd:YAG	Telescope diameter	404 mm
Wavelength	532 nm	Field of View	0.5 mrad
Repetition rate	10 Hz	Vertical resolution	10 m
Energy per shot	140 mJ	Detection	Photon Counting
Beam divergence	0.2 mrad		

Since its development in 2007 the system was able to generate scientific results. In 2008 aerosols studies were conducted in Pretoria on 23 February 2008. The aerosol extinction coefficient profile was retrieved from the LIDAR (see Fig. 3.3).

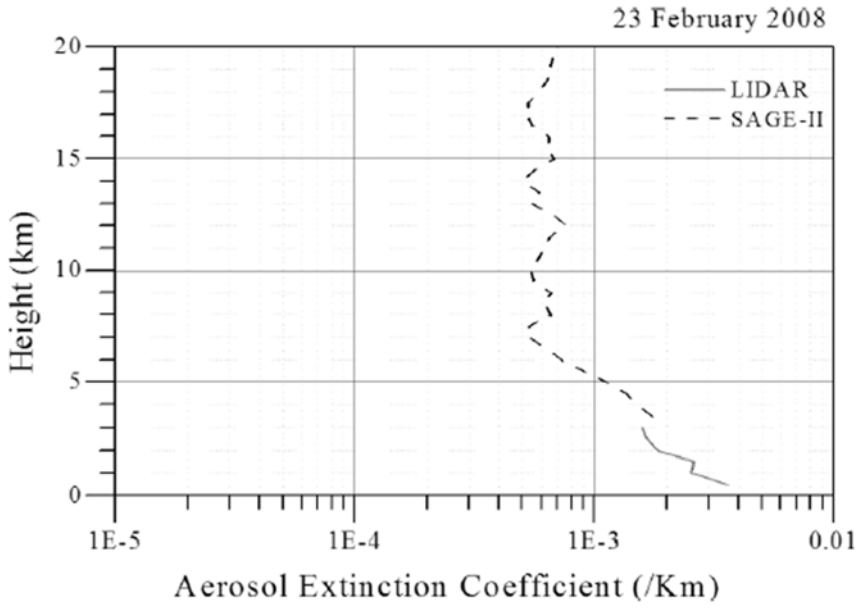

Fig. 3.3: Height profile of aerosols extinction retrieved from LIDAR signals returns and SAGE II satellite data (obtained from Sivakumar et al, 2008).

In 2009 cloud observations were reported by Sivakumar et al (2009), see Fig. 3.4. Strong backscattered signals are noticed at the height around 10 km and just above are due to the presence of high altitude clouds.

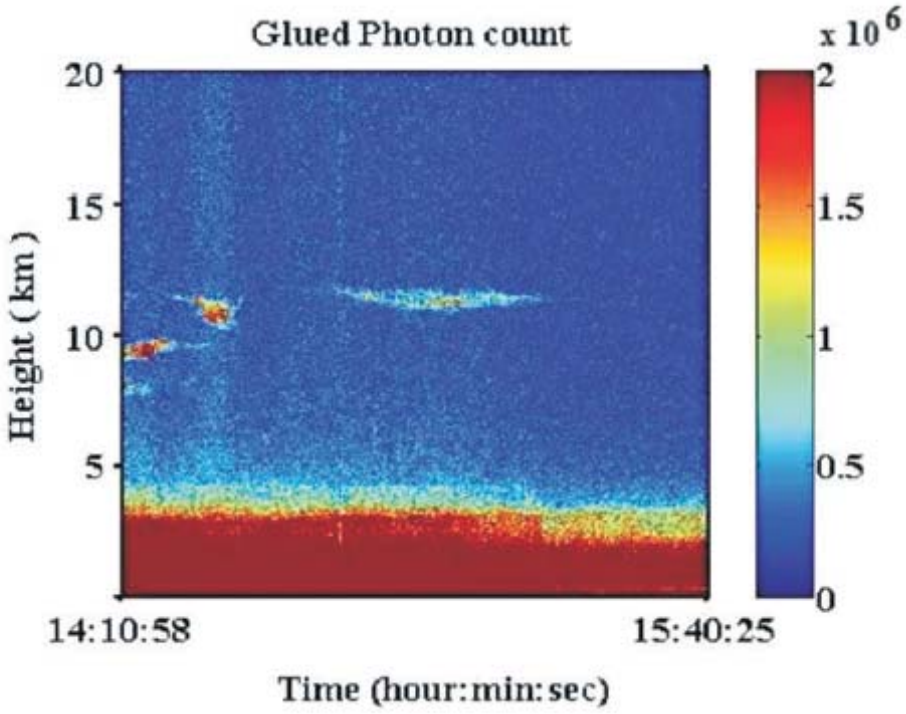

Fig. 3.4: Height-time colour map of LIDAR signal returns for 25 February 2008 (obtained from Sivakumar et al, 2009).

In 2013 modifications on the system began. The aim was to mount a scanner on the system which would allow for: (1) study of aerosols and clouds at any particular angles and (2) X-Y dimensional mapping of the atmosphere. Fig 3.5 shows the mobile LIDAR system with scanner mounted.

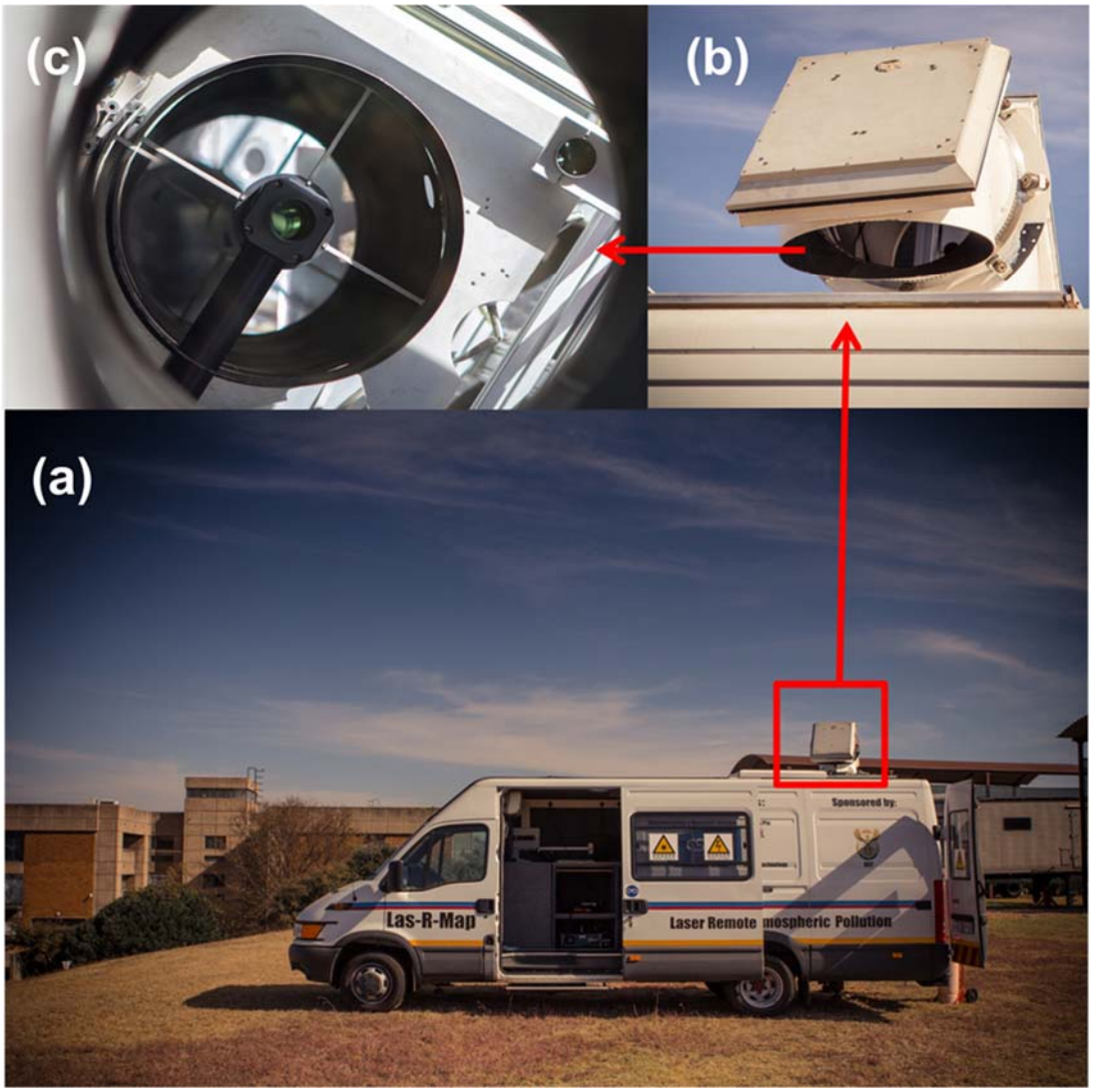

Fig. 3.5: (a) CSIR mobile LIDAR system with a scanner. (b) The scanner pointing in a vertical direction. (c) A Newtonian telescope with a 404 mm primary mirror used to collect the backscattered light from the atmosphere.

Vertical test measurements were performed to validate the mobile LIDAR system with scanner. Aerosol Optical Depth (AOD) measurements were conducted and compared to those of the sun-photometer. Measurements were done in Pretoria on the 26-27 June 2014 (see Fig. 3.6) and the AOD comparison between the LIDAR and the sun-photometer were carried out (see Table 3.4). The AOD values of about 0.12 and 0.25 were observed on 26 and 27 June 2014 respectively by both

the instruments. It has evidenced a good agreement that implies that the LIDAR instrument can be trusted with future measurements. These values indicate a relatively clean atmosphere over the observation site.

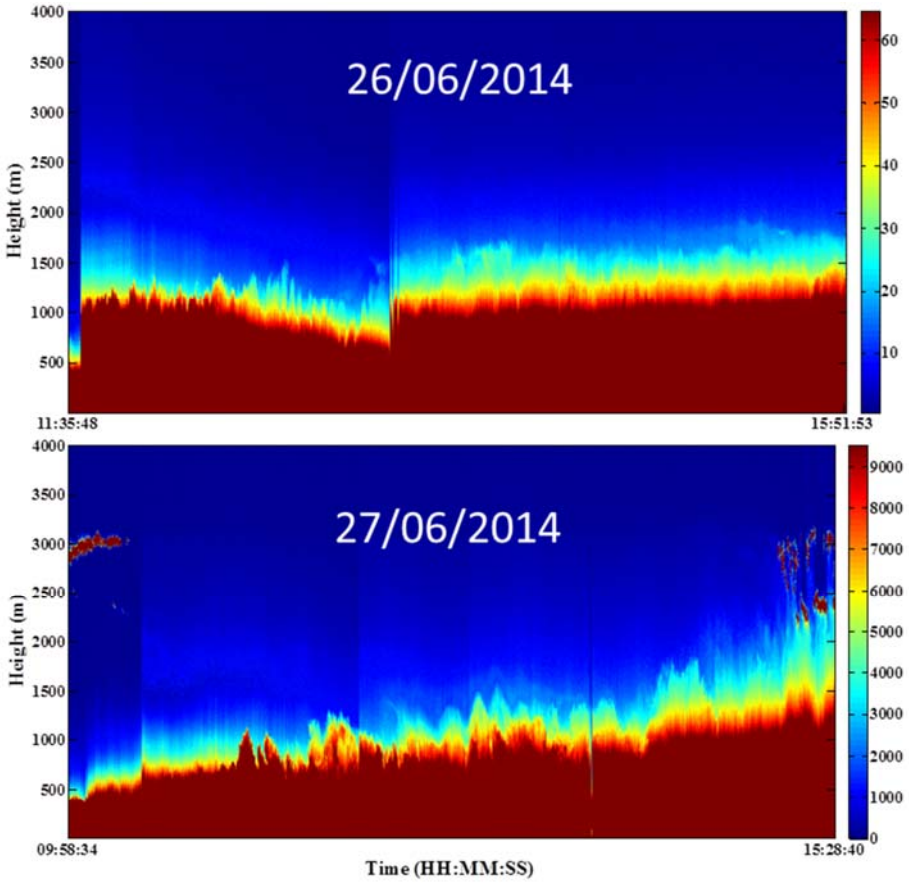

Fig. 3.6: Height-time color map of CSIR-NLC mobile LIDAR backscatter signal returns at daytime in Pretoria on 26 and 27 June 2014 (obtained from Shikwambana and Sivakumar, 2014).

Table 3.4: Comparison of LIDAR and sun photometer AOD measurements (obtained from Shikwambana and Sivakumar, 2014)

Date	AOD LIDAR	AOD Sun photometer
26/06/2014	0.1206	0.1233±0.0188
27/06/2014	0.2652	0.2480±0.0605

3.3 Sun-photometer

Sun-photometers are instruments used for observing and measuring optical properties of atmospheric aerosols. They are also used to quantify and characterise aerosols. Their data can be used for meteorological and atmospheric applications.

For this work a CIMEL Electronique 318A spectral radiometer which forms part of the AErosol RObotic NETwork (AERONET) was used. The sun-photometer is situated in Pretoria (25.7° S, 28.1° E) and it measures sun and sky radiances at a number of fixed wavelengths within the visible and near-infrared spectrum. AERONET provides inversion products, precipitable water and spectral aerosol optical depth (AOD) in diverse aerosol regimes. AOD data is computed for three data quality levels namely, Level 1.0 (unscreened), Level 1.5 (cloud-screened), and Level 2.0 (cloud screened and quality-assured). Precipitable water, inversions and other AOD-dependent products are derived from these levels and may implement additional quality checks. (http://aeronet.gsfc.nasa.gov/, *date accessed on 08/03/2017*). The instrument is electronically controlled, has on-board data storage capability and incorporate an automated tracking system for accurate positioning and pointing (http://www.ncaveo.ac.uk/site-resources/pdf/cimel.pdf, *date accessed on 08/03/2017*).

The basic operation of the system is shown in Fig. 3.7. Sunlight interacts with the aerosols in the atmosphere and causes light to scatter. The un-scattered light is then detected by the sun-photometer. Direct sun measurements are made in eight spectral bands requiring approximately 10 seconds. A direct drive stepping motor rotates eight interference filters at wavelengths of 340, 380, 440, 500, 670, 870,

940 and 1020 nm which are located in a filter wheel. Measurements are taken by the instruments starting at an air mass of 7 in the morning and ending at an air mass of 7 in the evening. Aerosol optical depth is calculated from the spectral extinction of direct beam radiation at each wavelength based on the Beer-Bouguer Law (http://aeronet.gsfc.nasa.gov/new_web/system_descriptions_operation.html, *date accessed on 08/03/2017*). A typical sun-photometer AOD plot from AERONET is shown in Fig. 3.8. This is level 2 data which has been cloud screened and quality assured.

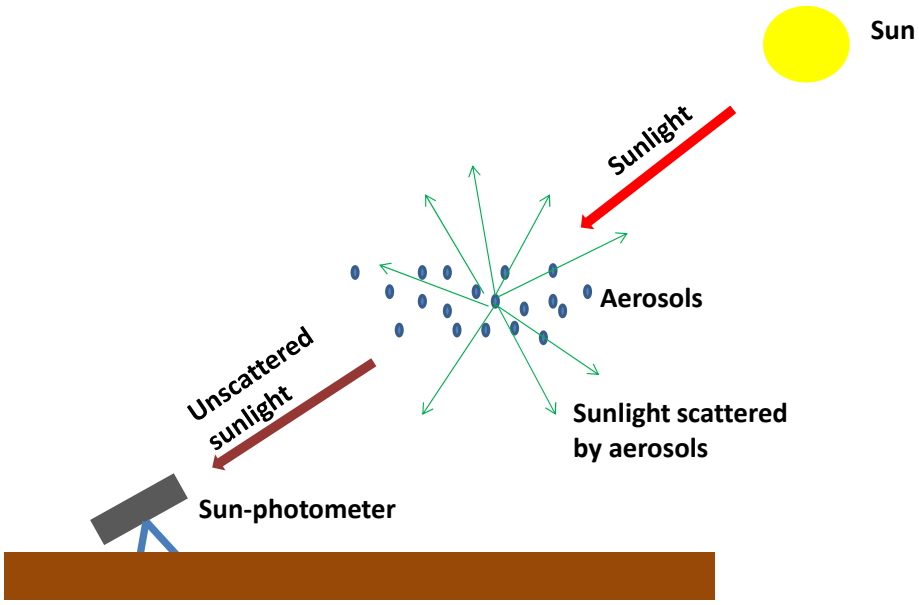

Fig. 3.7: Diagram illustrating the principles of the sun-photometer.

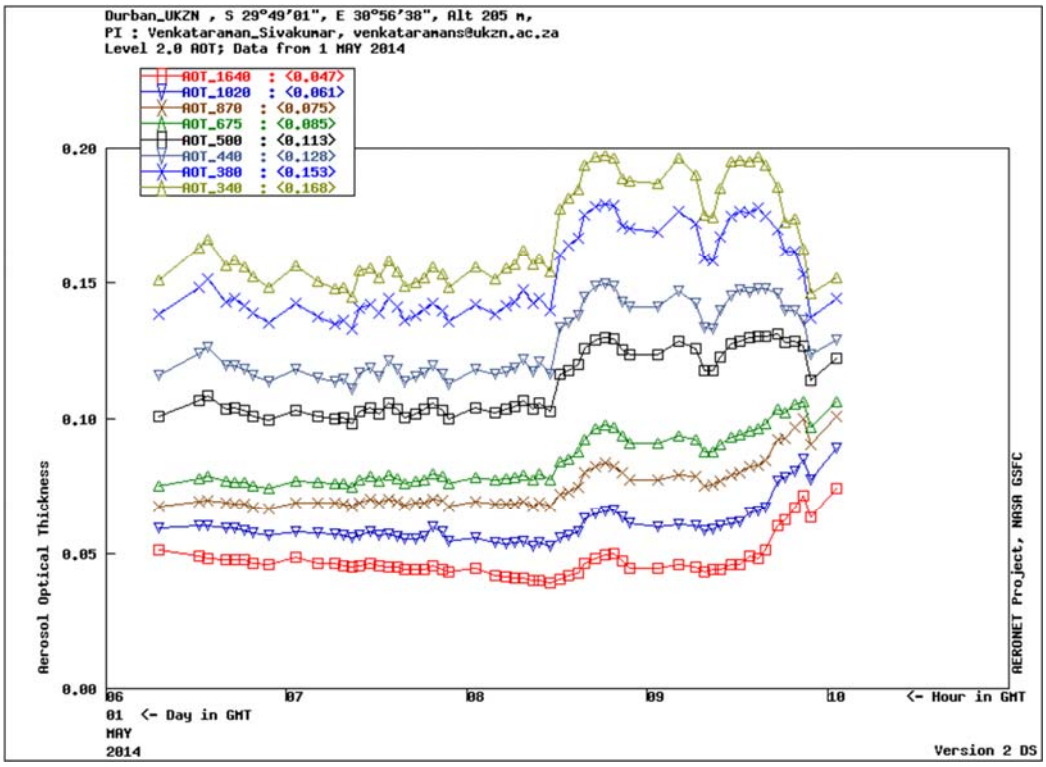

Fig. 3.8: A typical AOD plot for level 2 data at Durban on 1 May 2014 (obtained from AERONET; https://aeronet.gsfc.nasa.gov/ , date accessed on 08/03/2017).

3.4 MODIS

The Moderate Resolution Imaging Spectroradiometer (MODIS) is an instrument aboard the Terra Earth observation system (EOS AM) and Aqua (EOS PM) satellites (http://modis.gsfc.nasa.gov/about/; date accessed on 08/03/2017). The Terra's orbit around the earth is timed so that it passes over the equator from north to south in the morning. The Aqua's orbit is timed so that it passes over the equator from north to south in the afternoon.

MODIS takes measurements at three spatial resolutions (250, 500, and 1000 m); it takes measurements every day; it has a wide field of view and detects a wide spectral range of electromagnetic energy. A continual, complete coverage allows MODIS to complete an electromagnetic picture of the globe every two days (http://wamis.meraka.org.za/modis-basics; *date accessed on 10/03/2017*). MODIS

has many products which are being used by scientists of many disciplines such as oceanography, biology, and atmospheric science. For this work the focus is on the products relating to the atmosphere which are the aerosol products, cloud products, cloud mask and atmospheric profiles to name a few. The MODIS technical specifications are summarised in Table 3.5 and an example of global AOD measurements are shown in Fig. 3.9.

Table 3.5: MODIS technical specifications (http://wamis.meraka.org.za/modis-basics, date accessed on 08/03/2017)

Feature	Specification
Orbit	705 km, 10:30 a.m. descending node or 1:30 p.m.ascending node, sun synchronous, near-polar, circular
Scan rate	20.3 rpm, cross track
Swath dimensions	2330 km (across track) by 10 km (along track at nadir)
Telescope	17.78 cm diam. off-axis, afocal (collimated), with intermediate field stop
Size	1.0 x 1.6 x 1.0 m
Weight	250 kg
Power	225 W
Data rate	11 Mbps (peak daytime)
Quantization	12 bits
Spatial resolution	250 m (bands 1-2) (at nadir): 500 m (bands 3-7), 1000 m (bands 8-36)

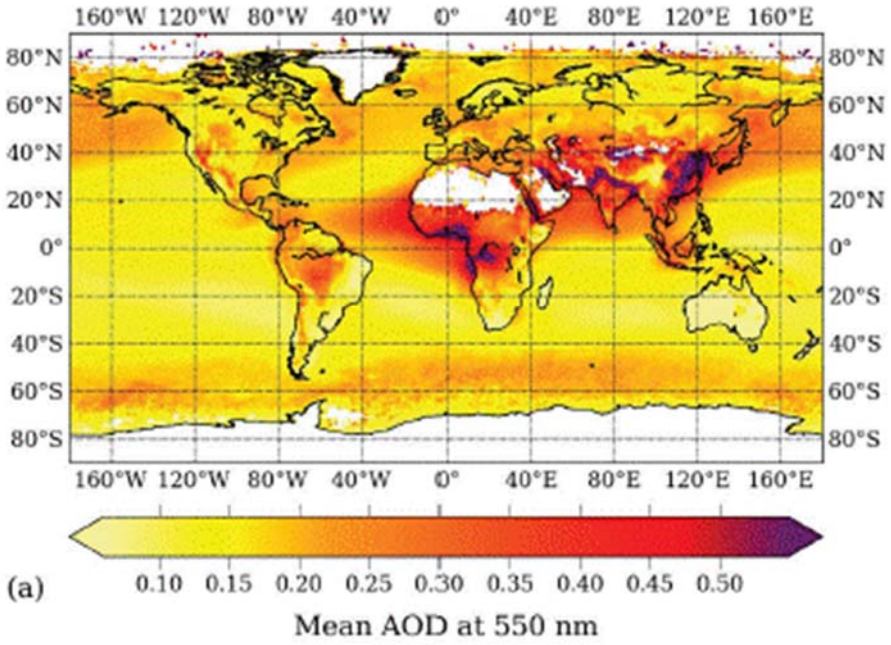

Fig. 3.9: Mean AOD of the Level 3 MODIS dataset over the globe (obtained from Ruiz-Arias et al, 2013).

3.5 CALIPSO

The Cloud-Aerosol Lidar and Infrared Pathfinder Satellite Observations (CALIPSO) spacecraft is used to study the role that clouds and aerosols play in regulating Earth's weather, climate and air quality (http://www.nasa.gov/mission_page/calipso/mission; date accessed on 10/03/2017). CALIPSO can provide information about the thickness of clouds and can determine the height and types of aerosols. The CALIPSO payload, Fig. 3.10, consists of three co-aligned nadir-viewing instruments; the Cloud-Aerosol Lidar with Orthogonal Polarization (CALIOP), the Imaging Infrared Radiometer (IIR), and the Wide Field Camera (WFC) (http://www.nasa.gov/mission_pages/calipso/spacecraft/index.html; *date accessed on 10/03/2017*).

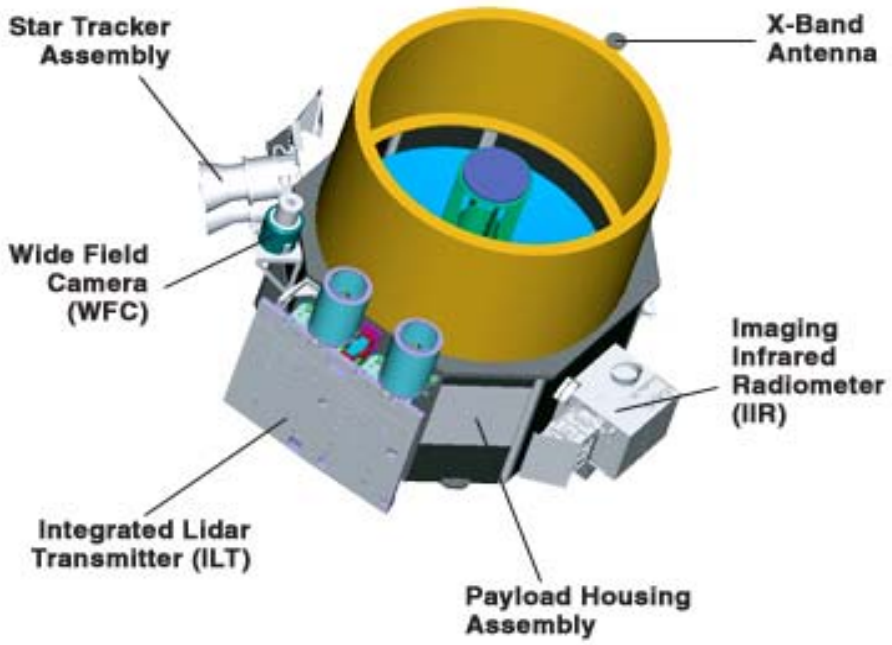

Fig. 3.10: The physical layout of the CALIPSO payload (http://www.nasa.gov/mission_pages/calipso/spacecraft/index.html; date accessed on 10/03/2017)

CALIOP is a sensitive LIDAR that provides high-resolution vertical profiles of aerosols and clouds. It has three receiver channels one measuring the 1064 nm backscatter signal and the other two channels measure the orthogonally polarized components of the 532 nm backscattered signal (Winker et al, 2007). The specifications of the CALIOP are shown in Table 3.6 and an example of the 532 nm Total Attenuated Backscatter profile from the CALIOP is shown in Fig. 3.11.

Table 3.6: CALIOP technical specifications (obtained from Winker et al, 2007)

Feature	**Specification**
Laser	Nd: YAG, diode-pumped, Q-switched, frequency doubled
Wavelength	532 nm, 1064 nm
Pulse energy	110 mJ/channel
Repetition rate	20.25 Hz
Receiver telescope	1 m diameter
532 detector	PMT
1064 detector	APD
Polarization	532 nm
Footprint/FOV	100 m/ 130 µrad
Vertical resolution	30-60 m
Horizontal resolution	333 m
Linear dynamic range	22 bits
Data rate	316 kbps

CALIOP data products are separated into two types; (a) level 1 products are composed of calibrated and geo-located profiles of the attenuated backscatter returned signal and (b) level 2 products which are derived from level 1 products and are classified in three groups: profile products, vertical feature mask (VFM) and layer products (Lopez et al, 2012). Retrieved backscatter and extinction profiles within the detected layers are provided by the profile product. Cloud and aerosol location, and also their types are provided by VFM (Lopes et al, 2012. Optical properties of aerosols and clouds integrated or averaged in the layers detected in the atmosphere are provided by the layer products.

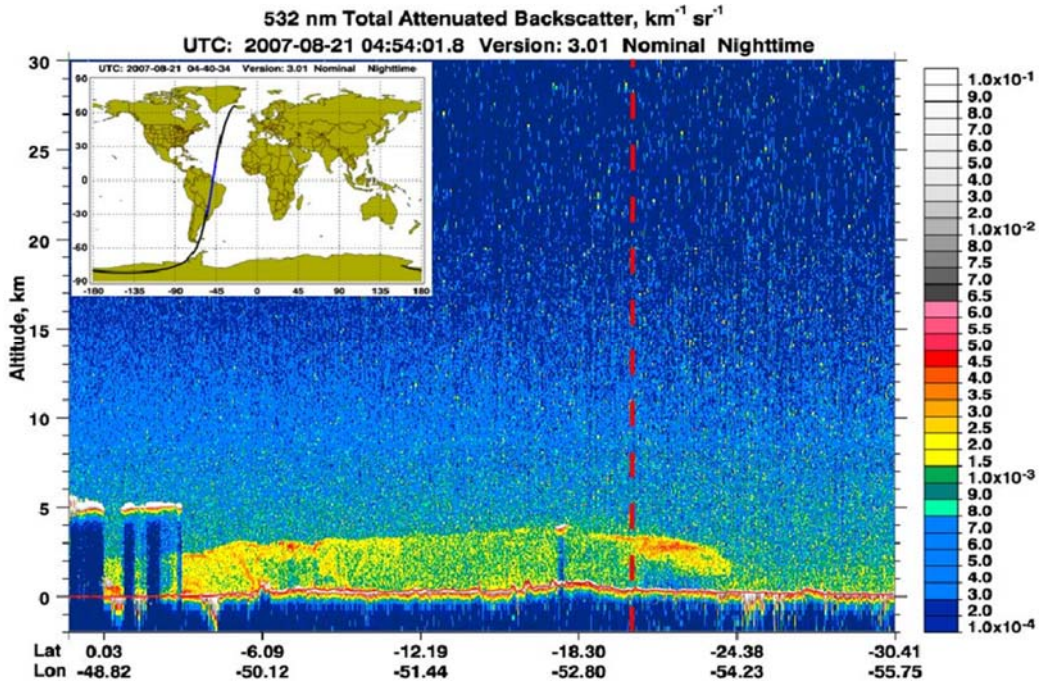

Fig. 3.11: CALIOP 532 nm Total Attenuated Backscatter profile along with the orbit track in the graphic embedded in the upper left. The dashed line in red represents the closest approach to the region of Campo Grande on 21 August 2007 around 05:00 (UTC) (obtained from Lopes et al, 2012).

References

Fernalds F. G., 1984. Analysis of atmospheric lidar observations: some comments. Applied Optics 23, 652-653

Klett J. D., 1981. Stable analytical inversion solution for processing lidar returns. Applied Optics 20, 211-220

Klett J.D., 1985. Lidar inversion with variable backscatter/extinction ratios. Applied Optics 24, 1638-1643

Lopes F. G. S., Mariano G. L., Landulfo E., Mariano E. V. C., 2012. Impacts of Biomass Burning in the Atmosphere of the Southeastern Region of Brazil Using Remote Sensing Systems, Atmospheric Aerosols - Regional Characteristics - Chemistry and Physics, Dr. Hayder Abdul-Razzak (Ed.), ISBN: 978-953-51-0728-6, InTech, DOI: 10.5772/50406.

Ruiz-Arias J. A., Dudhia J., Gueymard C. A., Pozo-Vazquez D., 2013. Assessment of the Level-3 MODIS daily aerosol optical depth in the context of surface solar radiation and numerical weather modeling. Atmospheric Chemistry and Physics 13, 675–692

Sharma A., Sivakumar V., Bollig C, van der Westhuizen C. and Moema D ,2009. System description of the mobile LIDAR of the CSIR, South Africa, South African Journal of Science, 105, 456-462

Shikwambana L., Sivakumar V., 2014. Aerosol optical depth measurements over Pretoria using CSIR LIDAR and sun-photometer: A case study. South African Society of Atmospheric sciences peer reviewed conference proceedings. ISBN 978-0-620-62777-1

Sivakumar V., Tesfaye M., Aleme W., Sharma A., Bollig C., Mengistu G., 2008. Aerosol measurements over South Africa using satellite, sun-photometer and LIDAR. Advances in Geosciences Vol. 16: Atmospheric Science, 253-262

Sivakumar V., 2012. CSIR - NLC Mobile LIDAR for Atmospheric Remote Sensing, Remote Sensing - Advanced Techniques and Platforms, Dr. Boris Escalante (Ed.), ISBN: 978-953-51-0652-4, InTech, Available from: http://www.intechopen.com/books/remote-sensing-advanced-techniques-and platforms/csirnlc- south-africa-mobile-lidar-for-atmosphere-remote-sensing

Winker D. M., Hunt W. H., McGill M. J., 2007. Initial performance assessment of CALIOP. Geophysical Research Letters 34, L19803, doi:10.1029/2007GL030135

Chapter 4

Observation of clouds using the CSIR transportable LIDAR: A case study over Durban, South Africa

4.1 Introduction

The detection of clouds in satellite imagery has a number of important applications in weather and climate studies (Jedlovec, 2009). In atmospheric remote sensing, cloud detection is an important step for the inversion of the parameters in the atmosphere such as temperature, humidity and sea surface temperature to name a few (Du et al, 2009). Equally important in sensed image processing, cloud detection is an important foundation for many applications such as forest fires detection, environmental pollution and water-body monitoring (Moghaddam and Aghamohamadnia, 2013). The National Aeronautics and Space Administration (NASA) has a constellation of satellites called the A-Train which has passive and active sensors specifically dedicated to the study of aerosol and cloud properties from a three-dimensional perspective, exploiting simultaneous and collocated multisensor observations (Waquet et al, 2009). The A-train satellites include the Aqua satellite with its Moderate Resolution Imaging Spectroradiometer (MODIS, http://modis-atmos.gsfc.nasa.gov/), CloudSat with its Cloud Profiling Radar (CPR, http://cloudsat.atmos.colostate.edu/), and the Cloud-Aerosol Lidar and Infrared Pathfinder Satellite Observations (CALIPSO), all these instruments can be used to study clouds (Setvák et al, 2013). Space-based observations have the advantage of providing global spatial coverage but they do not have sufficient temporal coverage to study many atmospheric processes (Madonna et al, 2011). Ground-based observations are necessary for the long-term monitoring of atmospheric parameters that cannot be observed from available satellite-borne sensors (Madonna et al, 2011). Ground based instruments such as

sun-photometers which makes direct sun measurements at several wavelengths in the range between 340 and 1020 nm, with a 1.2° full- field-of-view (FOV) which takes about 8 s to scan all wavelengths using a filter wheel (Guerrero-Rascado et al, 2013). Ground based radars are also used to detect and study different clouds. For example, Hollars et al (2004) used a radar system for the retrievals of cloud-top heights from the Atmospheric Radiation Measurement (ARM) 35 GHz Millimeter Wave Cloud Radar and compared to those from the Geostationary Meteorological Satellite (GMS)-5 satellites. Similar to ARM systems, the Light Detection And Ranging (LIDAR) with high sensitivity and high temporal coverage can be used for studying clouds (Hai et al, 2012). LIDAR retrieval of atmospheric parameters are an effective tool to characterize the time and spatial evolution of the atmospheric boundary layers as well as to investigate the physics properties of the cloud composing particle (Lakkis et al, 2009). A laser ceilometer is another type of a ground-based instrument that can be used to determine the height of a cloud base, cloud cover and cloud vertical structure (Costa-Surós et al, 2013). A laser ceilometer has a similar type of setup as the LIDAR, it consists of a vertically pointing laser and a receiver at the same location. Many studies and observations of clouds have been made around the world using various instruments. However, in South Africa only a few studies of this nature have been carried out using a transportable LIDAR system. Transportable LIDAR systems have an advantage over static systems as they can be moved to the desired locations where measurements want to be carried out.

For South Africa, it was found that the country could be divided into three climatic regions; the subtropical wet, the subtropical dry and the arid. The subtropical wet region is characterised by hot summer temperatures and fully humid conditions, this is observed on the eastern parts of South Africa. The subtropical dry regions are observed on the northern parts of South Africa and are characterised by warm temperatures during dry summers. The arid region is observed on the west part of South Africa and are characterised by high temperatures (Kanike and Sivakumar, 2015). However, a full description of the division of climatic areas is defined by Koppen-Gieger climate classification (Kottek et al., 2006). Fig 4.1 shows the different climatic regions found in South

Africa (http://koeppen-geiger.vu-wien.ac.at/present.htm). The Koppen-Gieger climate classification is divided into three zones; (1) the main climatic zone, (2) precipitation and (3) temperature. The color scheme on the map indicates a combination of the three zones which gives a description of the climatic condition of the area. From the regions mentioned the subtropical wet regions offers the best location for our cloud studies as it is humid and allows for a higher chance of cloud formation. Durban (29.9° S, 30.9° E) was the city chosen as it met all the requirements. Moreover, there were no cloud measurements reported using the LIDAR system. The campaign measurements performed at Durban is to understand the aerosol-cloud interaction later. The particular site had a fixed LIDAR system at the University of KwaZulu Natal but currently not operational. Moorgawa et al. (2007) has made initial results on aerosols over Durban but there were no cloud measurements reported using such LIDAR. Thus, the present study further motivates the continuation of LIDAR for atmospheric research over Durban.

In this study, the CSIR transportable LIDAR system and CALIPSO were used for observing cloud structure and study their properties. In this paper, we discuss the campaign measurements conducted in Durban, South Africa, during the end of the spring season. We show the type of clouds that were observed from 20 – 23 November 2012. In section 4.2, a description of the experimental site is given. The instruments, methodology and results are discussed in sections 4.3, 4.4 and 4.5 respectively. Conclusions are then given in section 4.6.

4.2 Experimental site

Durban is the largest urban city in the South African province of KwaZulu-Natal and its time zone is UTC+02:00. It is situated at the south-east of South Africa and it is bound to the east by the Indian Ocean (see Fig. 4.1). The city has a subtropical climate and experiences four seasons which are summer (December-February), autumn (March-May), winter (June-August) and spring (September-November). The rainy season is during late November through December and may extend into January.

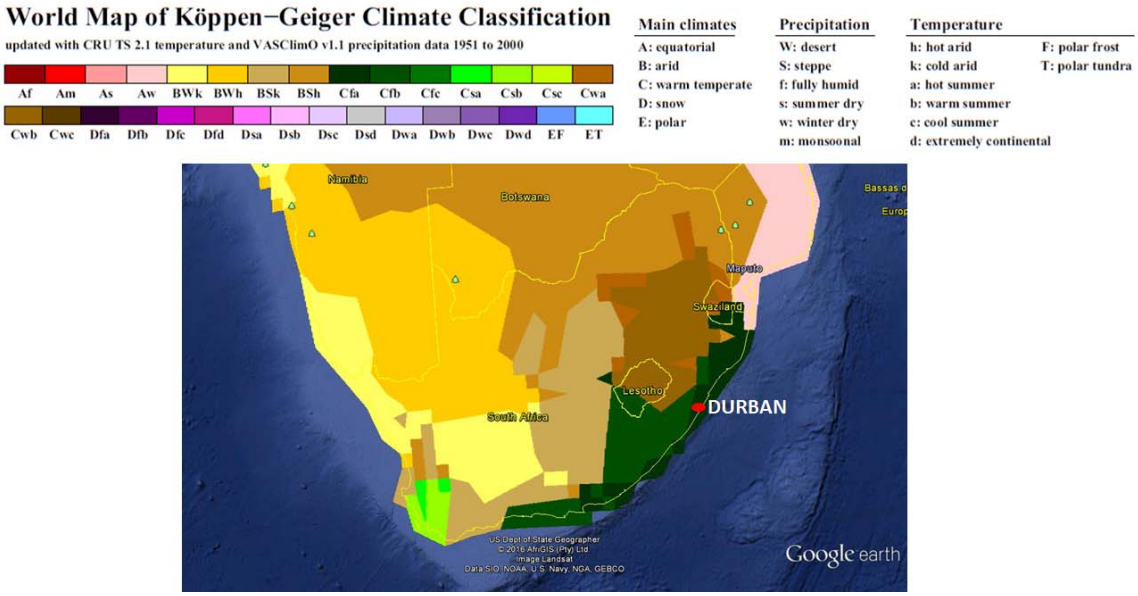

Fig. 4.1: Koppen-Gieger climate classification of South Africa representing different climatic regions (Kottek et al., 2006; http://koeppen-geiger.vu-wien.ac.at/present.htm). The map also shows the city of Durban the measurement site.

4.3. Instruments

4.3.1 CSIR transportable LIDAR system

The transportable Mie LIDAR system at the Council for Scientific and Industrial Research (CSIR), in Pretoria (25.7461° S, 28.1881° E), was developed in 2007. This LIDAR has been configured into mono-static system that maximizes the overlap of the outgoing beam with the receiver field of view (Sivakumar et al, 2012). The LIDAR system has been mounted in a transportable platform with a special shock absorber frame to maximise stability (Sivakumar et al, 2012; Sharma et al, 2009). Fig. 4.2 shows the layout of the experiment with the three main sections of the LIDAR system, namely the transmission, receiver and data acquisition sections. Specifications of the CSIR LIDAR system are shown in Table 4.1. More details about the LIDAR can be found in an earlier article on system characteristics by Sharma et al (2009).

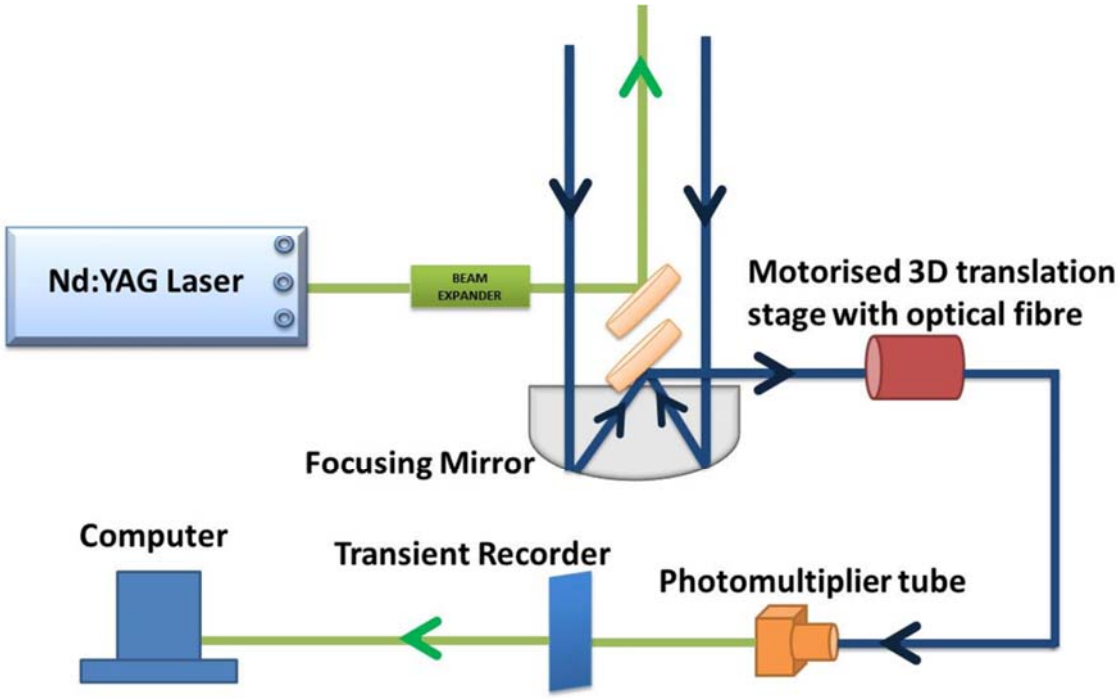

Fig. 4.2: Schematic layout of the CSIR-NLC mobile LIDAR system.

4.3.2 CALIPSO

The Cloud-Aerosol Lidar and Infrared Pathfinder Satellite Observations (CALIPSO) can provide information about the thickness of clouds and can determine the height and types of aerosols. CALIPSO consists of three co-aligned nadir-viewing instruments; the Cloud-Aerosol Lidar with Orthogonal Polarization (CALIOP), the Imaging Infrared Radiometer (IIR), and the Wide Field Camera (WFC). CALIOP is a sensitive LIDAR that provides high-resolution vertical profiles of aerosols and clouds. CALIOP products can be separated into two levels: (a) level 1 products are composed of calibrated and geo-located profiles of the attenuated backscatter returned signal and (b) level 2 products which are derived from level 1 products and are classified in three types: layer products, profile products and vertical feature mask (Lopes et al, 2012). The CALIOP is sensitive to the presence of thin cloud layers and, its range resolution of 333 m can identify small boundary layer clouds, especially in the absence of optically thick, high clouds where low clouds most dramatically impact the fluxes of shortwave radiation (Medeiros et al, 2010). Table 4.1 shows the specifications of the CALIPSO.

Table 4.1: Specifications of the CALIPSO and CSIR LIDAR system

Feature	**CALIPSO**	**CSIR LIDAR**
Laser	Nd: YAG, diode-pumped, Q-switched, frequency doubled	Nd:YAG, Q-switched, flash lamp-pumped (Continuum®, PL8010)
Wavelength	532 nm, 1064 nm	532 nm
Pulse energy	110 mJ/channel	140 mJ
Repetition rate	20.25 Hz	10 Hz
Receiver telescope	1 m diameter	0.404 m
532 detector	PMT	PMT
1064 detector	APD	-
Polarization	532 nm	532 nm
FOV	130 µrad	500 µrad
Vertical resolution	30-60 m	10 m

4.4.4. Data analysis and Methodology

The LIDAR measurements were carried out from the 20th of November 2012 until the 23rd of November 2012. The time duration of measurements depended on the weather situation for that day. For example, on the 20th of November 2012 the measurement were carried out from 10:59 local time to around 15:50 when it started to drizzle, the measurements were then discontinued. The weather varied for the different days of the measurements.

The backscatter signals were collected and their intensities measured. In general, the received signal intensity is described in terms of the LIDAR equation as given by Bangia et al (2011);

$$P(r) = P_o \frac{c\tau}{2} A \frac{\beta(r)}{r^2} e^{-2\int_0^r \sigma(r')dr'} \tag{4.1}$$

where P_o is the transmitted laser power in terms of photon counts at 532 nm, c is the velocity of light, τ is the pulse duration, A is the effective system receiver area, $\beta(r)$ is the backscattering coefficient, $\frac{1}{r^2}$ is the range dependence factor that

accounts for the decrease in solid angle subtended with the square of the range, $e^{-2\int_0^r \sigma(r)dr'}$ is the integrated two-way extinction of the signal as it propagates from the instrument to the scattering volume at range r and returns back. The method mostly used for inverting elastic LIDAR returns is the backward inversion method. The Klett inversion requires an input value of the extinction coefficient at the far boundary of the LIDAR range. This boundary value can be measured or assumed.

The backscattering and extinction coefficients are given by contribution of both aerosols and molecules and are expressed as:

$$\beta(r) = \beta_{aer}(r) + \beta_{mol}(r) \tag{4.2}$$

$$\sigma(r) = \sigma_{aer}(r) + \sigma_{mol}(r) \tag{4.3}$$

where subscript (*aer*) and (*mol*) indicate aerosols and molecules, respectively. Molecular contributions were calculated using data from CIRA 1986 standard atmosphere model (Bangia et al, 2011). The molecular backscatter coefficient $\beta_{mol}(r)$ is estimated by considering the theoretical molecular LIDAR ratio $S_{mol} = \sigma_{mol} / \beta_{mol}$ as $8\pi/3\ sr$, under the condition of zero molecular absorption (Bangia et al, 2011). The backward inversion method can be expressed as Bangia et al (2011):

The total backscatter coefficients are derived from the backward inversion method and can be expressed as (Bangia et al, 2011):

$$\beta_{aer}(r) + \beta_{mol}(r) = \frac{X(r)\exp\left[-2\left(S_{aer}(r) - S_{mol}\right)\int_{r_c}^{r}\beta_{mol}(r)dr\right]}{\frac{X(r_c)}{\beta_{aer}(r_c) + \beta_{mol}(r_c)} - 2S_{aer}\left\{\int_{r_c}^{r} X(r)\exp\left[-2\left(S_{aer}(r) - S_{mol}\right)\int_{r_c}^{r}\beta_{mol}(r')dr'\right]dr\right\}} \tag{4.4}$$

where $X(r)$ is the range normalized signal given by $P(r)r^2$ and r_c is the reference height. One advantage of using the backward inversion method is that when we start integrating from the far end of the LIDAR sounding path we can avoid producing negative values of $\beta_{aer}(r)$ (Stoyanov et al, 2012). For more details, the reader may refer to Bangia et al. (2011).

Aerosol optical depth (AOD) is calculated by integrating the extinction coefficient from cloud base to its top (Krishnakumaret al, 2014)

$$AOD = \int_{Z_b}^{Z_t} \alpha(r)\, dr \tag{4.5}$$

where Z_t is the cloud top, Z_b is the cloud base and $\alpha(r)$is the aerosol extinction coefficient.

4.5. Results and discussion

4.5.1. CSIR - LIDAR observations

LIDAR measurements were carried out on 20, 21, 22 and 23 November 2012 in Durban (see Fig. 4.3). On the 20th of November 2012 the backscatter signal from the LIDAR (where red indicates a strong backscatter) revealed the presence of a cloud layer. The cloud was observed at an altitude of around 500 m from 10:59 until it started raining at around 15:50 local time (see Fig. 4.3a). The cloud had a thickness of about 100 m. (Note that the CSIR- LIDAR has capability for providing range resolution of 10 m). On the 21st of November 2012 two layers of clouds at the heights of 600 and 1400 m were observed between 10:40 and 12:00 local time (see Fig. 4.3b). The backscatter signal indicated that the lower level cloud at 600 m did not have a large amount of liquid water content in it, thus allowing the laser to penetrate through it, and enabled the detection of the other layer of clouds at approximately 1400 m. The cloud at a height of 600 m showed a thickness of about 100 m while the other layer at a height of 1400 m indicated a thickness of approximately 70 m. However, the upper cloud layer could not be observed at the local time of 13:01 until 13:45 but a strong backscatter signal was observed at the height of 600 m. This indicates that the laser might not penetrate through the clouds (optically opaque) thus the other layer could not be observed, if there were any. On the 22nd of November 2012 multi-layered clouds were briefly observed between 13:10 until 13:28 local time (see Fig. 4.3c). The lower level clouds were observed at 600 m and the upper level clouds were observed at 1000 m with thickness of about 100 m. On the 23rd of November 2012 a single layer cloud at a height of 10000 -12000 m was observed (see Fig. 4.3d). The

backscatter signal was moderate at a height of 11000 m and the strength of the signal weakened with increasing height.

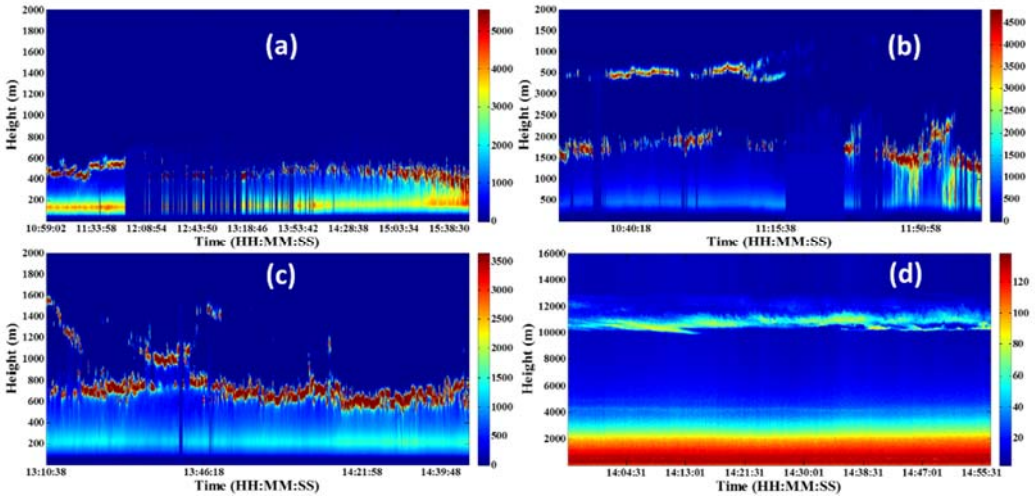

Fig. 4.3: Height-time colour map of CSIR transportable LIDAR backscatter signal returns at daytime in Durban on (a) 20 November 2012 (b) 21 November 2012 (c) 22 November 2012 and (d) 23 November 2012 UTC+02:00.

A similar method used by Venema et al. (2000) to identify clouds directly from the extinction coefficient profiles was used. In this method the height at which the signal decreases/increases considerably is called cloud top/ base. For aerosols the extinction coefficients profiles generally show a decrease in extinction coefficient values with increasing height and clouds generally show sudden high values on the profile. The aerosol extinction coefficient profiles for 20, 21, 22 and 23 November 2012 are shown in Fig. 4.4. On 20, 21 and 22 November 2012 low level clouds were observed. On these days, an aerosol layer was observed at altitudes of ~ 100- 400 m. On the 20th of November 2012 a layer of cloud was observed between 400 and 500 m (see Fig. 4.4a), and demonstrated an extinction coefficient value of 0.018 m^{-1}. On the21st of November 2012 (see Fig. 4.3b) multi-layered clouds were also observed. Thin cloud layers at 600, 700 and 800 m were observed from the extinction coefficient profiles which were not so visible in Fig. 4.3b. These cloud layers showed extinction coefficients values of 0.003, 0.0118 and 0.0117 m^{-1} respectively. There was also a cloud layer at 1500 m with an extinction coefficient value of 0.009 m^{-1}. On the 22nd of November 2012 (see Fig.

4.4c) multiple layers of clouds were observed at 600, 1000, 1200 and 1500 m with extinction coefficients values of 0.0012, 0.0044, 0.0013 and 0.0009 m^{-1} respectively. On the 23rd of November 2012 (see Fig. 4.4d) cloud layers at 10000 and 11000 m with extinctions coefficients values of 0.000001 and 0.000002 m^{-1} were observed. The extinction coefficients of low-level clouds had values in the range of 0.018-0.0009 m^{-1} depending upon the thickness of cloud. Thicker clouds showed higher values of extinction coefficients compared to thinner clouds.

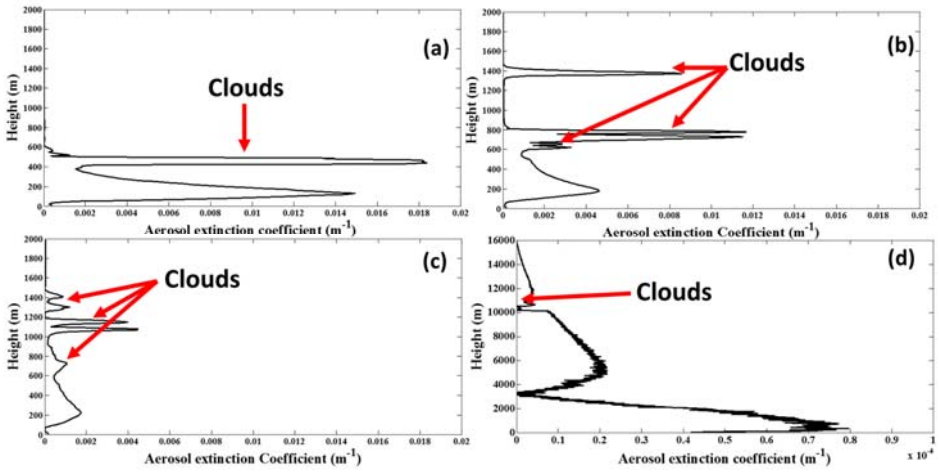

Fig. 4.4: The retrieved aerosol extinction coefficients using the LIDAR on (a) 20 November 2012 (b) 21 November 2012 (c) 22 November 2012 and (d) 23 November 2012.

The temporal evolution of the aerosol optical depth (AOD) was retrieved for the four days of measurements in Durban (see Fig. 4.5) using equation 4.5. On the 20th of November 2012 an overall increase of the AOD was observed from the morning (10:59) to the afternoon (15:40) from 0.35 to 0.6 (see Fig. 4.5a). On 21 November 2012 a similar trend was also observed with AOD increasing from 0.3 to 1 (see Fig. 4.5b). However, on 22 November 2012 a small change in AOD was observed from 0.1 to 0.15 (see Fig. 4.5c). Platt et al. (1989) mentioned that the change in optical depth depends on the nature of composition and the thickness of the cloud. However, on 23 November 2012 a steady AOD value of ~0.02 was observed (see Fig. 4.5d).

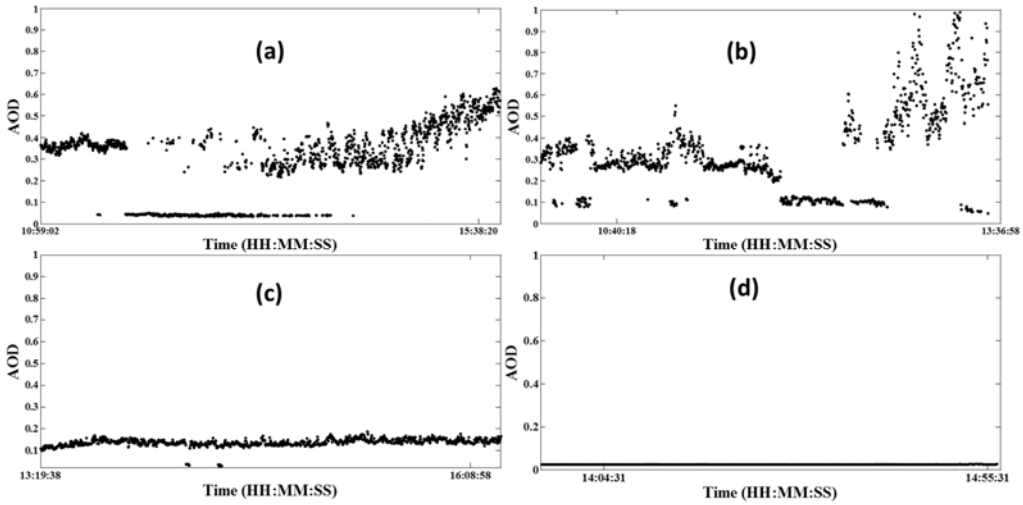

Fig. 4.5: Temporal evolution of AOD on (a) 20 November 2012 (b) 21 November 2012 (c) 22 November 2012 and (d) 23 November 2012.

4.5.2 Cirrus clouds observed on 23 November 2012

Throughout the campaign, cirrus clouds were only observed on 23 November 2012. Most of these clouds are found between the height of 5.5 km and 12.5 km, with height range thicknesses spanning 1.8–3.1 km, see Fig. 4.6. Sassen et al (1990) and Jensen et al (1996) have ascribed the outflows from cumulonimbus anvils to the formation of thick cirrus clouds to mid and high altitudes. These types of clouds arise due to the vertical mixing of air from the entrainment and detrainment. It is also suggested that the ice water gradient is largely destroyed due to sturdy mixing by the strong cloud circulation (Sivakumar et al, 2003). The optical properties of this cloud were compared to cirrus clouds observed in the southern hemisphere, see Table 4.2. From the reported cirrus clouds in Table 4.2 it can be seen that the cirrus clouds over Durban had the lowest cloud height base of 5.5 km. These are very low cirrus clouds but over time they were found to disappear. However, the average cloud thickness is similar to that observed by Lakkis et al (2009). This correlation does somehow suggest that the cirrus cloud properties may depend on climate conditions and geographical location. However, a more wider climatological study needs to be carried out to confirm the dependence of climate conditions and geographical location.

Table 4.2: Cirrus cloud properties observed by LIDAR

	Location (AGL) (Distance from shoreline)	Cloud top height (km) - maximum	Cloud base height (km) - minimum	Cloud thickness (km)	Distance to tropopause (km)
Durban	29.9° S, 30.9° E (8 m) (±14 km)	12.5	5.5	2.45	-
(Buenos Aires) Lakkis et al., 2009	34.6°S,58.5°W (31 m)	11.82	9.63	2.41	0.38
(Punta Arenas) Immler et al., 2002	53.1°S,71°W (30 m)	9.5	8.8	1.4	1.7

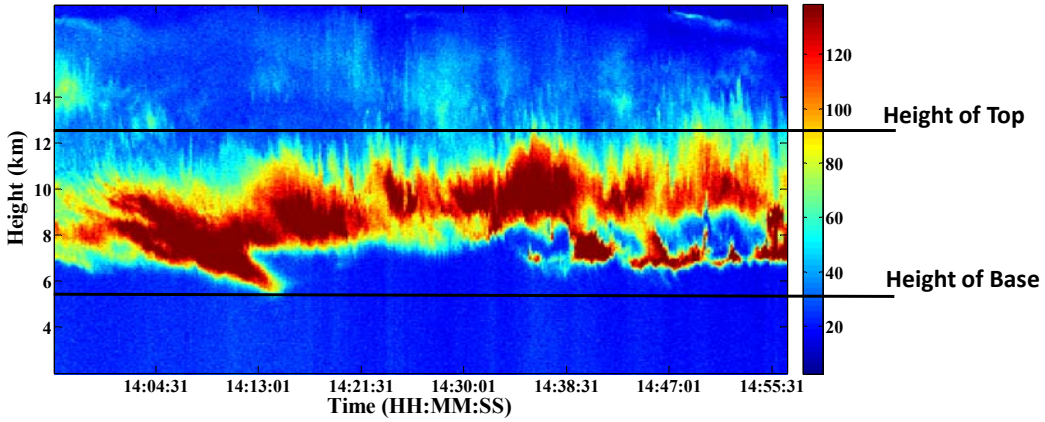

Fig. 4.6: Height-time colour map of CSIR transportable LIDAR signal returns, illustrating the presence of cirrus clouds on 23 November 2012 over Durban. The cloud height top and cloud height bottom are indicated by the thick dark lines.

4.5.3 CALIPSO and CSIR LIDAR comparison

The only comparable CALIPSO data which were available during the operation of the CSIR LIDAR were on 20 and 22 November 2012. For 21 and 23 November 2012 the satellite observations were too far from the measurement site. Fig. 4.7(a) and (b) shows colour coded time-height images of the daytime level-1 data at 532 nm acquired by CALIPSO on 20 and 22 November 2012 respectively. On 20 November 2012 the nearest coincidence between the CSIR LIDAR and the CALIPSO occurred around 12:05 local time. The aerosol layer was observed around 1 km. No clouds were observed in the lower part of the troposphere by the CALIPSO at the observation site (latitude -29.9^{o}). However, it has illustrated the presence of clouds at 8-13 km with a thickness ~ 3 km; these clouds were not observed by the CSIR LIDAR system. This suggests that the thick cloud observed by the CSIR LIDAR caused most of the photons of the laser to be absorbed and, thus a few photons penetrating through the cloud. As a result these few photons could not detect the clouds at those heights as they could have been scattered or absorbed along the way. On 22 November 2012 a similar cloud at a height of 8-13 km was observed. However, on this day a layer of cloud was observed at the height of ~ 4.5 km by the CALIPSO. The CSIR LIDAR gives a better description of the atmospheric conditions in the first few kilometers of the troposphere for cloudy conditions whereas the CALIPSO gives better information at the top of the troposphere. Further, it indirectly also addresses the strength of the signal which is higher at lower heights (as it is penetrating upwards) while the satellite data looks downward where the signal strength is higher at the top. Thus, the two instruments complement each other to give a description of clouds in the troposphere even for cloudy conditions.

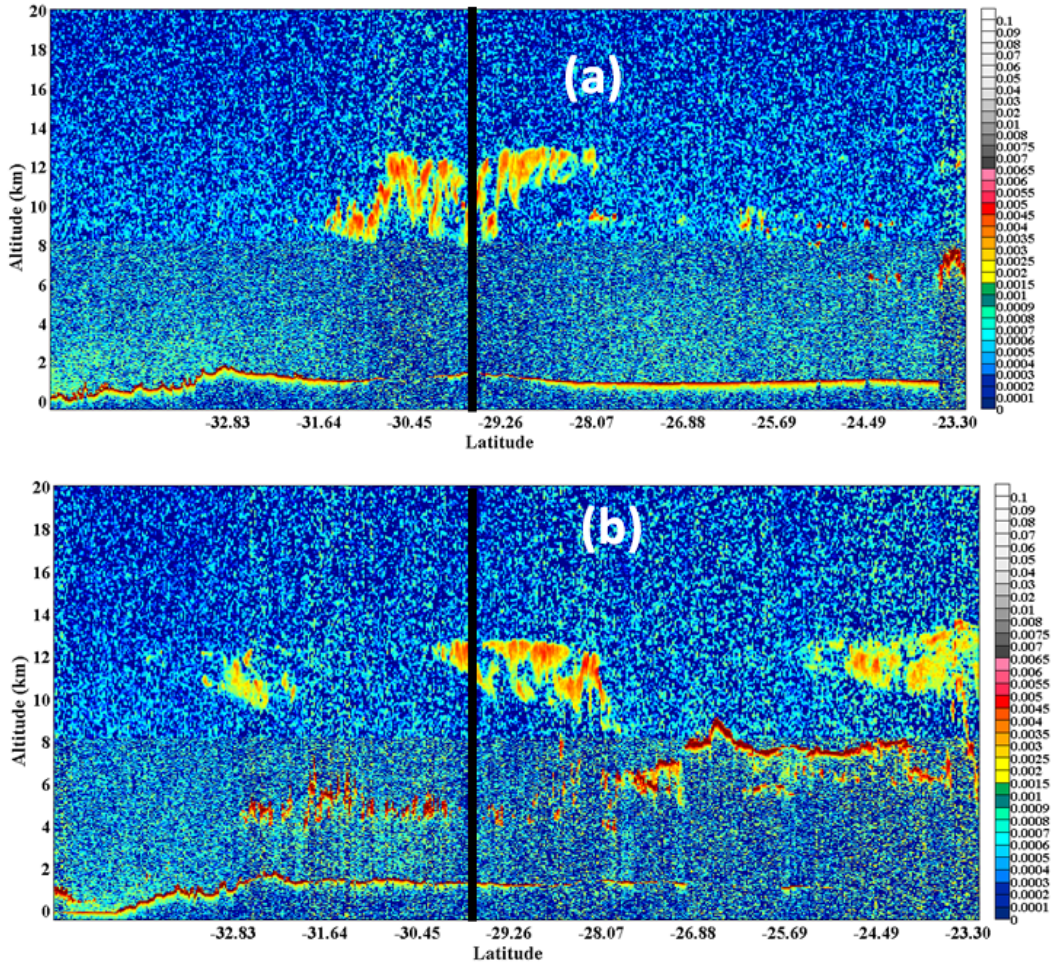

Fig. 4.7: Height-time-colour map of CALIPSO-derived total attenuated backscatter at 532 nm on (a) 20 November 2012 at 12:05 and (b) 22 November 2012 at 11:52 UTC+02:00.

The mean extinction coefficient profiles from the CALIPSO Level 2 aerosol product is shown in Fig. 4.8. On 20 November 2012 the highest value of extinction coefficient of ~0.08 km^{-1} was observed at a height of about 5 km (see. Fig. 4.8a). From Figure 4.8a this indicates the presence of a thin cloud at that altitude. High level clouds at the heights of 6-11 km were observed from the extinction coefficient data. However, on the lower part of the troposphere a thick single layer of cloud around 1.8 km was observed. It can also be observed that different layers of clouds were present at different altitudes from 1.8 km to 11 km. These, however, were not so clear in Fig. 4.7a and b. The negative extinction

coefficient values are found to be noise in the CALIPSO signal when aerosol loading is low and background noise is high. On 22 November 2012 the extinction coefficient profile showed the presence of a thick cloud at around 3 km (see Fig. 4.8b) while the aerosol layer was observed at about 1.5 km. However, no extinction coefficients were observed at high altitudes indicating the absence of clouds.

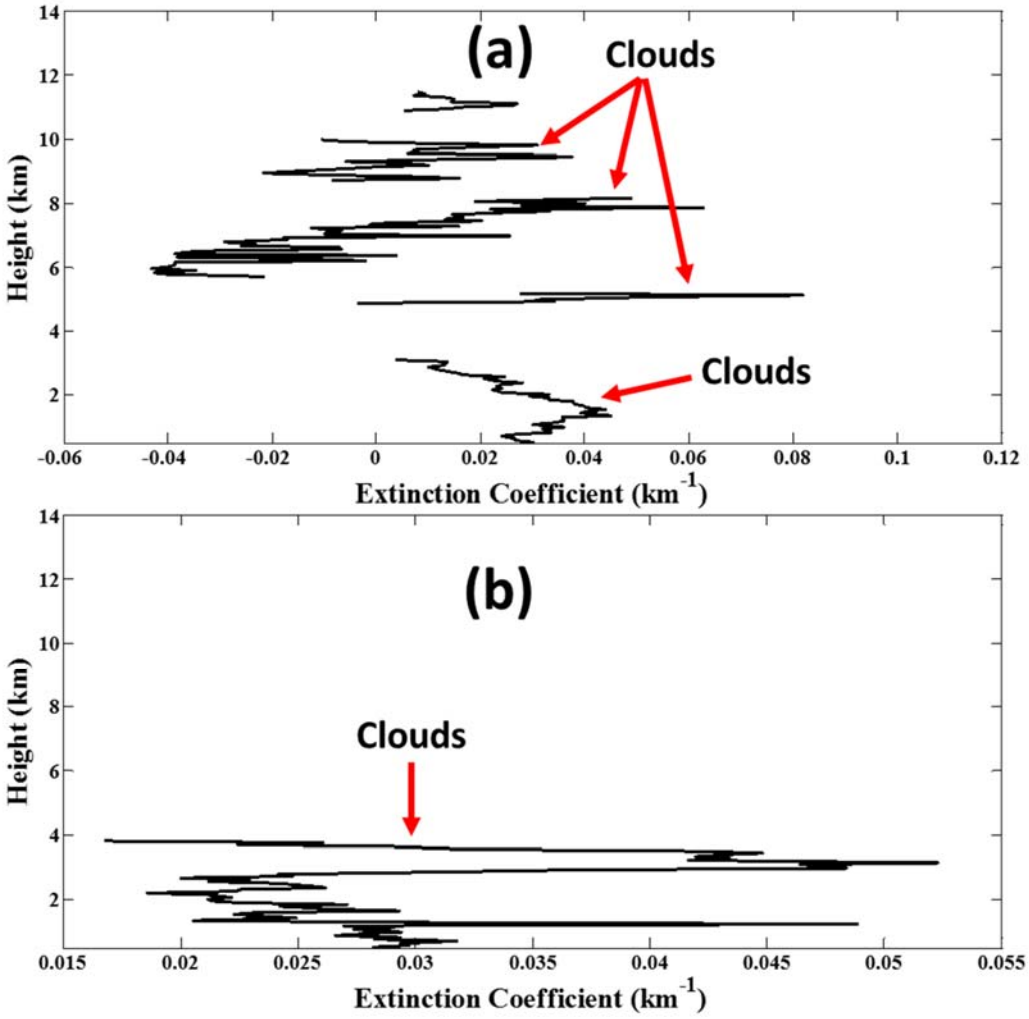

Fig. 4.8: Height profile of eextinction coefficient observed from CALIPSO on (a) 20 November 2012 and (b) 22 November 2012.

4.6. Conclusion

Campaign measurements over Durban (29.9° S, 30.9° E) have been carried out due to favourable meteorological conditions for cloud formations and to perform aerosol-cloud interactions studies in future. Clouds over Durban (29.9° S, 30.9° E) during the spring (early summer) season were observed using a transportable LIDAR system. Cloud layers on the lower atmosphere were observed on 20 – 22 November 2012 while high level clouds were observed on 23 November 2012. The low level cloud layers have high extinction coefficients values ranging from 0.0009 to 0.018 m^{-1}, whereas low extinction coefficients for high level clouds were observed at values ranging between 0.000001 and 0.000002 m^{-1}. The vast difference in the extinction coefficient suggests that there are remarkable differences in optical characteristics between low and high level clouds. The high level clouds could be classified as Cirrus clouds based on the altitude they were detected. The calculated AOD showed a high variability for 20 and 21 November 2012. This indicates a change in the composition and/or thickness of the cloud. However, a constant value of the optical depth on 23 November suggested a static cloud composition and/or thickness. Comparable LIDAR and CALIPSO data was available on 20 and 22 November 2012 and indicated that the CALIPSO could observe high level clouds while the CSIR LIDAR could not. However, the two instruments complement each other well to describe the cloudy condition.

References

Alpert P., Kishcha P., Shtivelman A., Krichak S. O.,andJ. H. Joseph, 2004: Vertical distribution of Saharan dust based on 2.5-year model predictions, *Atmospheric Research*, 70, 109–130

Antuña J. C., Robock A., Stenchikov G. L., Thomason L. W., and J. E,Barnes, 2002:Lidar validation of SAGE II aerosol measurements after the 1991 Mount Pinatubo eruption, *Journal of Geophysical research*, 107, 10.1029/2001JD001441

Bangia T., Omar A., Sagar R, Kumar A., Bhattacharjee S, Reddy A., Agarwal P. K., Phanikumar, 2011: Study of atmospheric aerosols over the central Himalayan region using a newly developed Mie light detection and ranging system: preliminary results, *Journal of Applied Remote Sensing*, 5, 053521, 1-12

Bangia T, Kumar A., Sagar R., Agarwal P. K., and S. K. Singh, 2011: Development of Mie LIDAR system and initial cloud observations over Central Himalayan region, *Scientific Research and Essays*, 6, 896-907

Cadet B., Goldfarb L., Faduilhe D, Baldy S., Giraud V., Keckhut P., and A. Re´chou, 2003: A sub-tropical cirrus clouds climatology from Reunion Island (21^{o}S, 55^{o}E) lidar data set, *Geophysical research letters*, 30, 3, 30-1-4

Calinoiu D., Ionel I. and G.Triftordai., 2011: Analysis of Aerosol Optical Thickness in Timisoara from AERONET Global Network Observations, *Strojarstvo*, 53, 353-358

Costa-Surós M., Calbó J., González J. A.,andJ. Martin-Vide, 2013: Behavior of cloud base height from ceilometer measurements, *Atmospheric Research*, 127, 64–76

Deng X., Shi C., Wu B., Chen Z., Nie S., He D.,andH. Zhang, 2012: Analysis of aerosol characteristics and their relationships with meteorological parameters over Anhui province in China, *Atmospheric Research*, 109-110, 52–63

Du H., Wang Y. and Y. Chen, 2009: Studies on Cloud Detection of Atmospheric Remote Sensing Image Using ICA Algorithm, *2nd International Congress*

on Image and Signal Processing, 2009. CISP ' '09, 1-4

Guerrero-Rascado G. L., Costa M. J., Silva A. M., and F. J.Olmo, 2013: Retrieval and variability analysis of optically thin cloud optical depths from a Cimel sun-photometer, *Atmospheric Research*, 127, 210–220

Hai B.V., Trung D.V, Tuan N. X., Thang D.D., Binh N. T., 2012. Monitoring Cirrus Clouds and tropopause height over Hanoi using a compact LIDAR system, Communications in Physics, 22, 357-364

Hollars S., Fu Q., Comstock J, and T. Ackerman, 2004: Comparison of cloud-top height retrievals from ground-based 35 GHz MMCR and GMS-5 satellite observations at ARM TWP Manus site, *Atmospheric Research*, 72, 169–186

Immler F., Schrems, O., 2002. Lidar measurements of cirrus clouds in thenorthernand southern midlatitudes during INCA (55°N, 53° S): a comparative study.*Geophysical Research Letters*, 29, 1809. doi:10.1029/2002GL015077

Jedlovec G., 2009: Automated detection of clouds in satellite imagery. *Advances in Geoscience and Remote Sensing*, 303–316

Jensen, E. J., Toon O. B., Selkirk H. B.,Spinhirne J. D., M.R,.Schoeberl, 1996. On the formation and persistence of subvisible cirrus clouds near the tropical tropopause, *Journal of Geophysical Research*, 101, 21,361–21,375

Kanike R. K, and V. Sivakumar, 2015: *Remote sensing of Aerosol using a sunphotometer*, ISBN 978-3-659-70622-6

Keckhut P., Perrin J-M, Thuillier G., Hoareau C., Porteneuve J., N.Montoux, 2013: Subgrid-scale cirrus observed by lidar at mid-latitude: variability effects of the cloud optical depth, *Journal of Applied Remote Sensing*, 7, 1-15

Kottek M., Grieser, J., Beck, C., Rudolf, B., R. Franz, 2006: Worldmap of the Koppne-Geiger climate classification updated.*MeteorologischeZeitschrift*, 15, 259-263

Krishnakumar V., Satyanarayana M., Radhakrishnan S. V., Dhaman R. K., Pillai V. P. M., Raghunath K., Ratnam M. V., Rao D. R., P. Sudhakar,SelvanJayeshlal G. S., Motty G. N. S., Pillai V. P. M., Karnam

Raghunath K., Ratnam M. V., PSudhaka, 2014: Lidar investigations on the optical and dynamical properties of cirrus clouds in the upper troposphere and lower stratosphere regions at a tropical station, Gadanki, India (13.5°N, 79.2°E), *Journal of Applied Remote Sensing*, 8, 083659-1 – 21

Lakkis S.G., Lavorato M.,andP. O. Canziani, 2009: Monitoring cirrus clouds with lidar in the Southern Hemisphere: A local study over Buenos Aires. 1. Tropopause heights, *Atmospheric Research*, 92, 18–26

Larroza E.G., Nakaema W.M., Bourayou R., Hoareau C., Landulfo C., and P. Keckhut.,2013: Towards an automatic Lidar cirrus cloud retrieval for climate studies, *AtmosphericMeasuremnets Techniques. Discuss*, 6, 4087–4121

Lopes F. G. S., Mariano G. L., Landulfo E. andE.V.C. Mariano, 2012: Impacts of Biomass Burning in the Atmosphere of the South eastern Region of Brazil Using Remote Sensing Systems, *Atmospheric Aerosols - Regional Characteristics* - Chemistry and Physics, Dr.Hayder Abdul-Razzak (Ed.), ISBN: 978-953-51-0728-6, InTech, DOI: 10.5772/50406

Madonna F., Amodeo F., Boselli A., Cornacchia C., Cuomo V., D'Amico G., Giunta A., Mona L, and G. Pappalardo, 2011: CIAO: the CNR-IMAA advanced observatory for atmospheric research, *Atmospheric Measurement Techniques*, 4, 1191–1208

Medeiros B., L. Nuijens, C. Antoniazzi, and B. Stevens, 2010: Low - latitude boundary layer clouds as seen by CALIPSO*, Journal of Geophysical Research*, 115, D23207

Moghaddam Y. J. andM. Aghamohamadnia, 2013: A Novel method for cloud detection in MODIS imagery, *International Archives of the Photogrammetry, Remote Sensing and Spatial Information Sciences*, XL-1/W3, 1-4

Moorgawa A., Bencherif H., Michaelis M. M., Porteneuve J., and S. Malinga, 2007: The Durban atmospheric LIDAR, *Optics & Laser Technology*, 39, 306-312

Parameswaran K.B. V. Thampi, and S. V. Sunilkumar, 2010: Latitudinal dependence of the seasonal variation of particulate extinction in the UTLS

over the Indian longitude sector during volcanically quiescent period based on lidar and SAGE-II observations, *Journal of Atmospheric and Solar-Terrestrial Physics*, 72, 1024–1035

Platt C. M. R., J. D. Spinhirne, and W. D. Hart, 1989: Optical and microphysical properties of a cold cirrus cloud: Evidence for regions of small ice particles, *Journal of Geophysical Research*, 94, 11,151–11,164

Radhakrishnan S. R., Satyanarayana M., Krishnakumar V., Pillai M. V. P., Raghunath K., Ratnam M.V., Rao D. R., 2010. Optical properties of cirrus clouds at a tropical Indian station Gadanki, Tirupati (13.5°N, 79.2°E), *Journal of Applied Remote Sensing*, 4, 043559, 1-16

Repasky K. S., ReaganJ. A., Nehrir A. R., Hoffman D. S., Thomas M. J., CARLSTEN J. L. Shaw J. A.,and G. E. Shaw, 2010:Observational Studies of Atmospheric Aerosols over Bozeman, Montana, Using a Two-Color Lidar, a Water Vapor DIAL, a Solar Radiometer, and a Ground-Based Nephelometer over a 24-h Period, *Journal of Atmospheric and oceanic technologies*, 28, 320-336

Roy D.P., Borak, J.S., Devadiga, S., Wolfe, R.E., Zheng, M.,andJ. Descloitres, 2002: The MODIS Land product quality assessment approach, *Remote Sensing of Environment*, 83, 62-76

Sassen K., A. W. Huggins, A. B. Long, J. B. Snider, and R. J. Meitin, 1990. Investigations of a winter mountain storm in Utah. part II: Mesoscale structure, supercooled liquid water development, and precipitation processes, *Journal of Atmospheric Sciences*, 47, 1323–1350

Setvák M., Bedk K., Lindsey D. T., Sokol A., Šťástka Z. C.J., and P. K. Wang, 2013: A-Train observations of deep convective storm tops, *Atmospheric Research*, 123, 229–248

Sharma A., Sivakumar V., Bollig C, van der Westhuizen C. and D. Moema,2009: System description of the mobile LIDAR of the CSIR, South Africa, *South African Journal of Science*, 105, 456-462

Sivakumar V., 2012: CSIR - NLC Mobile LIDAR for Atmospheric Remote Sensing, Remote Sensing - Advanced Techniques and Platforms, Dr. Boris Escalante (Ed.), ISBN: 978-953-51-0652-4

Sivakumar V., Y. Bhavanikumar, P. B. Rao, K. Mizutani, T. Aoki, M. Yasui, and T. Itabe, 2003: Lidar observed characteristics of the tropical cirrus clouds, *Radio Science*, 38. doi:10.1029/2002RS002719

Sivakumar V, Tesfaye M., Alemu W., Moema D., Sharma A., Bollig C. and G. Mengistu,2009: CSIR South Africa mobile LIDAR—First scientific results: comparison with satellite, sun photometer and model simulations, *South African Journal of Science*, 105, 449-455

Stoyanov D., Grigorov I., Kolarov G., Peshev Z. and T. Dreischuh, 2012: LIDAR Atmospheric Sensing by Metal Vapor and Nd:YAG Lasers, *Advanced Photonic Sciences*, Mohamed Fadhali (Ed.), ISBN: 978-953-51-0153-6

Tao W.-K., Chen J.-P., Li Z., Wang C., and C. Zhang, 2012: Impact of aerosols on convective clouds and precipitation. Reviews of Geophysics, 50, doi:10.1029/2011RG000369

Veerabuthiran S., Razdan A. K, Jindal M. K., Dubey D. K., and R. Sharma, 2011: Mie lidar observations of lower tropospheric aerosols and clouds, *SpectrochimicaActa Part A*, 84, 32– 36

Waquet F., Riedi J., Labonnote L. C., Goloub P., Cairns B., Deuze´ J- L, and D. Tanre, 2009: Aerosol Remote Sensing over Clouds Using A-Train Observations, *Journal of the Atmospheric Sciences*, 66, 2468-2480

Venema V.,Russchenberg H., Apituley A., van Lammeren A. and L. Ligthart, 2000: Cloud boundary height measurements using lidar and radar, *Physics and Chemistry of the Earth*, 24, 129-134

Chapter 5

Investigation of aerosol optical characteristics and trends over different locations in South Africa using satellite, model simulation and LIDAR

5.1. Introduction

Aerosols play an important role in Earth's climate through aerosol radiative forcing (Xu et al, 2014; Gonget al, 2014) and the co-existence of both scattering and absorbing aerosols complicates this atmospheric phenomenon. The level of scattering and absorption by aerosols depends on their physical and chemical characteristics (Menon et al, 2014; Kaskaoutis et al, 2006). The aerosol optical depth (AOD) is the most important parameter used to quantify the impact of aerosols on radiative energy budget (Ge et al, 2011). AOD is an index of the attenuation of solar radiation due to the presence of aerosols and it is derived from measurements of direct solar radiation (Shahgedanova and Lamakin, 2005). The fine mode fraction (FMF) is another important parameter which has been used as a proxy for distinguishing anthropogenic from natural aerosols (Jones and Christopher, 2011). FMF is defined as the ratio of fine mode (in the micron region) AOD to the total AOD. Some examples of aerosols with high FMF are black carbon (BC) and sulphates (SO_4) which are mostly fine (small) mode in nature. By comparison, dust and sea-salts have low FMF and are predominately larger (coarse).

In the past, air pollution has been widely discussed primarily because of its health and environmental effects. Chemical emissions from factories, dust, pollen and emissions from vehicles may be suspended as particles in the atmosphere thus contributing to air pollution. Pollutants such as BC, sulphate, nitrogen dioxide (NO_2) and carbon monoxide (CO) are known to be harmful and can lead to health problems. BC aerosols are produced from anthropogenic activities and are known to absorb visible and infrared radiation which may lead to atmospheric warming (Zhanget al., 2015; Panicker et al., 2014; Kompalli et al, 2014; Ahmed et al.,

2014). Sulphate aerosols have both natural and anthropogenic sources. Natural sources include volcanic eruptions and sea-salt emissions (Ray and Kim, 2014) whilst biomass burning, industrial combustion and coal burning are some anthropogenic activities responsible for the emission of SO_4. Sulphates are known to cause cooling in the atmosphere by scattering incoming radiation (Sharma and Kulshrestha, 2014). Dust has also been reported to modify the atmospheric radiative budget by absorbing and scattering solar radiation. Dust can be easily transported over large distances from its source region making it a potential source for long range transport of bacteria (Ginoux et al., 2004). More recently Tesfaye et al. (2015) showed that the desert dust particles which load the western and southern regions of South Africa originate mainly from the Kalahari and Namib Desert areas.

Kumar et al. (2014) conducted a decadal climatological trend study on AOD, FMF and angstrom exponents, using Moderate Resolution Imaging Spectroradiometer (MODIS) data, over Pretoria, Bloemfontein and Cape Town (all major cities in South Africa). They showed that seasonal mean AOD values over these three locations were higher during spring (September) and summer (January / February), whereas the low values were found in the late autumn / early winter periods (June). A similar investigation is conducted in this work, however the Modern-Era Retrospective analysis for Research and Applications, Version 2 (MERRA-2) (from 2004 to 2014) is used to study black carbon (BC), sulphate (SO_4), dust and sea salt extinction AOD in SA. Based on our understanding, the study using MERRA-2 data over SA has not been previously performed. Selected sites for this study include Lephalale (23.6665° S, 27.7448° E), Bloemhof (27.6263° S, 25.5800° E), Mafikeng (25.8560° S, 25.6403° E), Potchefstroom (26.7145° S, 27.0970° E), Rustenburg (25.6544° S, 27.2559° E) and Vryburg (26.9584° S, 24.7299° E). These are all towns known to have a high rate of mining and industrial activities which would result in high aerosol loading. It should be noted that the LIDAR measurements were only carried out in Lephalale.

The main aim of this work is to study a ten year and seasonal climatology of black carbon (BC), sulphate, dust and marine aerosols in South Africa using MERRA-2.

The MERRA-2 data is validated against the AErosol RObotic NETwork (AERONET) data. The first objective of this work is to study the climatology of BC, sulphate and dust in the towns of Lephalale, Bloemhof, Mafikeng, Potchefstroom, Rustenburg and Vryburg using the Goddard Chemistry Aerosol Radiation and Transport (GOCART) model. The second objective is to study the vertical profiles of aerosol extinction coefficients in Lephalale using the Council for Scientific and Industrial Research (CSIR) mobile Light Detection and Ranging (LIDAR) and Cloud-Aerosol LIDAR and Infrared Pathfinder Satellite Observations (CALIPSO). It should be noted that LIDAR measurements were only carried out in Lephalale. The selection of this study site was motivated by the mining and industrial activities that occur in that area.

The study presented here is organized as follows: a discussion of the selected study sites is given in section 5.2 while instrumentation employed in this study is discussed in section 5.3. Section 5.4 presents a discussion of the results obtained and final conclusions are outlined in section 5.5.

5.2 Case Study locations

Limpopo and the North West provinces in South Africa (shown in Figure 1) were selected for this study because of their different geographical and climatological characteristics as well as economic activities that might contribute to aerosol loading in these regions. Lephalale is a small developing town in the Limpopo province with mining, agriculture and electricity production activities. The selection of the towns in the North-West province was motivated by a study conducted by Aurela et al (2016) in the North-West province and its surroundings. Aurela et al (2016) described the site as a dry savannah regional background site, with no major local anthropogenic sources. They showed that the surroundings contained several large anthropogenic sources from the mining and pyro-metallurgical smelting activities. In this work the aerosol effects from the surrounding sources are studied for the individual towns. Bloemhof and Mafikeng are small towns in the North West province with industrial activities whereas Potchefstroom and Vryburg have predominately farming activities. Rustenburg is characterised by a large number of facilities connected to the mining industry. It is

worth mentioning at this point that only LIDAR and CALIPSO measurements will be carried out in Lephalale and not in the other towns. However, the GOCART model data will be discussed for all the towns.

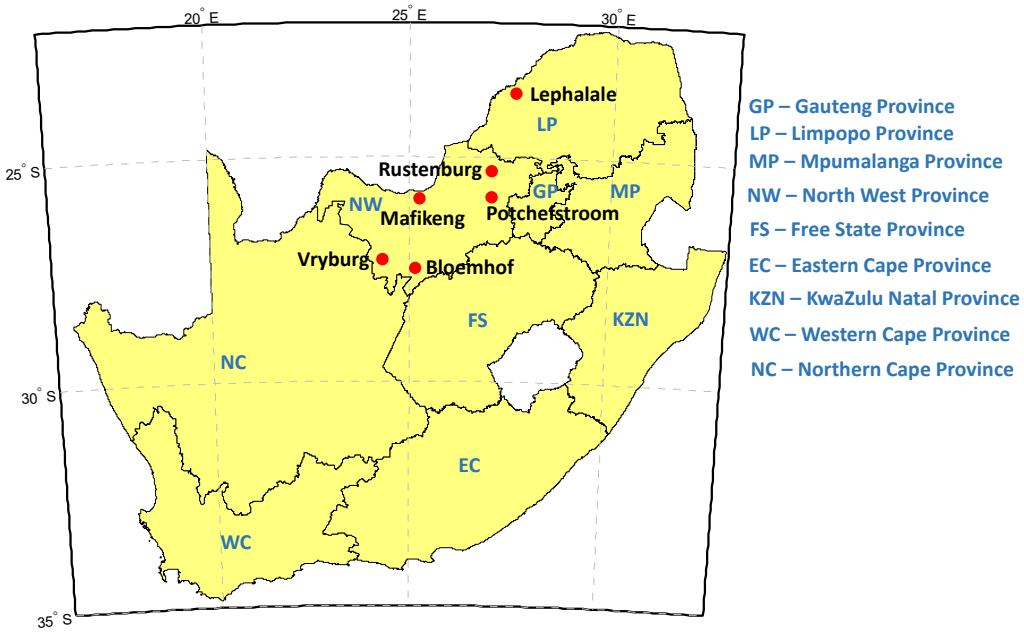

Fig. 5.1: A map of South Africa showing the nine provinces with towns where studies were conducted.

5.3 Instruments and data

5.3.1 Modern-Era Retrospective analysis for Research and Applications, Version 2 (MERRA-2)

MERRA – 2 is a NASA reanalysis product using a major new version of the Goddard Earth Observing System Data Assimilation System Version 5 (GEOS-5) (https://gmao.gsfc.nasa.gov/reanalysis/MERRA-2/). The Global Modeling and Assimilation Office (GMAO) has used its GEOS-5 atmospheric data assimilation system (ADAS) to synthesize the various observations collected over the satellite era (from 1980 to the present) into dataset that is as consistent as possible over time as it uses a fixed assimilation system. MERRA is being conducted with version 5.2.0 of the GEOS--5 ADAS with a 0.5˚ latitude × 0.625˚ longitude × 72 layers model configuration (Rienecker et al, 2011). More details on MERRA can

be found in Rienecker et al (2008 and 2011). In this work MERRA-2 is used to produce three-dimensional fields of BC, sulphate, dust and sea salt over the period of 2004-2014.

5.3.2 Goddard Chemistry Aerosol Radiation and Transport (GOCART) model

The Goddard Chemistry Aerosol Radiation and Transport (GOCART) model simulates major tropospheric aerosol components such as sulphates, dust, and BC. The GOCART model has the same horizontal resolution as the Goddard Earth Observing System Data Assimilation System (GEOS DAS): 2^{o} latitude x 2.5^{o} longitude and 20–30 vertical sigma layers, and uses the assimilated meteorological fields generated from GEOS DAS (Ginoux et al, 2001; Chin et al, 2002). A detailed description of the model is given by Chin et al (2000). In this study, the climatology of BC, sulphate and dust over the period of 2004-2007 is investigated.

5.3.3 Moderate Resolution Imaging Spectroradiometer (MODIS)

Moderate Resolution Imaging Spectroradiometer (MODIS) views a 2300 km wide swath, from polar orbit of 700 km, providing near daily coverage of Earth's surface and atmosphere (Cheng et al, 2012). MODIS measures radiance in 36 channels spanning the spectral range 0.44 to 15 μm, with a varying spatial resolution of 250 m (bands 1 and 2), 500 m (bands 3–7) and 1 km (bands 8–36). A detailed description and operation of the Terra MODIS has been described by several authors Kaskaoutis et al. (2008), El-Metwally et al. (2010) and Baddock et al. (2009). In this study, monthly mean level 3 products from MODIS Terra (MOD08M3.051) were used for the period from 2004 to 2014.

5.3.4 Multi-angle Imaging SpectroRadiometer (MISR)

The Multi-angle Imaging SpectroRadiometer (MISR) provides ongoing global coverage with high spatial resolution. MISR uses nine cameras pointed at fixed angles, one viewing the nadir direction and four each viewing the forward and aftward directions along the spacecraft ground track. Information on the technical

specifications is described by Diner et al (1998). MISR data products are grouped into three levels of processing. Level 1 processing provides calibrated instrument data. Level 2 processing provides retrieval of derived scientific quantities, such as atmospheric aerosol and cloud measurements. Level 3 processing will produce data aggregated over various time scales (monthly, seasonally, annually) on a global map grid. For this study, the monthly MISR Level - 3 data Global 0.5 x 0.5 degree aerosol product were used for the period from January 2004 to December 2014.

5.3.5 CSIR mobile LIDAR

The Mie LIDAR system at the Council for Scientific and Industrial Research (CSIR), in Pretoria (25.7461° S, 28.1881° E), was developed in 2007. This LIDAR has been configured into mono-static that maximizes the overlap of the outgoing beam with the receiver field of view. The LIDAR system has been mounted in a mobile platform with a special shock absorber frame (Sivakumar et al, 2009; Sharma et al, 2009). Sharma et al (2009) have discussed more detailed description of the CSIR-NLC mobile LIDAR system (see also chapter 3). More recent work by Shikwambana and Sivakumar (2016) address the scientific results obtained and data analysis. LIDAR measurements were carried out only during the day from 11th to 18th July 2014 in Lephalale (23.6665° S, 27.7448° E). The backscatter signals were collected and their intensities measured. Klett method was then used to calculate the aerosol backscatter coefficients and the aerosol extinction coefficient.

5.3.6 Air masses trajectories

The HYSPLIT (Hybrid Single-Particle Lagrangian Integrated Trajectory) model Version 4 is used to generate air mass backward trajectories. It is a complete system for computing simple air parcel trajectories to complex dispersion and deposition simulations (Draxler et al, 2009). The model can be run interactively on the website (http://ready.arl.noaa.gov/HYSPLIT.php).

5.3.7 Cloud-Aerosol LIDAR and Infrared Pathfinder Satellite Observations (CALIPSO)

The Cloud-Aerosol LIDAR and Infrared Pathfinder Satellite Observations (CALIPSO) provide information about the thickness of clouds and can determine the height and types of aerosols. CALIPSO consists of three co-aligned nadir-viewing instruments; the Cloud-Aerosol LIDAR with Orthogonal Polarization (CALIOP), the Imaging Infrared Radiometer (IIR), and the Wide Field Camera (WFC). CALIOP is a sensitive LIDAR that provides high-resolution vertical profiles of aerosols and clouds. CALIOP products can be separated into two levels: (a) level 1 products are composed of calibrated and geo-located profiles of the attenuated backscatter returned signal and (b) level 2 products which are derived from level 1 products and are classified in three types: layer products, profile products and vertical feature mask (Lopez et al, 2012).

A summary of the input and output data for each method used for the present study is given in Table 5.1

Table 5.1: Summary of the data used in this study.

Input data source (Temporal resolution, spatial resolution) (latitude, longitude)	**Products used**	**Period of analysis**	**Output data**
Merra-2 Model (monthly; 0.5 x 0.625^{o}) RSA (14.5^{o}, 35.4^{o}; -34.8^{o}, -22.2^{o})	BC AOD (550 nm)	2004-2014	10 year mean climatology of BC AOD
	Sulphate AOD (550 nm)		10 year mean climatology of sulphate AOD
	Dust AOD (550 nm)		10 year mean climatology of dust AOD

	Marine AOD (550 nm)		10 year mean climatology of Marine AOD
MODIS-Terra (monthly, 1°) RSA (14.5, 35.4; -34.8, -22.2)	AOD (550 nm)	2004-2014	Mean AOD climatology for South Africa
MISR (monthly, 0.5°) RSA (14.5, 35.4; -34.8, -22.2)	AOD (555 nm)	2004-2014	Mean AOD climatology for South Africa
GOCART (monthly, 2° x 2.5°) Lephalale (23.6665° S, 27.7448° E) Bloemhof (27.6263° S, 25.5800° E), Mafikeng (25.8560° S, 25.6403° E), Potchefstroom (26.7145° S, 27.0970° E) Rustenburg (25.6544° S, 27.2559° E) Vryburg (26.9584° S, 24.7299° E)	BC AOD Sulphate AOD Dust AOD	2004-2007	BC AOD trend from 2004 to 2007 Sulphate AOD trend from 2004 to 2007 Dust AOD trend from 2004 to 2007
CSIR mobile LIDAR (Daily) Lephalale (23.6665° S, 27.7448° E)	LIDAR backscatter signals returns	10-18 July 2014	Aerosol Extinction Coefficient (m^{-1}) profiles
CALIPSO (5.92 seconds, 5 km) Lephalale (23.6665° S, 27.7448° E)	Aerosol profile	12, 13, 14 and 16 July 2014	Aerosol Extinction Coefficient (m^{-1}) profiles
AERONET	Level 2.0	Aug-Dec	Averaged

Pretoria (25.7479° S, 28.2293° E)	$AOD_{500\ nm}$ (Quality Assured)	2010	monthly AOD

5.4 Results and discussion

5.4.1.1 Validation of the MERRA-2 model

AOD retrieved by the MERRA-2 model in Pretoria (25.7479° S, 28.2293° E) during the year 2010 is shown in Figure 2. The AOD retrieved by the MERRA-2 model were compared to the measured satellite AOD data from the MISR and the ground based AOD data from the AErosol RObotic NETwork (AERONET) station based at the Council for Scientific and Industrial Research (CSIR) in Pretoria. Averaged monthly AOD data from January to July was not available for AERONET but it was available from August to December 2010 as can been seen from Table 2. AOD retrieved by MERRA-2 is more comparable to AOD from AERONET than AOD measured by MISR, except for the month of October 2010. The differences in the values of AOD could be caused by the difference in wavelengths and spatial resolution amongst other things.

Table 5.2: Comparison of different techniques used to measure AOD

Month	**$AOD_{MERRA-2}$**	**AOD_{MISR}**	**$AOD_{AERONET}$**	**$AOD_{MERRA-2}$ -AOD_{MISR} (%)**	**$AOD_{MERRA-2}$ - $AOD_{AERONET}$ (%)**
Aug	0.1716	0.1863	0.1744	-0.0147 (8.57 %)	-0.0028 (1.63%)
Sep	0.2618	0.2339	0.2705	0.0279 (10.66%)	-0.0087 (3.32%)
Oct	0.3538	0.3766	0.2726	-0.0228 (6.44%)	0.0812 (22.95%)
Nov	0.1672	0.1959	0.1481	-0.0287 (17.17%)	0.0191 (11.42%)

5.4.1.2 Spatial distributions of AOD using MODIS and MISR

The averaged $AOD_{550\ nm}$ and $AOD_{555\ nm}$ in SA for the period 2004 to 2014 using MODIS and MISR is shown in Fig. 5.2a and 5.2b respectively. The averaged AOD retrieved from the database of both instruments shows a high aerosol loading in the northern and eastern parts of the country namely Limpopo and Mpumalanga Provinces. The east coast of SA also exhibits high aerosol loading. A low aerosol loading is observed in the southern parts of SA as measured by both instruments. MODIS AOD in the northern parts of SA is observed at ~0.11 whereas MISR AOD for the northern parts is observed at ~0.16. The MODIS results agree with earlier research, namely Kumar et al (2014). However, it is observed that MISR gives slightly higher AOD compared to MODIS. This is also observed in the lower southern parts of SA where MODIS AOD is ~0.02 and MISR AOD is ~0.08. Discrepancies in AOD between satellite platforms are generally within uncertainty and the differences in AOD values might be due to calibration and retrieval algorithms, processing methods, complex surface (Guo et al, 2014) and pass over time of the satellites over SA (Hersey et al, 2015). Other factors that might contribute to these differences include the difference in spatial resolutions and swath dimension of these instruments.

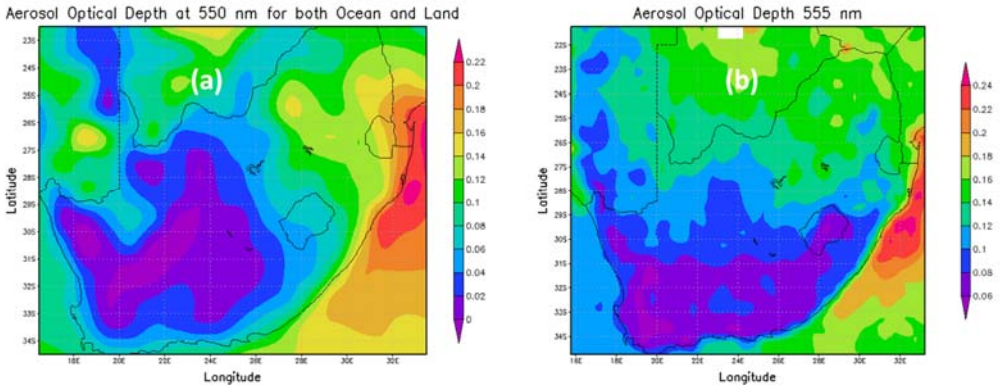

Fig 5.2: Latitude-Longitude color map of monthly mean AOD for South Africa using (a) MODIS (550 nm) and (b) MSIR (555 nm).

5.4.1 BC, Sulphate, Dust and Sea salt AOD observed by MERRA - 2

The spatial distribution of anthropogenic aerosols for SA averaged from 2004 to 2014 and retrieved by MERRA – 2 are shown in Fig. 5.3. BC aerosols are dominant in the north eastern parts of SA (see Fig 5.3a). This dominance can also be observed on the borders of the neighbouring countries i.e. Botswana, Zimbabwe and Mozambique and corresponds to a BC AOD of ~0.014. The biggest contributor to BC aerosols is from biomass burning. It has been shown that source-regions countries such as Zambia are the major contributor of BC through biomass burning in comparison to SA (Cahoon et al 1992). Air masses from the north and north eastern parts of the subcontinent transport a substantial amount of products resulting from biomass burning into the country (Cahoon et al 1992). By comparison low aerosol loading (AOD ~ 0.005) of BC is observed in the south western parts of SA and this extends to the Atlantic Ocean. However, the mid-latitude of SA is dominated by moderate BC (AOD ~ 0.008).

Sulphate aerosols are mostly concentrated in the eastern parts of SA in Mpumalanga province (see Fig 5.3b) where high aerosol loading (AOD ~ 0.1) is observed. Swaziland also shows a high sulphate aerosol loading (AOD ~ 0.085). Some of the northern and south eastern parts of SA have moderate sulphate loading corresponding to AOD ~ 0.07. The high and moderate sulphate aerosols are from the industrial activities in the Highveld and pyrometallurgical processing of copper in the Democratic Republic of Congo and Zambian Copper belt as reported by Piketh et al (1999 Freiman and Piketh, 2003; Zunckel et al., 2000). SAFARI-92 and SAFARI-2000 further indicated that biomass burning emissions that most significantly impact South Africa originate in neighbouring countries such as Zimbabwe and Mozambique (Hersey et al, 2015) Coal combustion for power production might also be a major contributor to the high sulphate aerosol loading in the Mpumalanga region. A low sulphate aerosol loading (AOD ~ 0.03) is observed from the central interior to the south western part of SA. This finding is supported by Tesfaye et al (2014) using the Regional Climate Model (RegCM4). The major contributions to sulphate aerosols are from industrial activities and biomass burning. However, in the western parts of SA these

activities are low and the major contribution of sulphate aerosols could be from the Atlantic Ocean region. It is also known that sulphate aerosols can be produced within the atmosphere by oxidation of reduced sulfur species such as dimethyl sulfide (DMS) emitted by oceanic phytoplankton (Alexander et al, 2005). Since the western parts of SA have low industrial activities and biomass burning, the major contribution of the sulphate could arise from emitted DMS. However, deliquescent sea-salt and dust aerosols have also been reported to be possible sites for aqueous phase sulphate production (Alexander et al, 2005).

Dust aerosols are more dominant in the north western parts of SA (see Fig 5.3c) where a high dust aerosol loading (AOD ~ 0.013) is observed near the border of Namibia. This dust aerosol loading is produced in the Kalahari and Namib Desert areas (Tesfaye et al, 2015). Low dust aerosol loading (AOD ~ 0.006) is observed in the northern, eastern and south eastern parts of SA. The interior of the country shows a moderate dust aerosol loading (AOD ~ 0.009).

Sea salt aerosols (SSA) are mainly produced by air bubbles bursting at the surface of the ocean as a result of wind stress (Jaegle et al, 2011). As the bubbles come back to the surface form whitecaps and burst, leading to the injection of seawater film and jet drops into the atmosphere (Jaegle et al, 2011). SSA is most dominant in the coastal parts of SA (see Fig. 5.3d). A high aerosol loading (AOD ~ 0.065) of SSA is observed in the south eastern coast in close proximity to the Indian Ocean. This high SSA loading could result from higher water temperatures in the Indian Ocean compared to that of the Atlantic Ocean. This is supported by Grythe et al (2014) who reported that temperature influences the production of SSA, i.e., production of SSA is favoured by warmer water temperatures relative to colder ones. It implies the reason for observed moderate SSA loading (AOD ~ 0.045) over south coast and south western coast. Low SSA loading (AOD ~ 0.01) is observed in the interior of SA as would be expected.

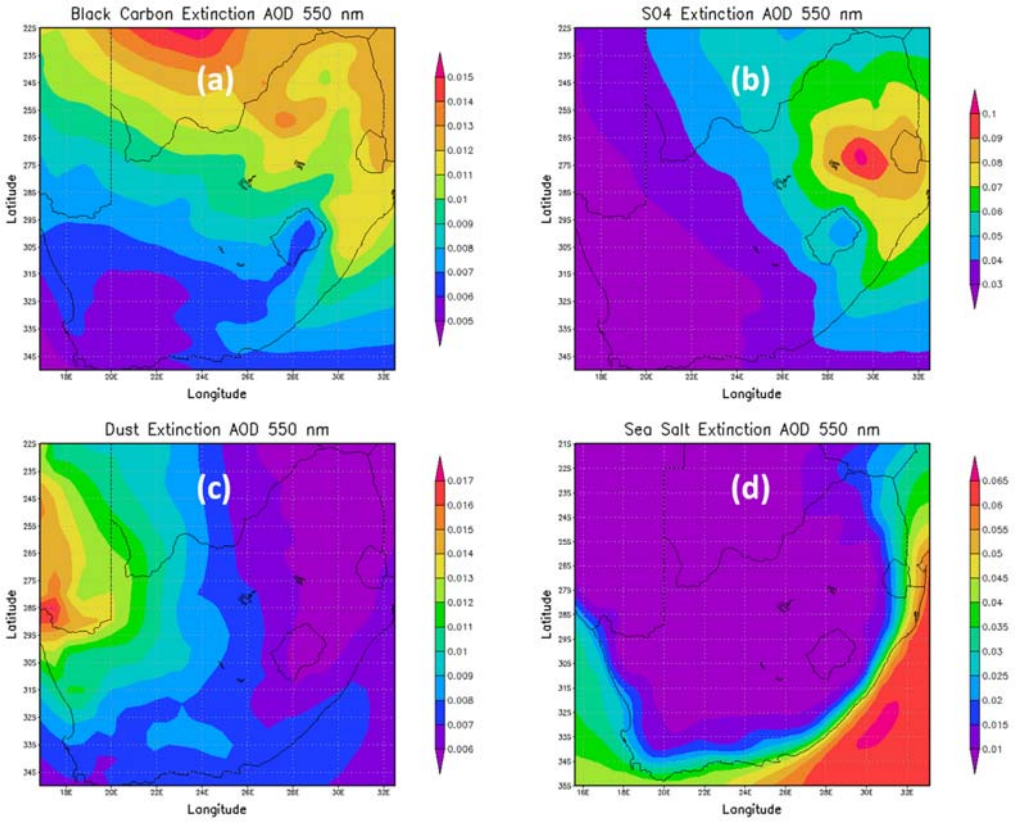

Fig. 5.3: Spatial distributions of (a) black carbon AOD (550 nm), (b) sulphate AOD (550 nm), (c) dust AOD (550 nm) and sea salt (550 nm) as derived from MERRA – 2 for the period of 10 years (2004 to 2014).

5.4.2 Seasonal BC, Sulphate, Dust and Sea salt AOD observed by MERRA – 2

5.4.2.1 Seasonal BC AOD

Seasonal spatial distribution of BC aerosols in SA averaged for the period 2004 to 2014 and retrieved by MERRA – 2 are shown in Figure 5.4(a-d). Spring season has the maximum BC AOD in a year followed by the winter season. The summer and autumn seasons are of lower and lowest BC AOD in the year. During summer (December, January, February) high aerosols loading (AOD ~ 0.008) were observed in the northern and south eastern parts of the country (see Figure 5.4a) while moderate BC aerosols (AOD ~ 0.0045) are observed in the interior and southern parts of SA. Low BC aerosols (AOD ~ 0.003) are observed in the south western parts of the country.

During autumn (March – May) high aerosol levels in the northern regions of SA close to the Botswana border are observed. There south eastern part of SA as well as Swaziland showed a high aerosol loading compared to the rest of the country. The interior part of the country showed moderate aerosol loading (AOD ~ 0.0045) and low aerosol loading was observed in the western parts of South Africa. Autumn shows the lowest aerosol loading compared to the other seasons. Kruger et al (2016) showed that autumn and winter months have less strong wind gusts in the north eastern and north western regions and this could be the reason why less BC is observed during these seasons. During winter, June – August (JJA), an increase in aerosol loading is observed throughout the country (see Fig. 5.4c). However, the south western parts of SA still showed the lowest aerosol loading (AOD ~ 0.0045) compared to the rest of the country.

The highest BC aerosols loading in the country is observed in spring, September – November (SON) and corresponds to AOD ~ 0.02 (see Fig. 5.4d). Tesfaye et al (2014) also reported a high value of AOD in spring and showed that during this season the eastern part of Limpopo is one of the major local sources of biomass burning aerosols. These biomass burning aerosols are transported by wind to some parts of the North West province (Tesfaye et al 2014).

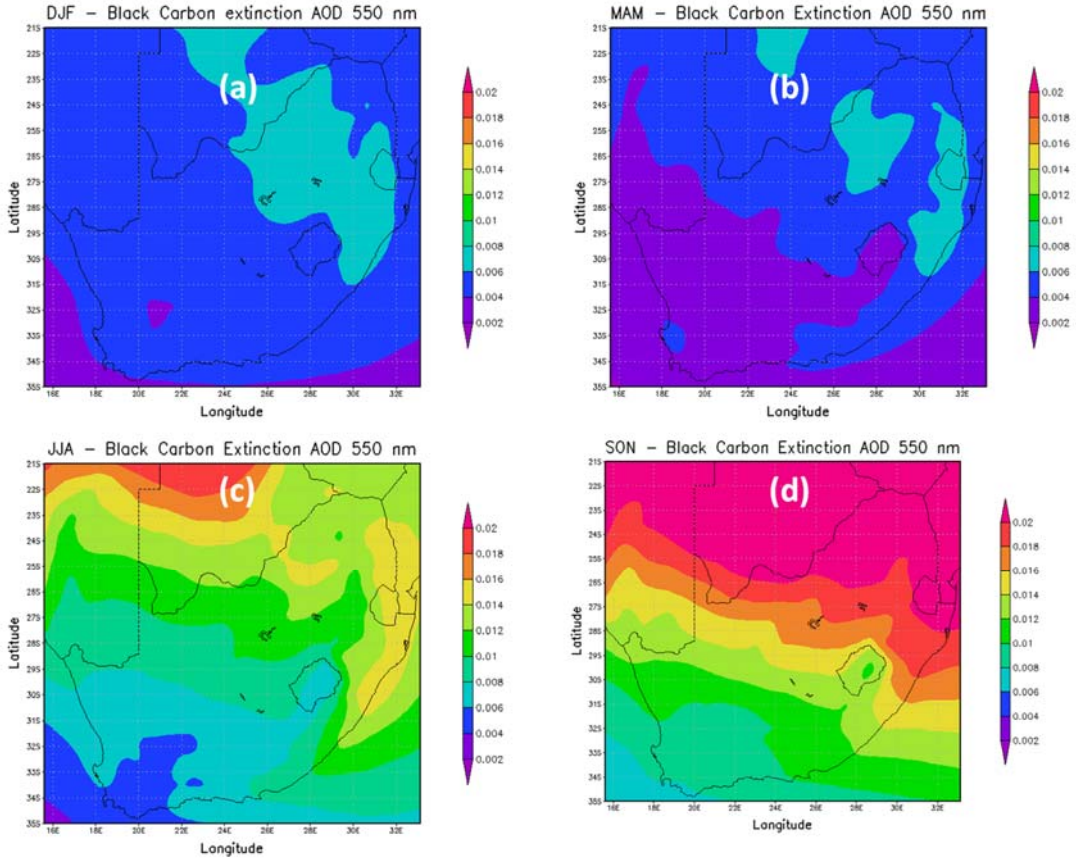

Fig. 5.4: Seasonal variation of black carbon AOD (550 nm) (a) summer, (b) autumn (c) winter and (d) spring derived from MERRA – 2 data.

5.4.2.2 Seasonal sulphate AOD

Seasonal spatial distribution of sulphate aerosols for SA averaged from 2004 to 2014 and retrieved by MERRA – 2 are shown in Fig. 5.5 (a-d). For the four seasons, high aerosol loading is always observed in the eastern part of the country namely Mpumalanga and Gauteng provinces. Low aerosol loading is always observed in the interior and western parts of the country. Of the four seasons, Summer (DJF) shows the highest sulphate aerosol loading overall (AOD ~ 0.16) in the eastern parts of SA (see Fig. 5.5a). Aurela et al (2016) also reported on the dominance of sulphate aerosols in summer. Since sulphate aerosols emanate mostly from the anthropogenic sources, Aurela et al (2016) attributed the high sulphate loading to air masses that passed over the coal-fired power station in Waterberg (23.6686° S, 27.6117° E) or the PMG smelter, in the Northam and

Thabazimbi area (24.5828° S, 27.4028° E), may enhance the sulphate concentration by 14 or 37 times.

During winter, the AOD shows a lowest aerosol loading (AOD ~ 0.05) in the eastern parts of SA (see. Fig 5.5c). The western parts of SA have a wet winter whereas eastern and interior parts of SA have a dry winter. Tesfaye et al (2011) showed that there is a decrease in wind speed and Angstrom exponent in SA over the winter season. They further showed that the lower AOD during winter in the eastern and interior parts of SA is due to a low wind speed which causes less aerosol generation and dispersion. This is one of the reasons why lower sulphate aerosols are observed. Overall, factors such as meteorological conditions, prevailing winds, temperature changes, less precipitation and different oxidation rates experienced during summer and winter have an impact in the variation of sulphate concentration seasonally. Autumn and spring (see Figures 5b and 5d), on the other hand, show moderate sulphate aerosol loading of (AOD ~ 0.1 and AOD ~0.11) in the eastern parts of SA respectively.

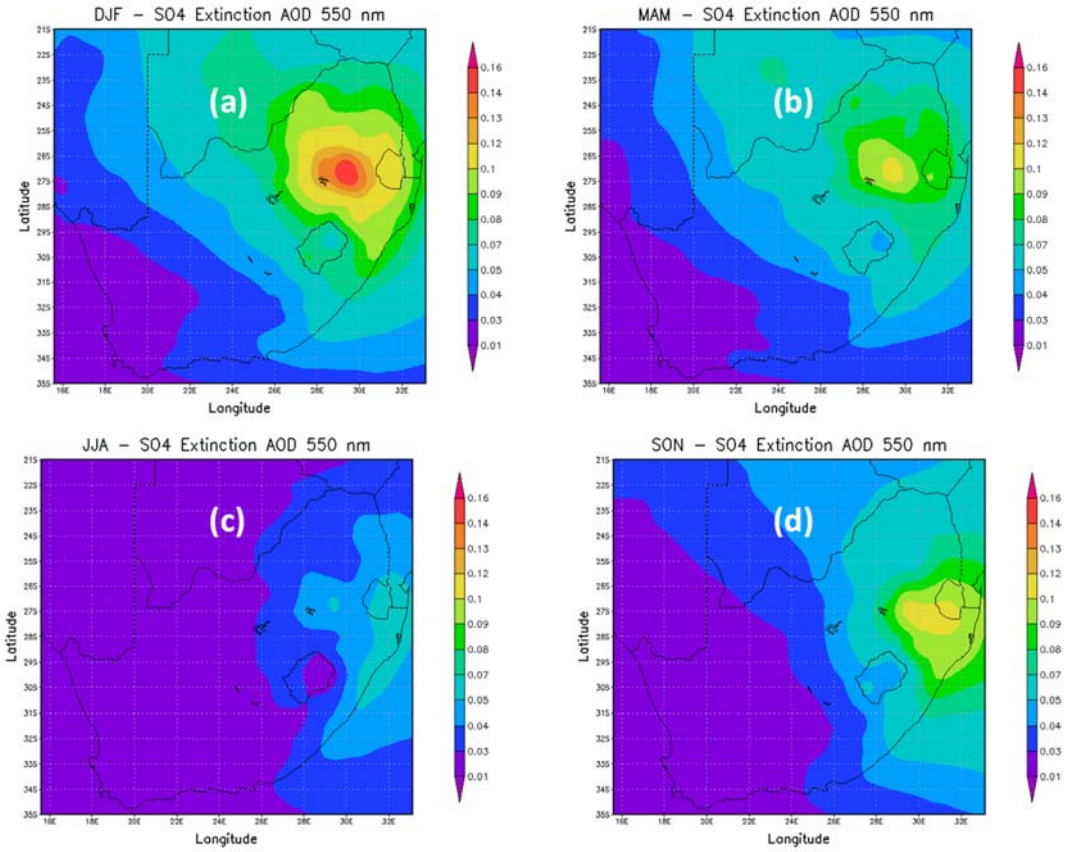

Fig. 5.5: Same as figure-4 but for sulphate AOD (550 nm)

5.4.2.3 Seasonal dust AOD

Seasonal spatial distribution of dust aerosols in SA averaged from 2004 to 2014 and retrieved by MERRA – 2 are shown in Fig. 5.6(a-d). In all seasons, dust aerosols are predominantly observed in the north western parts of SA while low aerosol loading can be observed in the eastern parts of SA. Summer (DJF) is the season with the highest dust aerosol loading (AOD ~ 0.01) with maximum concentrations observed in the north western parts of the country (see Fig. 5.6a) corresponding to the Northern Cape Province. The dust aerosols appear to originate from Namibia which borders South Africa, a finding supported by Tesfaye et al (2015). Their study showed that the Kalahari and Namib Deserts were the main source for the detection of desert dust particles in the western parts of South Africa. During summer, moderate aerosol loading (AOD ~ 0.006) was observed in the central interior and south of the country. During Autumn (MAM)

and Winter (JJA) mostly SA has low dust aerosol levels (AOD ~ 0.006) except the north western regions where it has moderate dust aerosol levels (see Fig. 5.6b and 5.6c respectively). Change in wind direction with change in season might be the cause for the observed low aerosol loading. In Spring (SON) (see Fig. 5.6d) an increase in dust aerosol loading is seen. Namibia is the major source of dust aerosols and these aerosols are transported to SA in the north western parts to the interior of the country. In their study, Hersey et al (2015) observed high dust aerosols using the GOCART model. They attributed this to be from windblown dust from the nearby Namib Desert.

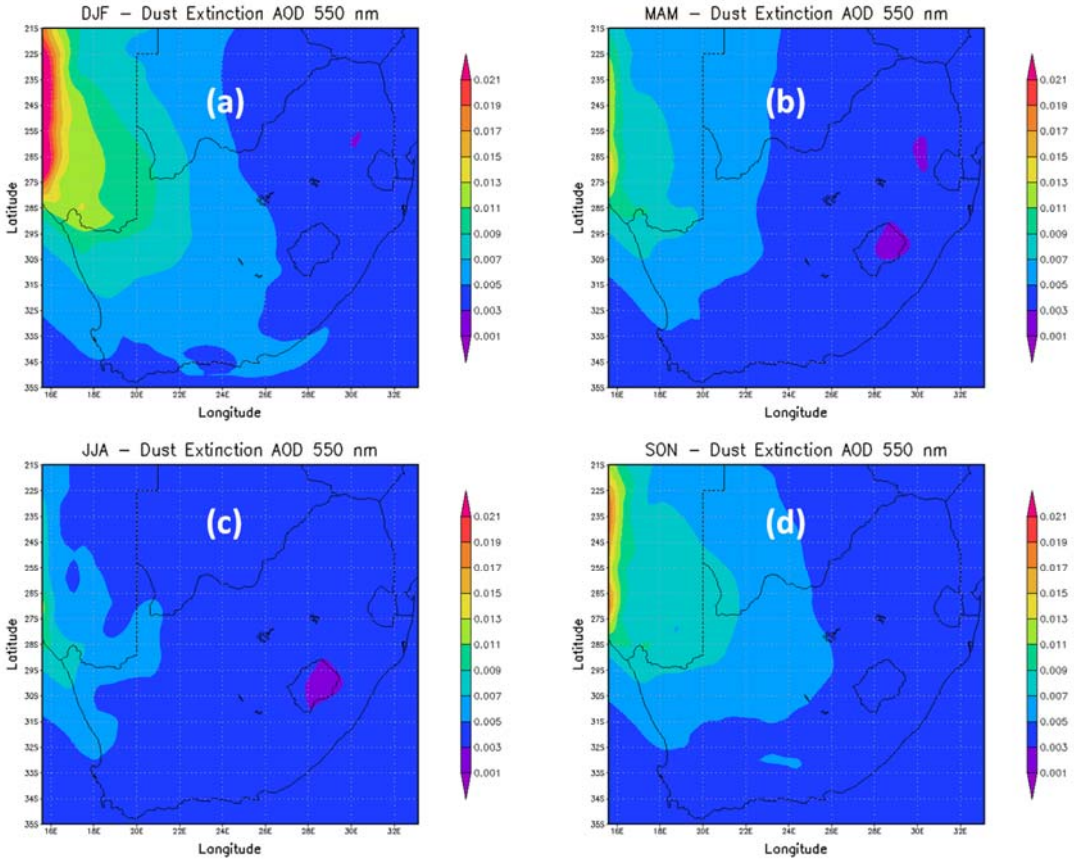

Fig. 5.6: Same as figure 4 but for Dust AOD (550 nm).

5.4.2.4 Seasonal sea salt AOD

Seasonal spatial distribution of SSA in SA averaged from 2004 to 2014 and retrieved by MERRA – 2 are shown in Fig. 5.7(a-d). High SSA loading (AOD ~ 0.065) are observed in coastal areas in all seasons. The Indian Ocean has a higher sea salt aerosol loading than the Atlantic Ocean in all seasons. The highest sea salt aerosol loading in the Indian Ocean is observed in Summer (DJF) and Spring (SON) (see Fig. 5.7a and 5.7d). These seasons coincide with warmer water temperatures compared to Autumn (MAM) and Winter (JJA), such conditions favour the production of SSA. During Summer (DJF) and Spring (SON) (see Fig. 5.7a and 5.7d) moderate SSA (AOD ~ 0.01) are observed in the south western and northern parts of SA. Low SSA loading (AOD ~ 0.003) is observed in the interior of SA. For Autumn (MAM) and Winter (JJA) low SSA loading is observed in the interior (see Fig. 5.7b and 5.7c). By comparison, the north eastern parts of the country show moderate SSA loading (AOD ~ 0.025).

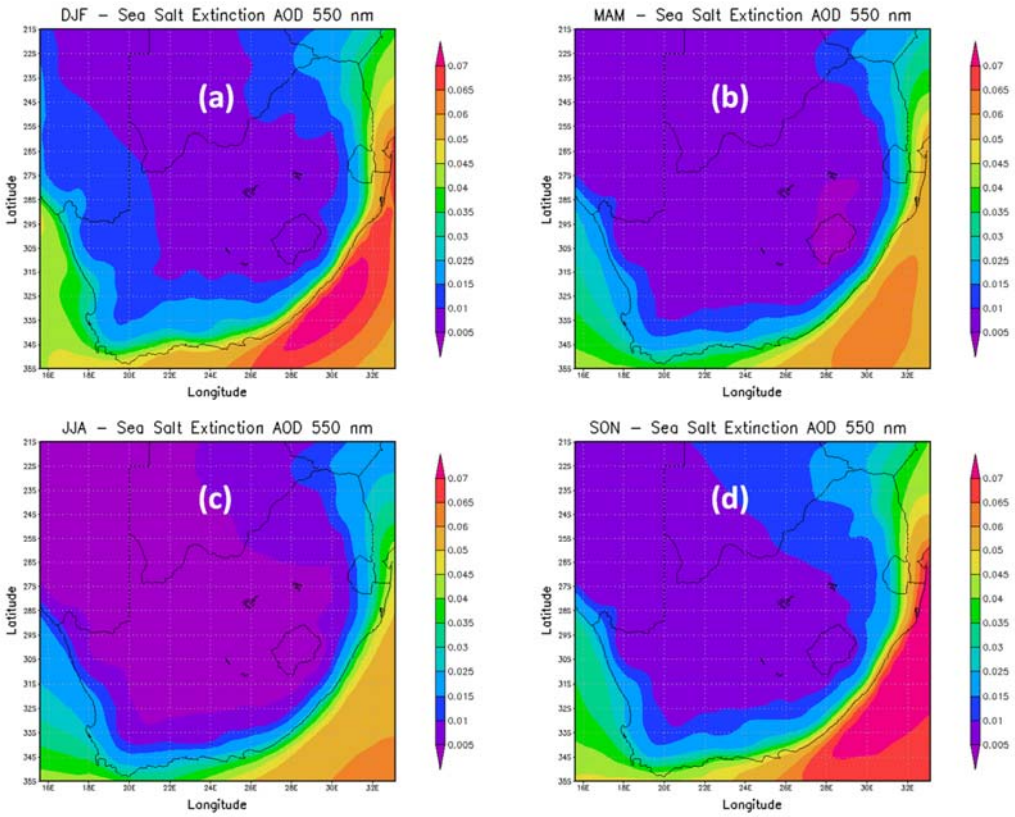

Fig. 5.7: Same as figure 4 but for Sea Salt AOD.

5.4.3 GOCART natural and anthropogenic aerosols

This investigation uses the GOCART model V006 product for the period 1 January 2000 - 31 December 2007. There is no data after December 2007. The reason for using data from 2004 to 2007 is that this period falls within the period of the ten year (2004 – 2014) trend studies carried out using MERRA – 2 data. Figure 5.8 illustrates GOCART model results from 2004 to 2007 for the regional AOD trends from natural sources (dust - indicated by green colour in Fig. 5.8) and anthropogenic sources (BC and sulphates – indicated by blue and red colour respectively in Fig. 5.8) for the locations of Lephalale, Bloemhof, Mafikeng, Potchefstroom, Rustenburg and Vryburg. In each of these towns, it is observed that sulphates are the dominant contributing factor towards total anthropogenic AOD when compared with contributions due to dust and BC. In all locations, sulphate AOD levels show a very similar pattern of variation during the period from 2004 to 2007. However the trend for 2004 – 2007 in all locations shows marked seasonal changes in Sulphate AOD with highest values observed in February (summer) and lowest values observed in June (winter). The photochemical oxidation of SO_2 to sulphate in the summer could be the reason for the high calculated AOD values (Meij et al., 2012). Atmospheric rate of oxidation of SO_2 increases with increasing relative humidity (Khoder, 2002) and since the relative humidity is high in summer for SA (Tesfaye et al, 2011) this favours the production of sulphate aerosols. Consideration of BC (see Fig. 5.8 – black coloured) shows that in all locations and the variations are found to be similar for the period from July 2004 to December 2007. In all towns, August typically shows the highest AOD corresponding to ~0.02. It is estimated due to biomass burning which begins in the late winter and early spring seasons.

A high dust AOD was also observed in August of every year in all the towns except for Stellenbosch where it shows high AOD in June, August and May. The results are found to be in consistence with earlier findings by Tesfaye et al (2015). Some of the attributions of the dust particles are from the Namib and Kalahari Deserts.

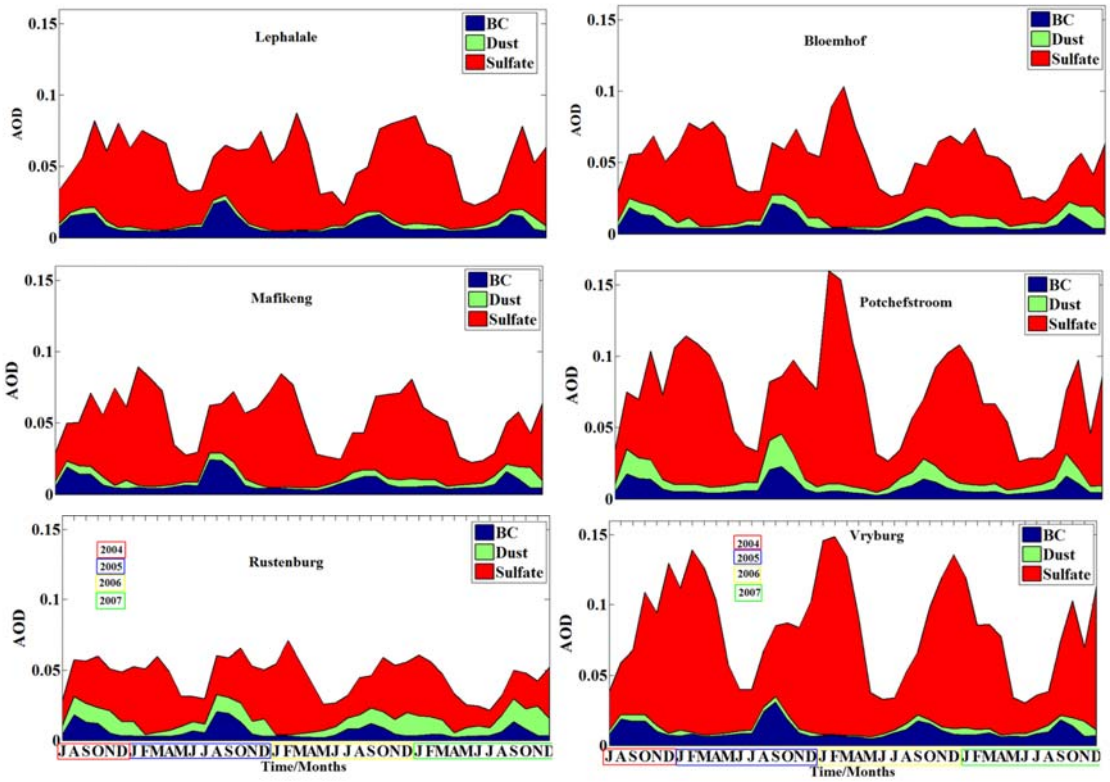

Fig. 5.8: Estimated AOD trends for BC, dust and sulphate aerosols in each region using the GOCART model from July 2004 to December 2007.

5.4.4 Case study in Lephalale

5.4.4.1 CSIR mobile LIDAR

As mentioned earlier, Lephalale is a growing town with mining, coal electricity power plant and industrial activities. BC and Sulphate aerosols observed by MERRA- 2 during the Winter (JJA) season showed moderate BC and sulphate aerosol loading in this location. These results served as motivation to carry out temporal resolution studies using the CSIR mobile LIDAR at this town. Measurements were carried out from 10-17 July 2014 at a location 3 km from construction of the new power station and 2 km from an active power station. The temporal evolution of the backscattered LIDAR signal for the eight days of measurements is shown in Fig. 5.9. Planetary Boundary Layer structures were

observed at various heights ranging from 2 – 3 km for the different days. High aerosol loading was observed in the morning but the level of aerosol loading has been decreased with time. The high aerosol load in the morning hours could be caused by the operating power station burning more coal to meet electricity demand. As the day gets warmer the demand for electricity reduces and less coal is burnt.

The vertical distributions of aerosol extinction coefficient profiles are shown in Fig. 5.10. These profiles were recorded ~10:00 am local time except for the day 10 July 2014 when it was recorded at 11:15 am. Similar profiles were observed on 10, 13 and 16 July 2014, however, the level at which highest value of the extinction coefficient occurs is different in the lower parts of the troposphere. The highest values of aerosol extinction coefficients were observed at an altitude of about ~20 m. The extinction values are 0.244 km^{-1}, 0.586 km^{-1} and 0.178 km^{-1} respectively for the above said three days. Three layers of aerosol clouds were observed between the altitude of 0.8 km and 1.4 km on 11 July 2014. The peaks of each aerosol cloud layers were observed at altitudes of 0.86 km, 1.24 km and 1.36 km, with aerosols extinction coefficient values of each peak at 0.000781 km^{-1}, 0.00604 km^{-1} and 0.00886 km^{-1} respectively. On 12 July 2014 a sharp peak at a height of 1.14 km corresponding to an aerosol layer was observed with an extinction coefficient of 0.0182 km^{-1}. A similar profile was observed on 14 and 15 July 2014 with multiple peaks observed corresponding to layers of aerosol. These aerosol layers were observed on the lower part of the troposphere at ~1 km. A different type of profile was observed on 17 July 2014. Although the height profile show a decrease in aerosol loading with increasing altitude, aerosol layers were observed at altitudes as low as 0.3 km. Multiple layers were also observed at altitudes less than 1 km. The results suggest that there was an over loading of aerosols in the lower part of the atmosphere during this period. From Figure 5.10, it can be seen that all profiles showed the existence of aerosols in the lower part of the atmosphere, however, aerosol levels decrease with an increasing altitude.

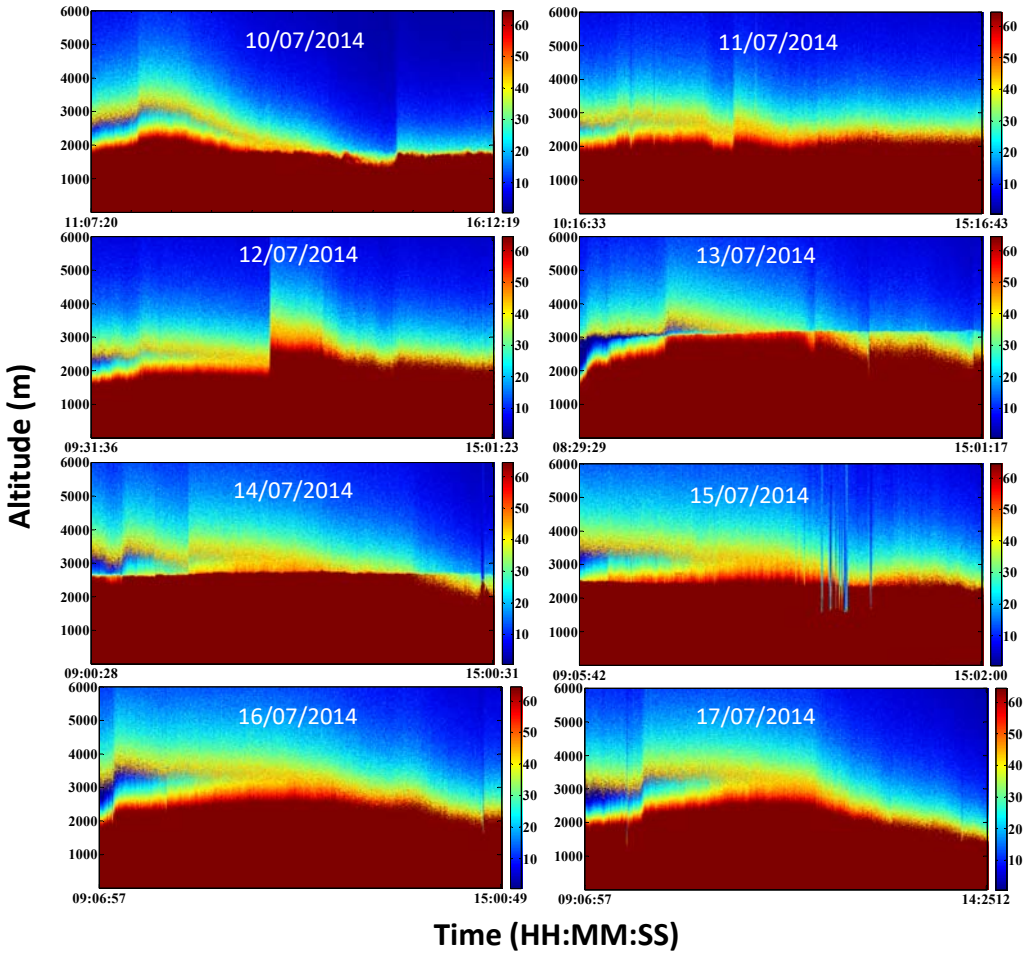

Fig. 5.9: Temporal evolution of the CSIR mobile LIDAR backscatter signal returns recorded during July 2014 at Lephalale.

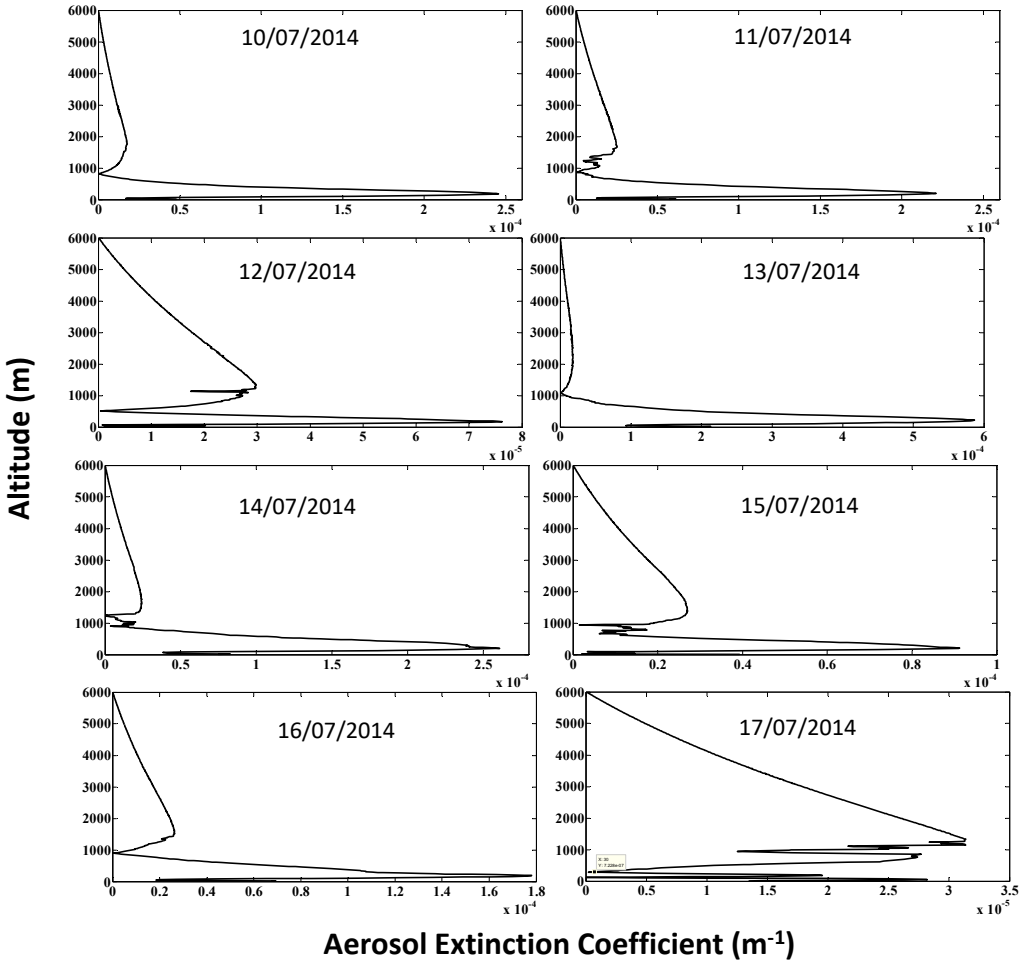

Fig. 5.10: Vertical profiles of aerosol extinction derived from CSIR mobile LIDAR signal returns recorded during July 2014 at Lephalale.

5.4.4.2 HYSPLIT model

120 hours of backward trajectories of air masses arriving at Lephalale for 11, 13, 15 and 17 July 2014 were obtained from the HYSPLIT model at two different altitudes to understand the long-range transport of air masses (see Fig. 5.11). On 11 July 2014 the backward trajectory at heights of 500 m (red) and 3000 m (blue) were used to observe the origins of the air mass (see Fig. 5.11a). The air mass showed that the 500 m air masses were from a northerly direction travelling through the Atlantic Ocean and inland of South Africa from the west to the east

coast. The air masses also travelled through southern Mozambique until it has reached the study site. However, at 3000 m, the air masses travelled from a southerly direction over the deserts of Namibia and Botswana before reaching Lephalale. It is likely that the air masses transported dust from the Namib and Kalahari Desert. On 13 July 2014, (see Fig. 5.11b) the air masses at 500 m originated from Swaziland and travelled through south Mozambique, south Zimbabwe as well as south Botswana. These locations have an arid climate and are likely to have significant amounts of dust that could be carried away by the air masses. At 3000 m, the air masses travelled the same route as that on 11 July 2014. On 15 July 2014 (see Fig. 5.11c) at 500 m, the air masses originated from the Indian Ocean and travelled north on the east coast of South Africa before reaching Lephalale. However, at 3000 m, the air masses originated from the Atlantic Ocean and travelled through the northern parts of South Africa. These parts of the country are known to have an arid climate and it is possible that sizeable amounts of dust could be transported to the study location. On 17 July 2014 at 500 m (see Fig. 5.11d), air masses travelled the same route as on 15 July 2014. However, air masses at 3000 m have originated from the south of Brazil, across the Atlantic Ocean and the east coast of South Africa before reaching Lephalale. This suggests that the major types of aerosols that could have been transported were of the marine type. However, air masses also travelled through the north eastern parts of South Africa which are dry and dust-rich. As a result, other types of aerosols such as dust could also have been transported to the study location.

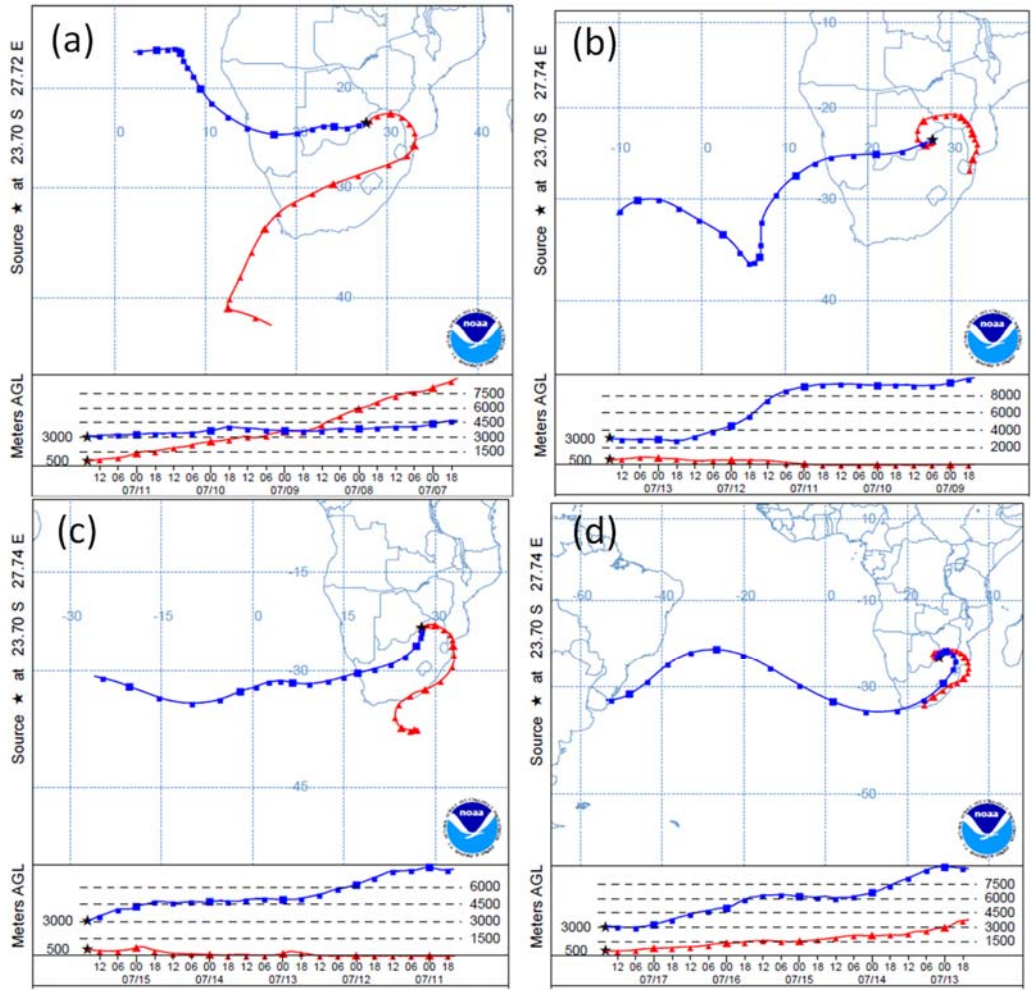

Fig. 5.11: NOAA HYSPLIT model of backward trajectory air masses for 5 days ending at Lephalale on (a) 11 July 2014; (b) 13 July 2014; (c) 15 July 2014 and (d) 17 July 2014.

5.4.4.3 Observation from CALIPSO

The mean extinction coefficient profiles from the CALIPSO Level 2 aerosol profile product are shown in Fig. 5.12. Only available CALIPSO data close to or less than ~150 km from the measuring site was considered as shown in Fig. 5.12. Inspection of Fig. 5.12 shows that aerosols could only be detected up to an altitude of 6 km and there is a general decrease in aerosol levels with an increase in altitude. Different profile shapes are observed for the four different days under

investigation. On 12 July 2014, the highest extinction coefficient value of 0.18 km^{-1} is observed at an altitude of ~3 km. The variations in extinction further reveals the presence of two broad peaks which indicate a high aerosol content observed at altitudes of ~ 3 and 5 km respectively. On 13 and 14 July 2014, the extinction coefficients show a similar profile to that recorded on 12 July. However, the biggest differences were in the values of the extinction coefficients recorded. On 13 July 2014 the highest extinction coefficient was 0.34 km^{-1} observed at an altitude of ~ 300 m. By comparison, on 14 July 2014 the highest extinction coefficient was 0.07 km^{-1} observed at an altitude of ~ 600 m. On 16 July 2014 the highest extinction coefficient value was 0.29 km^{-1} observed at an altitude of ~ 300 m. The range of extinction coefficient values observed by CALIPSO for the four days is 0.01 to 0.34 km^{-1}, this indicates that the aerosols observed might be dust. Dust aerosols with the extinction coefficients in the range from 0.01 to 0.38 km^{-1} were observed by He and Yi (2014) in their studies over Wuhan (30.5∘N, 114.4∘E), China.

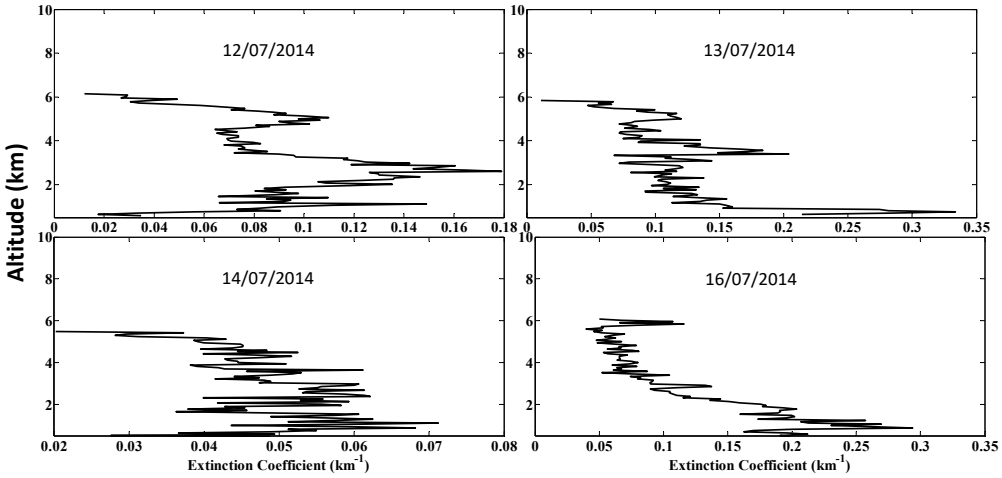

Fig. 5.12: Extinction coefficient profiles from CALIPSO recorded on (a) 12 July 2014, (b) 13 July 2014, (c) 14 July 2014 and (d) 16 July 2014 at Lephalale.

On 16 July 2014, the overpass of the CALIPSO satellite at Lephalale was at 11:59:29 to 12:12:58. It is almost the same time that the CSIR mobile LIDAR was in operation. This is the only day where there is simultaneous measurement

between the two instruments. The CALIPSO's total attenuated backscatter at 532 nm is presented in Fig. 5.13(a) for the case study of 16 July 2014. Low levels of aerosols were observed during this period as was the case with the CSIR LIDAR around these time frames. The high aerosol load in the morning could be caused by the operating power station burning more coal to meet the electricity demand. The backscatter coefficients are low (1×10^{-4}) at altitudes greater than 1 km. This indicates a low level of aerosol loading. However, a planetary boundary layer was observed at an altitude of ~1 km. High backscatter coefficients (1×10^{-1}) were observed which indicates a high aerosol loading. The vertical mask feature profile (see. Fig. 5.13b), confirms that the backscatter signals are indeed from aerosols. The aerosol subtype profiles are shown in Fig. 5.13c, classifies these aerosols as a combination of polluted dust and smoke.

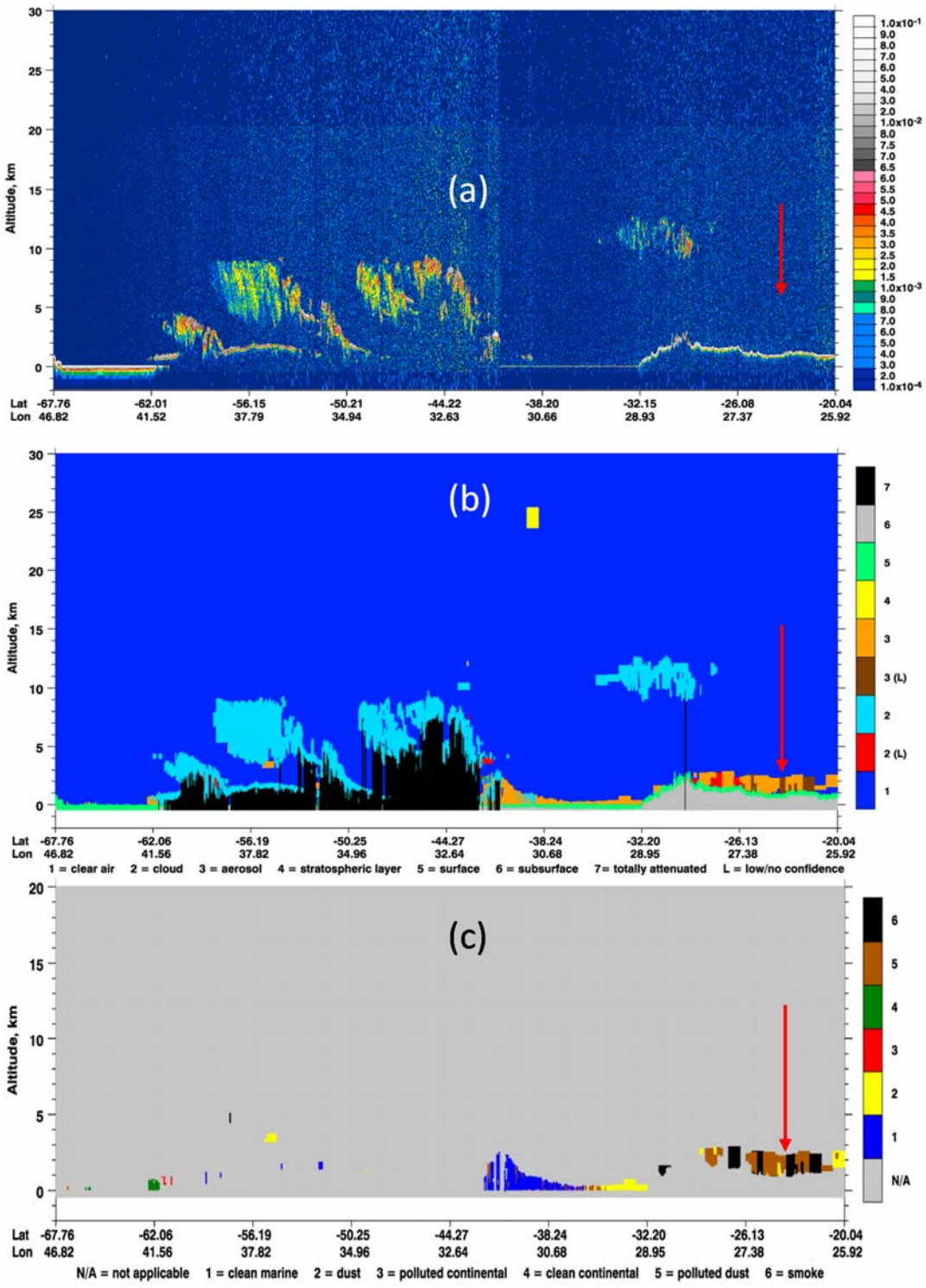

Fig. 5.13: CALIPSO (a) 532 nm attenuated backscatter , (b) aerosol types and (c) vertical feature mask on 16 July 2014 at UTC 11:59:29 to 12:12:58 at Lephalale.

5.4.4.4 Comparison of CSIR LIDAR and CALIPSO extinction coefficients

The range of the aerosol extinction coefficient values observed for the four days by (1) CALIPSO was from 0.01 km^{-1} to 0.34 km^{-1} and (2) CSIR mobile LIDAR was 0.07 km^{-1} to 058 km^{-1} (see Table 5.3). There are several reasons for the differences in the aerosol extinction coefficient values which include: (a) the horizontal distances between CALIPSO and the CSIR mobile LIDAR site was as much as 150 km, (b) the retrieval algorithm differ and (c) the CSIR mobile LIDAR averages the data over a long period in a day whereas CALIPSO averages over a short period. Dust aerosols with the extinction coefficients in the range 0.01 km^{-1} to 0.38 km^{-1} were observed by He and Yi (2014) in their studies over Wuhan (30.5°N, 114.4°E), China. Relating their study to what was observed by in this work by the CSIR mobile LIDAR, dust aerosols were only observed in 14 and 16 July 2014 with extinction coefficients of 0.26 km^{-1} and 0.17 km^{-1} respectively.

Table 5.3: Comparison of aerosol extinction coefficients using the CSIR mobile LIDAR and CALIPSO.

Date (July 2014)	**CSIR mobile LIDAR** **Aerosol Extinction Coefficient (km^{-1})**	**CALIPSO** **Aerosol Extinction Coefficient (km^{-1})**
12	0.07	0.18
13	0.58	0.34
14	0.26	0.07
16	0.17	0.29

5.5 Conclusion

Climatological studies of BC, sulphate, dust and sea salt aerosols using MERRA – 2 reanalysis data were carried out over South Africa. BC aerosols were observed to be dominant in the north eastern parts of the country while sulphate aerosols were observed to be dominant in eastern parts of the country. Dust aerosols were observed to be dominant in the north western parts of the country. Sea salt aerosols were observed to be dominant along the coastal regions of the country, however, moderate sea salt aerosols were also observed in the north eastern parts of the country. Seasonal studies conducted revealed that BC aerosols are more dominant in the eastern parts of SA during spring and less dominant in autumn. However, sulphate aerosols are more dominant in the eastern parts of SA during summer and less dominant in winter. This is consistent with what was observed by Kumar et al (2014) where they observed higher mean AOD during spring and summer. Dust aerosols are more dominant in the north-western parts of SA during summer and less dominant in winter. This result agrees well with the findings from Tesfaye et al. (2015). Sea salt aerosols are more dominant in the coast area, Indian Ocean and north eastern parts of SA during summer and spring, and less dominant during autumn and winter.

The GOCART model was used from the period July 2004 to June 2007 to simulate aerosol optical depth for sulphate, dust and BC tropospheric aerosols in six towns (Lephalale, Potchefstroom, Bloemhof, Mafikeng, Rustenburg and Vryburg) in South Africa. The model showed that sulphates contributed significantly in all the towns with BC also having some contribution. The GOCART model also indicated that there was no significant change in the sulfate aerosols during the period from 2004 to 2007. The highest sulphate aerosols levels were observed in the summer while the lowest sulphate aerosol levels were observed in winter. The high sulphate concentration in summer is as a result of an increase in relative humidity which favours the production of sulphates. The trends in BC aerosols revealed no change from 2004 to 2007. The highest BC aerosol levels were observed in August with the town of Lephalale showing the

highest AOD. A high dust aerosol level was also observed during every August and over all the locations.

Aerosol extinction coefficient profiles were retrieved by the CSIR mobile LIDAR during the Lephalale campaign and were compared to aerosol extinction coefficients profiles retrieved by CALIPSO. The aerosols extinction coefficients between the CSIR LIDAR and CALIPSO were not in good agreement with each other due to numerous reasons which include difference in retrieval algorithm, and horizontal distance between CSIR LIDAR and CALIPSO was about 150 km. However, aerosol extinction coefficient of 0.26 km^{-1} and 0.17 km^{-1} on 14 and 16 July 2014 respectively could be identified as dust aerosols.

References

Adak A, Chatterjee A., Singh A. K., Sarkar C., Ghosh S., Raha S., 2014. Atmospheric Fine Mode Particulates at Eastern Himalaya, India: Role of Meteorology, Long-Range Transport and Local Anthropogenic Sources. *Aerosol and Air Quality Research*, 14, 440–450.

Alexander B, Park RJ, Jacob DJ, Li QB, Yantosca RM, Savarino J, Lee CCW, Thiemens MH. 2005. Sulfate formation in sea-salt aerosols: Constraints from oxygen isotopes, *Journal of Geophysical Research*, 110, D10307.

Aurela M, Beukes JP, Van Zyl P, Vakkari V, Teinilä K, Saarikoski S, Laakso L, 2016. The composition of ambient and fresh biomass burning aerosols at a savannah site, South Africa. *South African Journal of* Science,112, 8 pages.

Ahmed T, Dutkiewicz V. A., Khan A. J., Husain L., 2014. Long term trends in Black Carbon Concentrations in the North eastern United States. *Atmospheric Research*, 137, 49–57.

Baddock M. C., Bullard J. E., Bryant R. G., 2009. Dust source identification using MODIS: A comparison of techniques applied to the Lake Eyre Basin, Australia. *Remote Sensing of Environment*, 113, 1511–1528.

Cahoon, D. R., Jr., B. J. Stocks., Levine J. S., Cofer III W. R., O'Neill K. P., 1992. Seasonal distribution of African savanna fires, *Nature*, 359, 812–815

Cheng T, Chen H., .Gu X., ,Yu T.,.Guo J., Guo H., 2012. The inter-comparison of MODIS, MISR and GOCART aerosol products against AERONET data over China. *Journal of Quantitative Spectroscopy & Radiative Transfer*, 113, 2135–2145.

Chin M., Rood R. B., Lin S. J, Muller J. F., Thompson A. M., 2000. Atmospheric sulfur cycle simulated in the global modelGOCART': Model description and global properties. *Journal of geophysical research*, 105, 671-24,687.

Chin M., Ginoux P., Kinne S., Torres O, Holben B. N., Duncan B. N.,. Martin R. V., Logan J. A., Higurashi A., Nakajima T., 2001. Tropospheric Aerosol Optical Thickness from the GOCART Model and Comparisons with Satellite and Sun Photometer Measurements. *Journal of the atmospheric sciences*, 59, 461-483.

De Meij A., Pozzer A., Lelieveld J., 2012. Trend analysis in aerosol optical depths and pollutant emission estimates between 2000 and 2009.*Atmospheric Environment*, 51, 75-85

Diner D. J., Beckert J. C., Reilly T. H., Bruegge C. J., Conel J. E., Kahn R. A., Martonchik J. V., Ackerman P. T., Davies R., Gerstl S. A. W., Gordon H. R., Muller J. P., Myneni R. B., Sellers P. J., Pinty B., Verstraete M. M., 1998, Multi-angle Imaging SpectroRadiometer (MISR) Instrument Description and Experiment Overview, *IEEE Transactions on Geoscience and remote sensing*, 36, 1072-1087

El-Metwally M., Alfaro S.C., Abdel Wahab M. M., Zakey A. S., Chatenet B., 2010. Seasonal and inter-annual variability of the aerosol content in Cairo (Egypt) as deduced from the comparison of MODIS aerosol retrievals with direct AERONET measurements. *Atmospheric Research*, 97, 14–25.

Freiman MT, Piketh SJ, 2003. Air transport into and out of the industrial Highveld region of South Africa. *Journal of Applied Meteorology*, 42, 994–1002.

Ge J. M., Su J., Fu Q., Ackerman T. P., Huang J. P., 2011. Dust aerosol forward scattering effects on ground-based aerosol optical depth retrievals. *Journal of Quantitative Spectroscopy & Radiative Transfer*, 112, 310–319.

Ginoux P, Chin M. Tegen I, Prospero J. M., Holben B.,Dubovik O., Line S-L., 2001. Sources and distributions of dust aerosols simulated with the GOCART model. *Journal of geophysical research*, 106, 255-20,273.

Ginoux P., Prospero J. M, Torres O, Chin M., 2004. Long-term simulation of global dust distribution with the GOCART model: correlation with North Atlantic Oscillation. *Environmental Modelling & Software*, 19, 113–128.

Gong C, Xin J, Wang S., Wang Y, Wang P, Wang L., Li P.,2014. The aerosol direct radiative forcing over the Beijing metropolitan area from 2004 to 2011.*Journal of Aerosol Science*, 69, 62–70.

Grythe H., Ström J., Krejci R., Quinn P., Stohl A., 2014. A review of sea-spray aerosol source functions using a large global set of sea salt aerosol concentration measurements, *Atmospheric Chemistry and Physics*, 14, 1277–1297.

Guo J, Gu X, Yu T, Cheng T, Chen H, 2014. Trend analysis of the aerosol optical depth from fusion of MISR and MODIS retrievals over China. IOP Conference Series: Earth and Environmental Science, 17.

He Y., Yin F., 2014. Dust Aerosols Detected Using a Ground-Based Polarization Lidar and CALIPSO over Wuhan (30.5°N, 114.4°E), China. *Advances in Meteorology*, 2015..

Hersey, S. P., Garland, R. M., Crosbie, E., Shingler, T., Sorooshian, A., Piketh, S., Burger, R. 2015. An overview of regional and local characteristics of aerosols in South Africa using satellite, ground, and modeling data. *Atmospheric Chemistry and Physics (Print)*, 15, 4259–4278.

Jones T. A., Christopher S. A., 2011. A reanalysis of MODIS fine mode fraction over ocean using OMI and daily GOCART simulations. *Atmosphere Chemistry and. Physics*, 11, 5805–5817.

Kaskaoutis D. G., Kambezidisa H. D., Adamopoulos A. D.,.Kassomenos P. A., 2006. Comparison between experimental data and modeling estimates of aerosol optical depth over Athens, Greece. *Journal of Atmospheric and Solar-Terrestrial Physics*, 68, 1167–1178.

Kaskaoutis D. G, Kambezidis H. D., Nastos P. T.,.Kosmopoulos P. G., 2008. Study on an intense dust storm over Greece. *Atmospheric Environment*, 42, 6884–6896.

Khoder MI. 2002. Atmospheric conversion of sulfur dioxide to particulate sulfate and nitrogen dioxide to particulate nitrate and gaseous nitric acid in an urban area. Chemosphere, 49, 675–684

Kompalli S. K, Babu S. S., Moorthy K. K., Manoj M. R., Kumar N.V.P , Shae K. H. B, Joshi A. K, 2014. Aerosol black carbon characteristics over Central India: Temporal variation and its dependence on mixed layer height. *Atmospheric Research*, 147–148, 27–37.

Kruger A.C., Pillay D. L., van Staden M., 2016. Indicative hazard profile for strong winds in South Africa, *South African Journal of Science*,112, 1-11, http://dx.doi.org/10.17159/

Kumar K. R., Sivakumar V, Yin Y, Reddy R, Kang N, Diao Y, A. Adesina A. J., Yu X., 2014. Long-term (2003 - 2013) climatological trends and variations in aerosol optical parameters retrieved from MODIS over three stations in South Africa. *Atmospheric Environment*, 95, 400 – 408.

Jaegle L., Quinn P. K., Bates T. S., Alexander B., Lin J.-T., 2011. Global distribution of sea salt aerosols: new constraints from in situ and remote sensing observations. *Atmospheric Chemistry and Physics*, 11, 3137–3157

Lopes F. G. S., Mariano G. L., Landulfo E. and E.V.C. Mariano, 2012: Impacts of Biomass Burning in the Atmosphere of the South eastern Region of Brazil Using Remote Sensing Systems, *Atmospheric Aerosols - Regional Characteristics* - Chemistry and Physics, Dr. Hayder Abdul-Razzak (Ed.), ISBN: 978-953-51-0728-6, InTech, DOI: 10.5772/50406Lyamani H., Olomo F. G., Foyo I., Alados-Arboledas L., 2011. Black carbon aerosols over an urban area in south-eastern Spain: Changes detected after the 2008 economic crisis. *Atmospheric Environment*, 45, 6423–6432

Menon H. B., Shirodkar S., Kedia S., Ramachandran S., Babu S, Moorthy K. K., 2014. Temporal variation of aerosol optical depth and associated shortwave radiative forcing over a coastal site along the west coast of India. *Science of the Total Environment*, 468–469, 83–92.

Panicker A. S., Pandithurai G., Safai P. D., Dipu S., Prabha T. V., Konwar M., 2014. Observations of black carbon induced semi direct effect over Northeast India. *Atmospheric Environment*, 98, 685-692.

Piketh, S.J., Annegarn H. J., Tyson P. D., 1999. Lower tropospheric aerosol loadings over South Africa: the relative contribution of aeolian dust, industrial emissions and biomass burning. *Journal of .Geophysical Research*, 104, 1597-1607.

Ray S., Kim K-H., 2014. The pollution status of sulfur dioxide in major urban areas of Korea between 1989 and 2010. *Atmospheric Research*, 147–148, 101–110.

Rienecker M. M., Suarez M.J., Todling R., Bacmeister J., Takacs L., Liu H-C., Gu W., Sienkiewicz M., Koster R. D., Gelaro R., Stajner I., and Nielsen J. E., 2008. Technical Report Series on Global Modeling and Data Assimilation. *NASA/TM–2008–104606*, 27, p92.

Rienecker M. M., Suarez M.J., Gelaro R, Todling R., Bacmeister J., Liu E., Bosilovich M., Schubert S., Takacs L., Kim G-K., Bloom S., Chen J., Collins D., Conaty A., Da silva A., Joiner J., Koster R. D., Lucchesi R., Molod A., Owens T., Pawson S., Pegion P., Redder C., Reichle Rolf., Robertson F., Ruddick A. G., Sienkiewicz M., Woollen J., 2011. MERRA: NASA's Modern-Era Retrospective Analysis for Research and Applications. *Journal of Climate*, 24, 3624 - 3648

Shahgedanova M., Lamakin M., 2005. Trends in aerosol optical depth in the Russian Arctic and their links with synoptic climatology. *Science of the Total Environment*, 341, 133 – 148.

Sharma D., Kulshrestha U. C., 2014. Spatial and temporal patterns of air pollutants in rural and urban areas of India. *Environmental Pollution*, 195, 276-281.

Sharma A., Sivakumar V., Bollig C, van der Westhuizen C. and Moema D ,2009. System description of the mobile LIDAR of the CSIR, South Africa. *South African Journal of Science*, 105**,** 456-462.

Sivakumar V, Tesfaye M., Alemu W., Moema D., Sharma A., Bollig C. and Mengistu G. 2009, CSIR South Africa mobile LIDAR—First scientific results: comparison with satellite, sun photometer and model simulations. *South African Journal of Science*, 105, 449-455

Shikwambana L., Sivakumar V., 2016. Observation of Clouds Using the CSIR Transportable LIDAR: A Case Study over Durban, South Africa. *Advances in Meteorology*, 2016, pp 9, doi:10.1155/2016/4184512

Tesfaye M, Sivakumar V, Botai J, Tsidu GM. 2011. Aerosol climatology over South Africa based on 10 years of Multiangle Imaging Spectroradiometer (MISR) data. *Journal of .Geophysical Research*, 116, D20216.

Tesfaye M., Tsidu G. M., Botai J., Sivakumar V., de W Rautenbach C. J., 2015. Mineral dust aerosol distributions, its direct and semi-direct effects over South Africa based on regional climate model simulation. *Journal of Arid Environments*, 114, 22-40.

Tesfaye M., Botai J. Sivakumar V., Tsidu G. M., 2014. Simulation of biomass burning aerosols mass distributions and their direct and semi-direct effects over South Africa using a regional climate model. *Meteorology and Atmospheric Physics*, 125, 177–195.

Xu H., Ceamanos X, Roujean J-L, Carrer D, Xue Y., 2014. Can satellite-derived aerosol optical depth quantify the surface aerosol radiative forcing? *Atmospheric Research*, 150, 151–167.

Zhang X, Rao R, Huang Y, Mao M, .Berg M. J., Sun W., 2015. Black carbon aerosols in urban central China. *Journal of Quantitative Spectroscopy & Radiative Transfer*, 150, 3–11.

Zunckel M., L. Robertson, Tyson PD, Rodhe H. 2000. Modelled transport and deposition of sulphur over southern Africa. *Atmospheric Environment*, 34, 2797–2808.

Chapter 6

Long-range transport of volcanic aerosols over South Africa: A case study of the Calbuco volcano eruption in April 2015

6.1 Introduction

Volcanic eruptions are very rare in Africa compared to other continents such as South America and Europe. However, the consequences of volcanic eruptions in these locations may result in volcanic aerosols being transported across Africa. One of the main components of gases from these eruptions is large amounts of atmospheric sulphur dioxide (SO_2) which increases the optical thickness at stratospheric altitudes (Shin et al, 2015). The long range transport of SO_2 from volcanic eruptions has been reported by several authors such as Schmidt et al (2015), Miffre et al (2012), Pitari et al (2016) and Sawamura et al (2012). Furthermore, sulphur dioxide is also known to have a cooling effect by reflecting sunlight back into space (Andersson et al, 2015; Langmann, 2014; Pöschl, 2005). Finally, SO_2 is known to be toxic when present in high concentrations at the surface and has negative impacts on human health (Ialongo et al, 2015).

Volcanic aerosols reside in the lower stratosphere and this has an impact on the hydrological cycle, stratospheric ozone and cirrus clouds (Kuebbeler et al, 2012).When SO_2 is injected into the stratosphere from a volcanic eruption it is converted into sulfuric acid aerosols. These aerosols form layers over a period of a week to several months after the eruption. Some effects of these SO_2 layers include: (a) they reflect in the visible part of the solar spectrum, (b) they absorb terrestrial and solar infrared radiation, and (c) they provide surfaces for a large number of chemical reactions to occur that alter the chemical composition of the stratosphere (Muthers et al, 2015; Robock, 2000).

In studies of the most recent volcanic eruptions, several authors have used different instruments to measure and track volcanic aerosols. DeVries et al (2014) conducted a study of SO_2 from the Nabro volcano eruption (starting 12 June 2011) in Eritrea (13.37ºN, 41.7º E) using satellite based spectrometers: SCanning Imaging Absorption spectroMeter for Atmospheric CHartographY (SCIAMACHY), Global Ozone Monitoring Experiment (GOME-2), and Ozone Monitoring Instrument (OMI). Bitar et al (2010) reported on the measurement of volcanic aerosols from the eruption of Kasatochi volcano, in the central Aleutian Islands of Alaska (52.1752° N, 175.5139° W) on 7–8 August 2008. These measurements were carried out using a LiDAR (Light Detection and Ranging) system in Halifax, Nova Scotia (44.64°N, 63.59°W). Observations started one week after the eruption and continued for the next 4 months. The study revealed stratospheric aerosols initially began as thin structured plumes near an altitude of 18 km and gradually dispersed over the 4 month observation period. Tropospheric aerosols were only observed in the second week after the eruption. Vernier et al (2011) conducted a study on the variability of stratospheric aerosol loading between 1985 and 2010 using satellite-based instruments to study the impact of the 1991 volcanic eruption of Mount Pinatubo. In their study data from the Stratospheric Aerosol and Gas Experiment (SAGE-II) measurements, Optical Spectrograph and InfraRed Imaging System (OSIRIS), the Global Ozone Monitoring by Occultation of Stars (GOMOS) on ENVISAT and the Cloud-Aerosol Lidar and Infrared Pathfinder Satellite Observations (CALIPSO) were used. They reported that stratospheric aerosol levels increased by as much as two orders of magnitude and only reached “background levels” between 1998 and 2002. From 2002 onwards other researchers reported on a sustained increase in the level of SO_2. Romeo et al (2016) reported on the volcanic eruption that occurred on 22–23 April 2015 in Calbuco Volcano, Chile. The main explosive eruption consisted of two eruption pulses on 22 and 23 April 2015. The first pulse started on April 22 at 21.05 GMT with a column ~15 km high above the crater and the other eruption pulse occurred on 23 April at 04.09 GMT with a column higher than 15 km in height. The main focus was to study the tephra fall deposits

of both pulses in terms of stratigraphy, distribution, volume, emplacement dynamics and eruption source parameters.

In the work presented here, the transport of volcanic aerosols over South Africa from the Calbuco Volcano eruption that occurred on 22 and 23 April 2015 is investigated. The Hybrid Single Particle Lagrangian Integrated Trajectory (HYSPLIT) model is used to compute air parcel trajectories and dispersion of the volcanic aerosols, Moderate Resolution Imaging Spectroradiometer (MODIS) is used to measure the aerosol optical depth (AOD) before and after the eruption (both in Chile and South Africa), OMI is used to measure SO_2 aerosols and CALIPSO is used to measure the extinction coefficient profiles and identify the type of aerosols detected.

The study presented here is organized as follows: a discussion of the selected study sites is given in section 2 while instrumentation employed in this study is discussed in section 3. Section 4 presents a discussion of the results obtained and final conclusions are outlined in section 5.

6.2 Study sites

The Calbuco volcano (41.33°S, 72.61°W) is situated in southern Chile (see Fig. 6.1a) and is one of the most active volcanoes in Chile. The last major eruption occurred on 22–23April 2015, followed by a smaller eruption on 30 April 2015. South Africa (see Fig. 6.1b) has no history of volcanic eruptions or places and SO_2 aerosols produced within the country are mostly the result of by-products from mining, industrial activities, vehicle emissions and biomass burning. However, most of the SO_2 is trapped in the lower troposphere. These SO_2 aerosols are mainly produced in the Highveld region of South Africa.

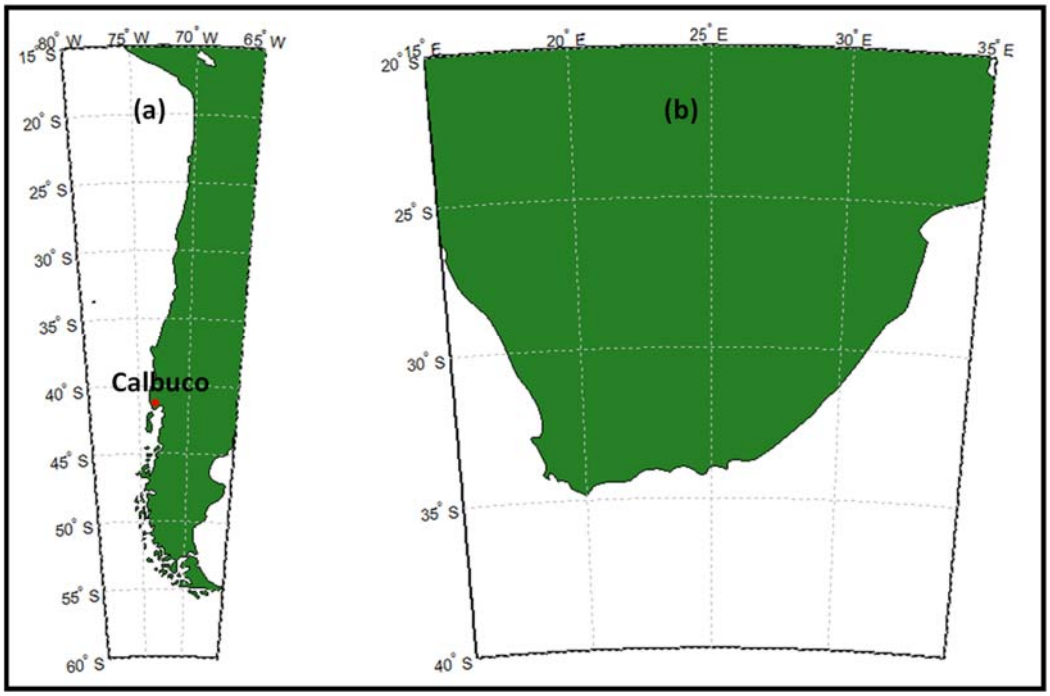

Fig. 6.1: Map of (a) Chile showing location of Calbuco volcano and (b) South Africa.

6.3. Instruments

6.3.1 Hybrid Single Particle Lagrangian Integrated Trajectory (HYSPLIT) model

The National Oceanic and Atmospheric Administration (NOAA) Air Resources Laboratory's (ARL) HYSPLIT model is a complete system for computing simple air parcel trajectories as well as complex transport, dispersion, chemical transformation, and deposition simulations (Stein et al, 2015). The model calculation method is a hybrid between the Lagrangian approach, using a moving frame of reference for the advection and diffusion calculations as the trajectories or air parcels move from their initial location, and the Eulerian methodology, which uses a fixed three-dimensional grid as a frame of reference to compute pollutant air concentrations. For further information on the historical background and recent developments on this model refer to Stein et al (2015).

In this study, 120-hour forward-trajectories in the altitude range from 1000 to 12000 m were calculated for the period 22 April to 28 April 2015, using the web based version of the HYSPLIT model.

6.3.2 MODIS (Moderate Resolution Imaging Spectroradiometer)

The MODIS (Moderate Resolution Imaging Spectroradiometer) instrument is operational on both the Terra and Aqua spacecrafts. MODIS observes a swath approximately 2330 km wide, and makes between 14 and 15 orbits per day. For ease of processing and data storage, MODIS data are organized into 5 min swath segments called granules (288 per day), which are composed of 1354 by 2030 pixels at nominal 1 km resolution (near nadir) (Levy et al, 2013; Ruiz-Arias et al, 2013). Its detectors measure 36 spectral bands between 0.405 μm and 14.385 μm, and it acquires data at three spatial resolutions; 250 m, 500 m, and 1000 m.

The MODIS aerosol product monitors the ambient aerosol optical depth (AOD) over the oceans globally and over a portion of the continents. Daily Level 2 data are produced at the spatial resolution of a 10x10 1-km (at nadir)-pixel array. There are two MODIS Aerosol data product files: MOD04_L2, containing data collected from the Terra platform; and MOD04_L2, containing data collected from the Aqua platform (https://modis-atmos.gsfc.nasa.gov/MOD04_L2/). MODIS uses quality flags to characterize the accuracy of AOD retrievals (Ruiz-Arias et al, 2013; Safarpour et al, 2014). The quality flags range from 3 (high confidence) to 0 (low or no confidence). The quality flags are assigned to each MODIS AOD retrieval based on the quality and number of pixels used in the AOD algorithms (Safarpour et al, 2014). In this work the change in AOD before and after the volcanic eruption is measured for both Chile and SA.

6.3.3 OMI (Ozone Monitoring Instrument)

The Ozone Monitoring Instrument (OMI) is the result of a partnership between NASA and the Dutch and Finnish meteorological institutes and space agencies. OMI flies onboard the NASA EOS-Aura satellite (Krotkov et al, 2016) and can distinguish between aerosol types (such as smoke, dust, and sulphates) and

measure cloud top pressure and coverage, which provide data from which tropospheric ozone levels may be derived.

A new product of PBL (Planetary boundary layer) SO_2 product was released in 2014, in which SO_2 is retrieved using a new algorithm that employs principal component analysis (PCA) techniques applied to OMI radiances (Krotkov et al, 2016; Li et al, 2016). The PCA algorithm uses a clear-sky air mass factor (AMF) similar to the previous SO_2 product, but with the full spectral content between 310.5 and 340 nm. This reduces retrieval noise by a factor of 2 (Krotkov et al, 2016; Li et al, 2016).

For this work the OMI/Aura Level-3e SO_2 Data Product OMSO2e (Version 003) was downloaded from the web-based application developed by the Goddard Earth Sciences Data and Information Services Center (GES DISC), Giovanni (Geospatial Interactive Online Visualization ANdaNalysis) (https://giovanni.sci.gsfc.nasa.gov /giovanni/).

6.3.4 CALIPSO (Cloud-Aerosol Lidar and Infrared Pathfinder Satellite Observation)

CALIPSO (Cloud-Aerosol Lidar and Infrared Pathfinder Satellite Observation) combines an active LiDAR instrument with passive infrared and visible imagers to probe the vertical structure and properties of thin clouds and aerosols over the globe (https://www-calipso.larc.nasa.gov/). CALIPSO is the first satellite-borne LiDAR optimized specifically for aerosol and cloud measurements, and is also the first polarization LiDAR in space (Liu et al, 2009). It is a dual-wavelength, polarization-sensitive elastic backscatter LiDAR and its light source is an Nd:YAG pulsed laser operating at 1064 nm and 532 nm (Liu et al, 2009). The active laser technique provides high vertical resolution and allows retrieval of aerosol profiles above lower-lying clouds and below optically thin clouds, as well as in cloud-free conditions (Kittaka et al, 2011). The transmitted laser beam is linearly polarized, and two polarization-sensitive 532-nm receiver channels measure the degree of linear depolarization of the return signal (Liu et al, 2009). A detailed description of CALIPSO is given by Winker et al (2010) and Winker et al (2013). However, Vaughan et al (2004) gives a full description of the

CALIPSO data products. In this work we use the CALIPSO level 2, version 3.30 data products (CAL_LID_L2_05kmAPro-Prov-V3-30). The CALIPSO images are acquired from NASA CALIPSO Lidar Browse Images website (http://www-calipso.larc.nasa.gov/products/lidar/browse_images/production/).

6.4. Results and discussion

6.4.1 Initial observations

The climatology of SO_2 aerosols over South Africa for the month of April for the years 2013, 2014, 2015 and 2016 are shown in Fig. 6.2. SO_2 aerosols are observed to be prominent in the eastern parts of South Africa and less so for the rest of the country (see Fig. 6.2a, b and d). The distribution of these SO_2 aerosols suggests that they are produced in the eastern parts of the country and travel to other locations. However, in April 2015 (see Fig. 6.2c) anomalously high levels of SO_2 were observed in the western and interior parts of SA as well as over the southern parts of Namibia, northern parts of Lesotho and the north eastern parts of SA. This increase in SO_2 distribution suggests that an event could have taken place which lead to this unusual accumulation of observed SO_2.

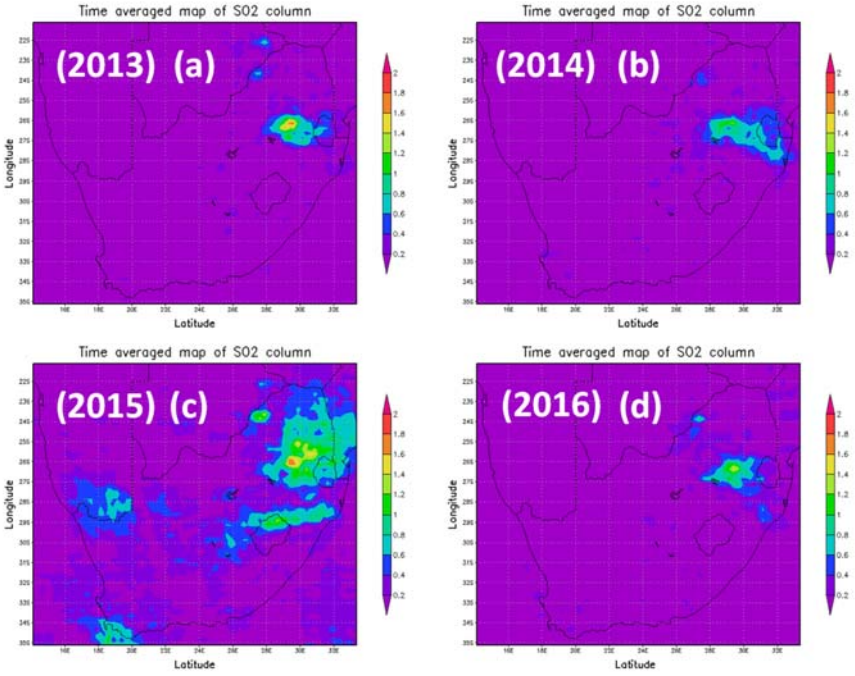

Fig. 6.2: OMI time averaged map of SO_2 column data for South Africa for 1–30 April in (a) 2013, (b) 2014, (c) 2015 and (d) 2016.

The mean monthly extinction coefficient profile using CALIPSO for April 2015 and 2014 are shown in Fig 6.3(a) and 6.3(b) respectively. The monthly mean in April 2015 reveals a general increase in the extinction coefficient with increasing altitude. In the lower part of the troposphere (ground level to ~1.8 km) there was a steady increase in the extinction coefficient. Between ~1.8 km to ~6 km there was a linear increase in the extinction coefficient from 0.01 km^{-1} to 0.36 km^{-1}. This increase in the extinction coefficient indicates an increase in the aerosols loading in that altitude range. This result illustrates that there were more aerosols in the middle troposphere than in the lower troposphere. However, in April 2014 the extinction coefficient profile was observed to be different to that of April 2015. A point to note is the negative extinction coefficient values observed at an altitude of ~0.5 km. These values are noise in the CALIPSO signal when aerosol loading is low and background noise is high (Shikwambana and Sivakumar, 2016). Between ground level and ~ 2 km there are oscillations around 0.07 km^{-1}. As was observed in April 2015, between ground level and ~ 2 km a steady increase in extinction coefficient was observed in April 2014.

There was an increase in the extinction coefficient value (from ~ 0.04 km^{-1} to ~ 0.16 km^{-1}) at an altitude of 2 km to 3 km. Thereafter a decrease in the extinction coefficient (from 0.16 km^{-1} to 0.05 km^{-1}) at altitudes of 3 km to 4 km was observed. From 4 km to 7 km an increase in extinction coefficient from ~ 0.05 km^{-1} to ~ 0.16 km^{-1} was recorded. It can be observed from both Fig 6.3a and 6.3b that there is an increase in the extinction coefficient above 4 km. This result indicates that there are aerosols that settle well in these altitudes.

The daily extinction coefficient profiles for April 2015 were examined using CALIPSO because there was an unusual distribution of SO_2 in SA compared to the other years (see Fig. 2). April 2014 extinction coefficients were also examined and compared to the April 2015 profiles. The mean extinction coefficient profiles for April 2015 from the CALIPSO level 2 aerosol products are shown in Fig 3(c). In SA the CALIPSO satellite passes either on the east (E), west (W) or centre of the country (COC). It was observed from the profiles shown in Fig 3(c) that on the east side of the country (23 and 25 April 2015) extinction coefficients were detected at altitudes (~up to 4 km) whereas in the west side (24 and 26 April

2015) altitudes up to ~6 km were observed. For the centre of the country on 28 and 30 April 2015 high altitudes up to ~8 km were observed. Altitude observation in the different parts of SA for the different days is discussed to illustrate the detection of aerosols. From the data provided by CALIPSO it is evident that the centre of the country had aerosols in the higher altitudes. This result is an important when a thorough discussion on the extinction coefficient on 28 April 2015 is done (section 6.4.4).

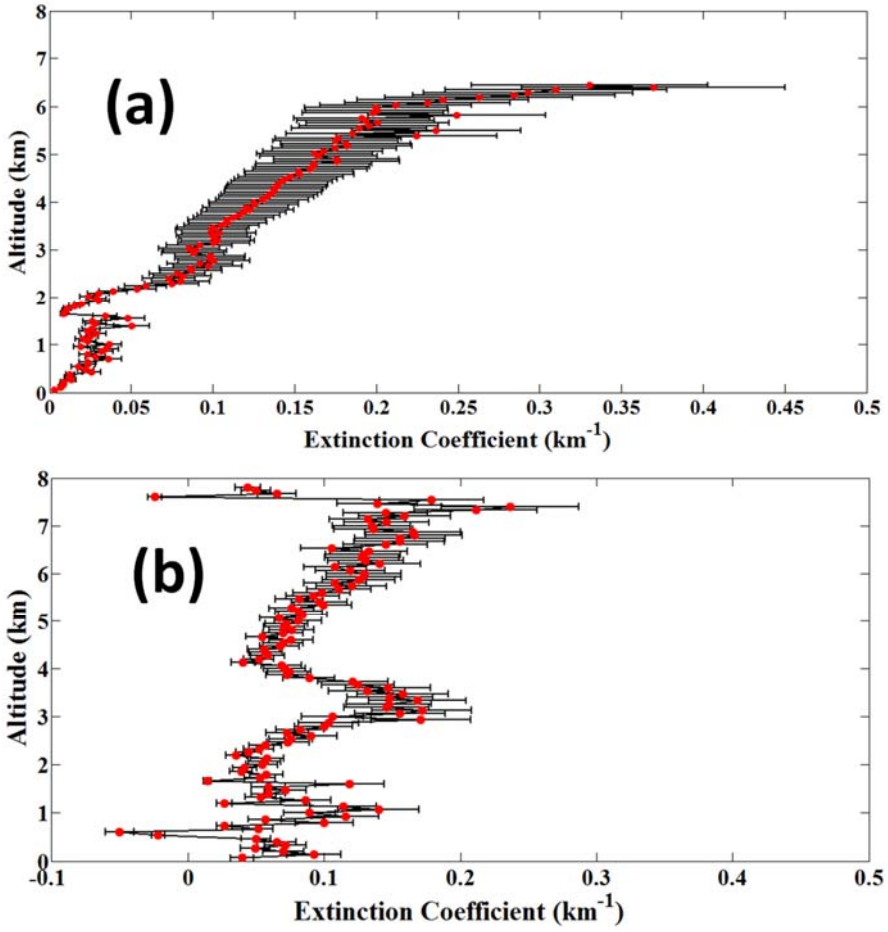

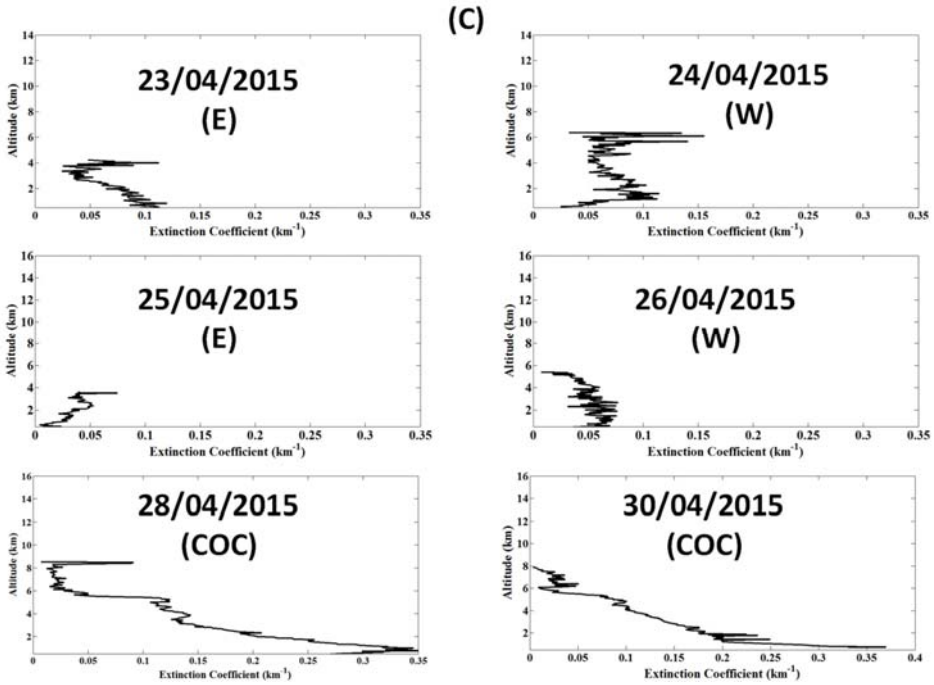

Fig. 6.3: (a) CALIPSO extinction coefficient mean monthly profiles with the standard deviation in April (a) 2015 and (b) 2014. (c) Daily CALIPSO extinction coefficient profiles over South Africa in April 2015.

6.4.2 AOD and SO_2 observations

A time averaged map of MODIS AOD (12-20 April 2015) before the volcanic eruption in Chile (the red block indicates the location of the volcano) is shown in Fig 6.4a. The time averaged AOD in the vicinity of the Calbuco volcano is ~0.1 and the lower parts of Argentina have the same averaged value of AOD = 0.1. However, after the volcanic eruption (22-29 April 2015) a small plume, with averaged MODIS AOD ~ 0.2, is observed in the Pacific Ocean (see Fig 6.4b). A huge plume with averaged MODIS AOD ranging between 0.2 and 1 is observed leaving Chile in an easterly direction. This suggests that the air masses were travelling in an easterly direction carrying and transporting the volcanic aerosols. Another medium sized plume was also observed along the east coast of Argentina and expanding in an easterly direction. The MODIS AOD fall in the range from 0.2 to 1. High AOD (0.7 to 1) values indicate very hazy sky conditions due to high concentrations of aerosols. Conversely, low values of AOD (0.1 to 0.4) indicate clear sky conditions with corresponding low concentration of aerosols.

A time averaged map of SO_2 column amount measurements, 12th to 20th April 2015, using OMI were carried out before the Calbuco volcano erupted in Chile on 22 April 2015, see Fig 6.5. Small amounts of SO_2 were observed in close proximity to the experimental site. Large scatter, in the red block, in the South Atlantic Anomaly (SAA) region over South America and the Southern Atlantic Ocean results from reduced signal-to-noise due to exposure of the low-orbiting satellite instrument to radiation and particles (Lee et al, 2009; Fioletov et al, 2016). Chuquicamata (22.31°S, 68.89°W) and Caletones (34.11°S, 70.45°W) correspond to smelters in Chile that are among the world's largest and known to produce large amounts of SO_2 aerosols (Fioletov et al, 2016) but OMI does not illustrate the same (see Fig 6.5a). Large amounts of SO_2 aerosols were observed after the eruption, see Fig 6.5b. Some SO_2 aerosols were observed travelling towards the Pacific Ocean in a westerly direction. However, Fig 6.5b suggests that large amount of SO_2 aerosols were travelling in an easterly direction and passed through Argentina and Brazil. These SO_2 aerosols were purely from the volcanic eruption.

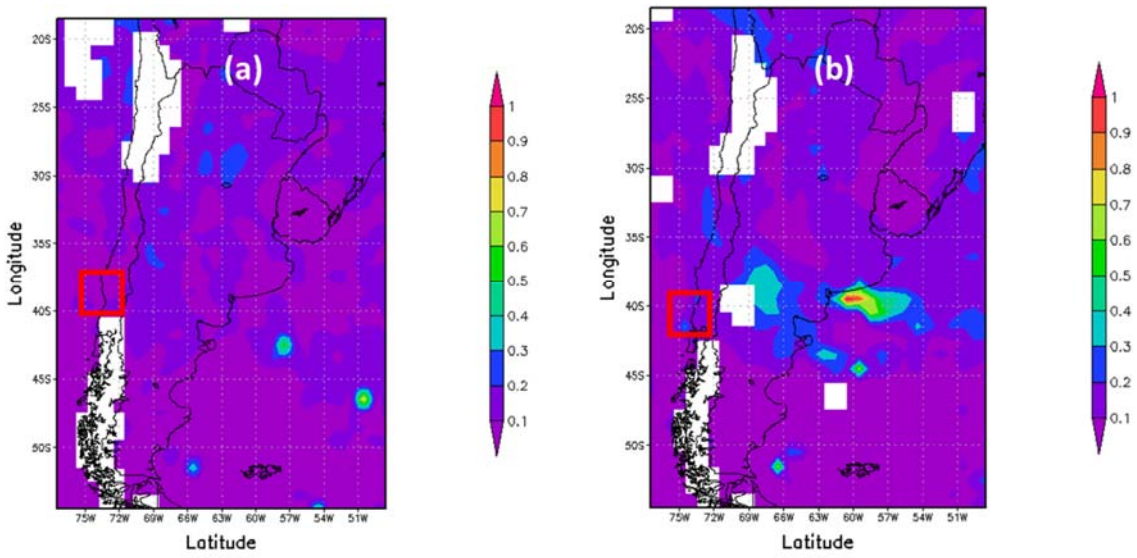

Fig. 6.4: Time averaged map of MODIS AOD in Chile on (a) 12-20 April 2015 and (b) 22-29 April 2015.

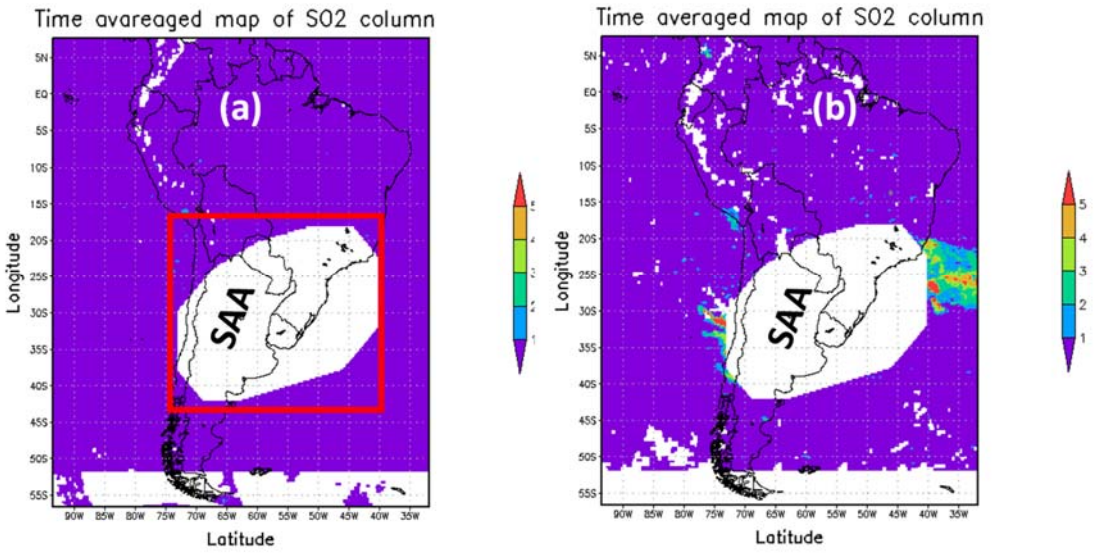

Fig 6.5: Time averaged map of SO_2 column in Chile on (a) 12-20 April 2015 and (b) 22-29 April 2015. SAA results from reduced signal-to-noise due to exposure of the low-orbiting satellite instrument to radiation and particles.

Images from the Atmospheric Infrared Sounder (AIRS) plus Ozone Mapping Profiler Suite (OMPS) further supports that the SO_2 volcanic aerosols travelled in an easterly direction after the eruption (see Fig. 6.6). On 23 and 24 April 2015 SO_2 aerosols were observed leaving Chile in an easterly direction towards Argentina and Brazil (see Fig. 6.6a and 6.6b). The SO_2 aerosols travelled over Argentina and Brazil to the Atlantic Ocean on 25 and 26 April 2015 (see Fig. 6.6c and 6.6d). However, on 27 April 2015 SO_2 aerosols were observed travelling through the eastern parts of SA. Although a high concentration of SO_2 was observed in Chile, Argentina and Brazil, SA witnessed a low concentration of SO_2. Table 6.1 summarises the quantities of the Calbuco volcanic eruption. It can be observed that there was an increase in the SO_2 mass from 119.91 kt in 23 April to 356.08 kt in 25 April 2015. This was due to the plume that was forming after the eruption. However, once the plume starts to travel and dissipates this result in a decrease of the SO_2 mass. This is observed on 26th and 27th April 2015. The area of coverage for SO_2 increased as the plume travelled from 520 500 to 3 999 100 km^2 on 23-27 April 2015.

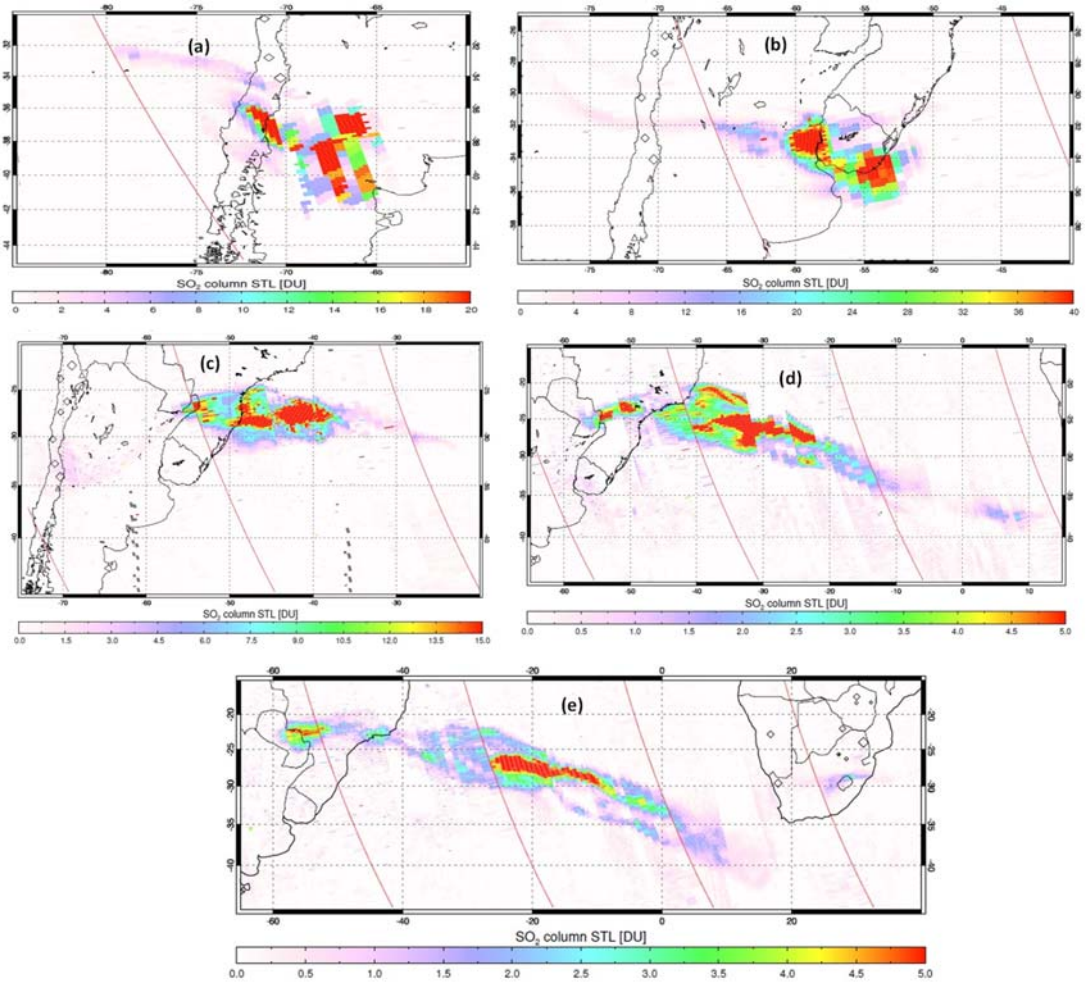

Fig. 6.6: Images of the plume coverage for volcanic SO_2 provided by AIRS + OMPS for (a) 23 April 2015 17:08-20:26 UT, (b) 24 April 2015 16:10 – 19:32 UT, (c) 25 April 2015 15:13 – 20:11 UT (d) 26 April 2015 12:39 – 19:18 UT and (e) 27 April 2015 11:43 – 18:26 UT.

Table 6.1: Quantities of the Calbuco volcano eruption provided by AIRS + OMPS

Date	**SO_2 mass (kt)**	**Area (km^2)**	**SO_2 max (DU)** **Longitude, Latitude**
23 April 2015	119.91	520 500	47.35 -71.38, -36.55
24 April 2015	316.94	1 030 531	159.11 -62.31, -32.87
25 April 2015	356.08	1 891 658	282.72 -48.00, -27.07
26 April 2015	256.23	3 034 382	20.53 -49.85, 18.45
27 April 2015	270.28	3 999 100	17.33 -20.96, -26.96

A time averaged map of SO_2 column measurements in SA before the eruption in Chile, 12-20 April 2015, is shown in Fig 6.7a. SO_2 is observed in scattered areas in the eastern parts of SA, however, there is no trace of SO_2 in the interior and western regions of SA. However, after the eruption SO_2 was observed in the western, north eastern and most predominantly interior regions of SA, see Fig 6.7b. The SO_2 aerosols observed could be from the Calbuco volcanic eruption entering SA from a south westerly direction, travelling through the interior of the country and exiting in the south eastern parts of the country towards the Indian Ocean. The north eastern region of SA (marked with a red circle in Fig 6.7b) has a large amount of industrial activities including coal burning (a by-product of which is SO_2). The SO_2 observed in this area could be primarily from such an activity but SO_2 from the eruption could also be a contributing factor. On 1-9 May 2015 (see Fig. 6.7c). SO_2 aerosols were observed in the interior and northern regions of SA. These aerosols could also be seen in the southern parts of Namibia, Botswana

and Zimbabwe. These SO_2 aerosols could be from the volcanic eruption as they were not present in Fig. 6.7a before the first SO_2 aerosols arrived in SA. It should be noted however, that these SO_2 aerosols were not as concentrated as those observed in Fig. 6.7b indicating less SO_2 aerosol loading over these areas. On 10-18 May 2015 (see Fig. 6.7d), less SO_2 aerosol loading is observed throughout SA. SO_2 loading observed in the north eastern parts of SA are from the industrial activities that occur there. SO_2 aerosols observed in the south western regions of SA could be from the volcanic eruption as there are no substantial SO_2 sources in that area. Overall SO_2 aerosols are not observed in SA and neighbouring countries indicating that these aerosols have travelled from other parts of the world.

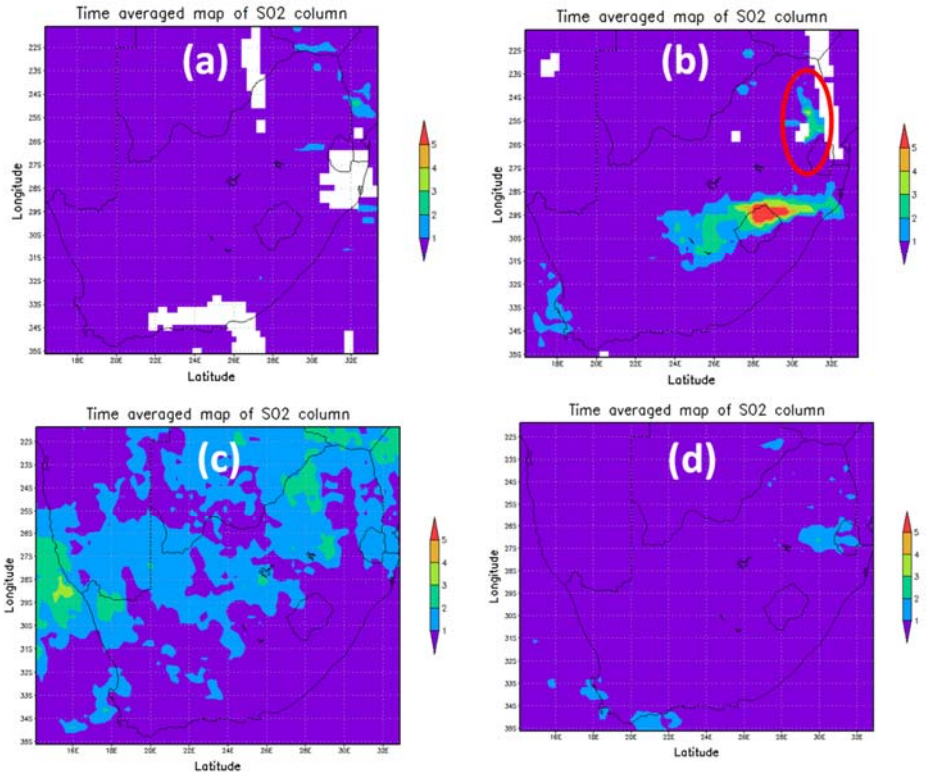

Fig. 6.7: OMI time averaged map of SO_2 column in South Africa on (a) 15-19 April 2015, (b) 23-28 April 2015, (c) 1-9 May 2015 and (d) 10-18 May 2015.

6.4.3 Forward trajectories

The 120-hour forward trajectories of air masses leaving the study site (Calbuco volcano) from 22 April 2015 were calculated using the HYSPLIT model (see Fig. 6.8). Consideration of Fig 6.7a shows that the 5 day trajectory of the 1000 m air masses transported volcanic aerosols over the Pacific Ocean. For the 2000 m air masses trajectory it was observed that the volcanic aerosols were transported through Argentina and headed towards Uruguay and Brazil. The air masses travelled via the South Atlantic Ocean towards these countries. At the end of the 5 day trajectory the 1000 and 2000 m air masses were observed at an altitude of 1000 m. At an altitude of 3000 m the air masses trajectory travelled a longer distance through Argentina, South Atlantic until the Indian Ocean with the net result that the air masses travelled between South Africa and Antarctica. The 3000 m air masses trajectory was observed at an altitude of 6000 m at the end of the 5 day simulation. The 4000 m air masses travelled the same route as the 3000 m air masses, see Fig. 6.8b. However, at the end of the 5 day trajectory simulation, these air masses were observed to have a final altitude of 7000 m. The air masses trajectory for the height at 5000 m and 6000 m transporting volcanic aerosols travelled to Brazil via Argentina and the South Atlantic Ocean (see Fig. 6.8b). Both these air masses altitudes were observed at less than 2500 m by the end of the 5 day trajectory. The 7000 m air masses transporting volcanic aerosols travelled the same route as the 4000 m and 5000 m air masses, see Fig. 6.8c. However, the 8000 m air masses (see Fig. 6.8c) transporting volcanic aerosols travelled through the interior of Chile, the Pacific Ocean and back through Chile with the final location of the volcanic aerosols being Argentina. The air masses at 8000 m were observed at a final altitude of 3000 m on completion of the 5 day trajectory simulation. The 9000 m air masses travelled a similar route as the 8000 m air masses but the air masses were observed in Chile at an altitude of 6000 m on completion of the 5 day trajectory simulation. The 10000 m air masses travelled over the Pacific Ocean, turned back and travelled through Chile and Argentina and over the South Atlantic Ocean. These air masses were observed at the end of the 5 day trajectory simulation to have an altitude of 6500 m. The 11000 m air masses transporting volcanic aerosols travelled over the Pacific

Ocean and reached the northern parts of Chile at an altitude of 4500 m on completion of the 5 day trajectory simulation. The air masses at 12000 m travelled through Argentina, Brazil, and then South Atlantic Ocean, passed through SA and reached the Indian Ocean on completion of the 5 day trajectory simulation with a final altitude of 8000 m (see Fig. 6.8d). It is therefore observed that volcanic aerosols entered the south western region of SA on the 25th of April 2015, travelled through the interior of SA and exited the country in the south east.

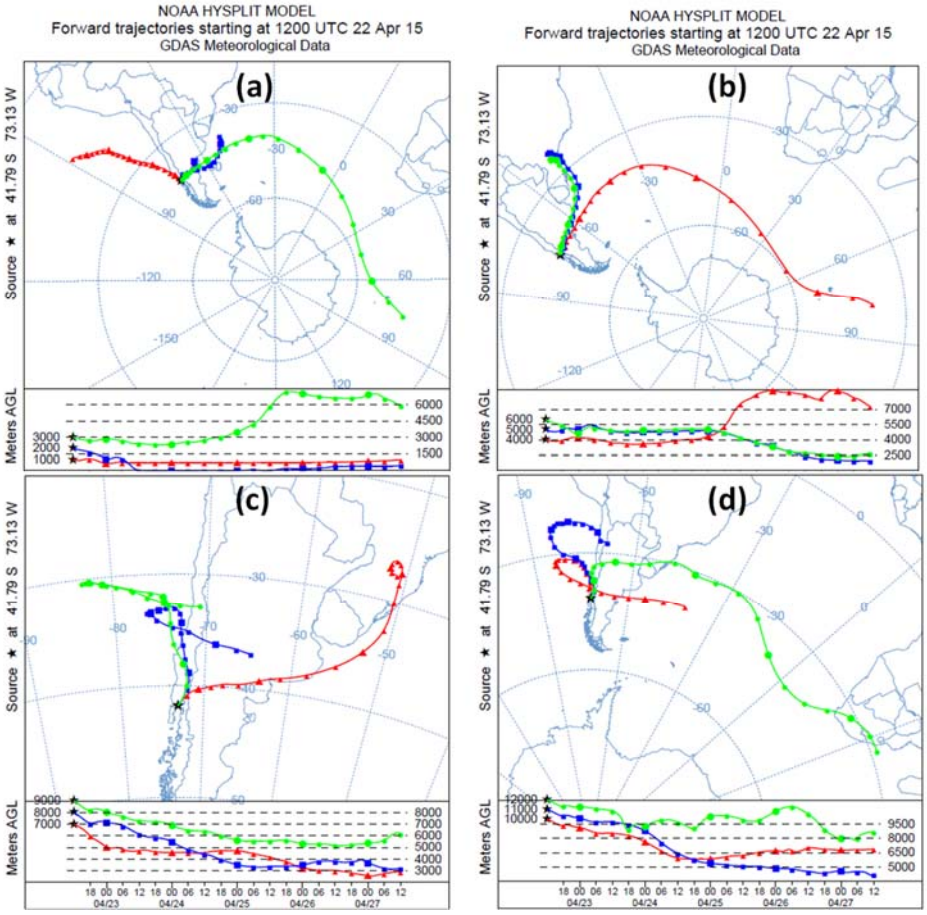

Fig. 6.8: Forward trajectories from Calbuco volcano starting on 22 April to 28 April 2015 for altitude ranges: (a) 1000 – 3000 m, (b) 4000 – 6000 m, (c) 7000 – 9000 m and (d) 10000 – 12000 m.

6.4.4 CALIPSO observations

On 28 April 2015, see Fig 6.9a, strong extinction coefficient signals (~0.35 km^{-1}) are observed in the lower part of the atmosphere (~1 km) which could be the result of anthropogenic aerosols. However, there is a decrease in the extinction coefficient values with an increase in altitude. This indicates that there are less anthropogenic aerosols in the upper atmosphere. At 8 km there is a sudden increase in the value of the extinction coefficient to (~0.09 km^{-1}) indicating an increase in aerosols loading. This sudden increase could be due to SO_2 aerosols from the volcanic eruption. This is further supported by the forward trajectory from the HYSPLIT model (see Fig 6.8d) showing the air masses arriving in SA at an altitude of ~8 km. On 6 May 2015, see Fig 6.9(b), low values of extinction coefficient profile are observed in the low troposphere which is indicative of low aerosol loading. However, the negative extinction coefficient values are found to be noisy in the CALIPSO signal when aerosol loading is low and background noise is high (Shikwambana and Sivakumar, 2016). By comparison, the highest extinction coefficient (~0.2 km^{-1}) is observed around 6 km. The extinction coefficient values then start to decrease with increasing height up to an altitude of ~12 km. The aerosols at this altitude could be SO_2 aerosols from the Calbuco volcanic eruption. On 7 May 2015, see Fig 6.9c, high values of extinction coefficients (~0.3 km^{-1}) are observed at low altitudes and a decrease in the values of extinction coefficients with increasing altitude is noted. As seen in Fig 6.9b, a high extinction coefficient (~0.45 km^{-1}) was observed at 6 km and the values of extinction coefficients begun decreasing with increasing altitude. The highest aerosols were observed at an altitude of ~ 12 km and are likely to be SO_2 aerosols from the Calbuco volcanic eruption. However, the values of extinction coefficients values at 12 km are very low (~0.03 km^{-1}) indicating that there is a low number of SO_2 aerosols at that altitude. The extinction coefficient profile on 9 May 2015 is similar to that observed in Fig 6.9b with the difference being the altitude that the SO_2 aerosols are observed. SO_2 aerosols were observed at an altitude of ~ 10 km in 9 May 2015.

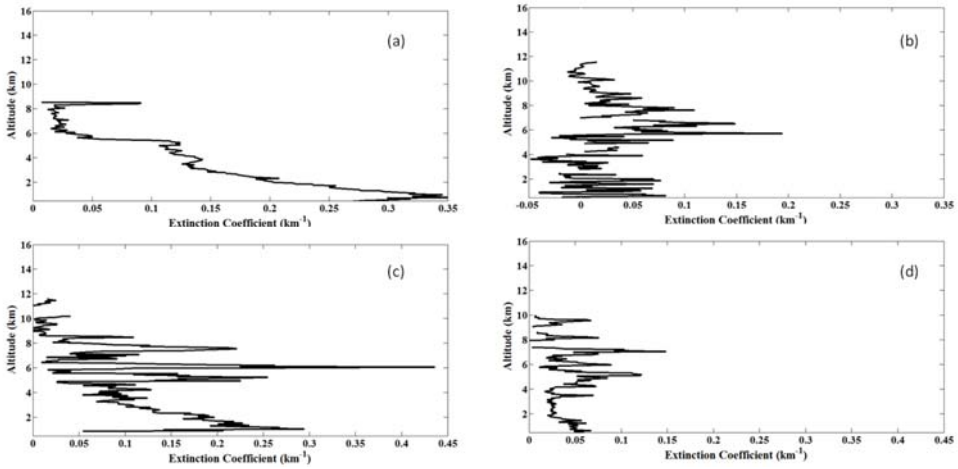

Fig. 6.9: Extinction coefficient profiles over South Africa over the different days after the Calbuco volcanic eruption. (a) 28/04/2015, (b) 06/05/2015, (c) 07/05/2015 and (d) 08/05/2015.

Fig. 6.10a shows the colour coded time-height total backscatter images at 532 nm acquired by CALIPSO on 28 April 2015. The red block indicates that the back scatter observed at an altitude of ~ 8 km travelling through SA might be due to aerosols or clouds. The yellow-red colour coding indicates that the aerosols or cloud loading is moderate. However, from the vertical Feature Mask (VFM) (see Fig 6.10b) it is observed that the backscatter could be classified as a mixture if cloud and aerosols are present. From the aerosol type in CALIPSO these aerosols and cloud mixture were classified as polluted dust. Presence of polluted dust aerosols corresponds with the presence of SO_2 (Mahmood et al, 2016). This indicates that these SO_2 aerosols could be from the Calbuco volcanic eruption in Chile.

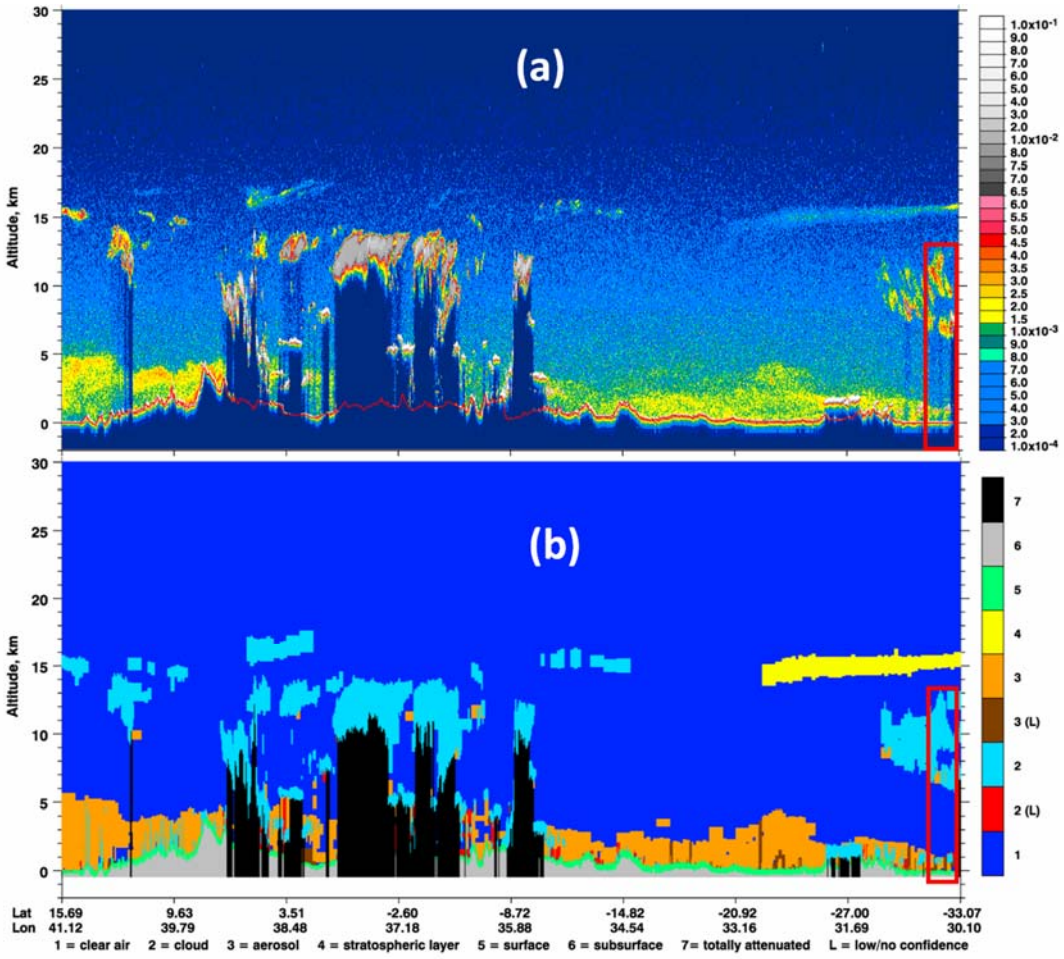

Fig 6.10: CALIPSO images showing the (a) height-time-colour map of CALIPSO-derived total attenuated backscatter at 532 nm and (b) Vertical Feature Masks Image for 28 April 2015

6.5 Conclusion

During a volcanic eruption different types of substances are released onto the surface of the earth and into the atmosphere as volcanic aerosols. The main focus of this study was to determine if South Africa was impacted by volcanic aerosols as a result of an eruption in Chile. One way of accomplishing this was to track SO_2 aerosols, which are known to be a by-product of volcanic eruptions. A case study of the Calbuco volcanic eruption, in Chile (22 April 2015) was then completed. It was observed using the HYSPLIT model, that the air masses leaving Calbuco (22 April 2015) were at an altitude of 12000 m and travelled through SA

at an altitude of 8000 m on 28 April 2015. MODIS and OMI both showed AOD and SO_2 aerosols leaving Chile in an easterly direction. Furthermore, OMI showed SO_2 aerosols travelling over SA on 28 April 2015 which is in agreement with the HYSPLIT model. The extinction coefficient profile and total backscatter height-time-colour map from CALIPSO also confirmed the presence of aerosols at a height of 8 km on 28 April 2015. The VFM and aerosol type from CALIPSO were used to classify the particles as a mixture of cloud and aerosol polluted dust which corresponds to the presence of SO_2. With these measurements it can be concluded that the SO_2 aerosols travelled from Chile to SA. Extinction coefficient profiles observed on 06-09 May 2015 further suggests that these aerosols were still present on those days.

References

Andersson S. M., Martinsson B. G., Vernier J.-P., Friberg J., Brenninkmeijer C. A. M., Hermann M., van Velthoven P. F. J., Zahn A., 2015. Significant radiative impact of volcanic aerosol in the lowermost stratosphere, Nature Communication., 6:7692 doi: 10.1038/ncomms8692

Bitar L, Duck T. J., Kristiansen N. I.,Stoh A., Beauchamp S., 2010. Lidar observations of Kasatochi volcano aerosols in the troposphere and stratosphere, Journal of Geophysical Research., 115, D00L13, doi:10.1029/2009JD013650

De Vries M. J. M. P., DörnerS.,Pukite J., Hörmann C., Fromm M. D., Wagner T., 2014. Characterisation of a stratospheric sulfate plume from the Nabrovolcano using a combination of passive satellite measurements in nadir and limb geometry, Atmospheric Chemistry and Physics, 14, 8149–8163. doi:10.5194/acp-14-8149-2014

Fioletov V. E., McLinden C. A., Krotkov N., Li C., Joiner J., Theys N., Carn S., Moran M. D., 2016. A global catalogue of large SO_2 sources and emissions derived from the Ozone Monitoring Instrument, Atmospheric Chemistry and Physics, 16, 11497–11519

Ialongo I., Hakkarainen J., Kivi R., Anttila P., Krotkov N. A., Yang K., Li C., Tukiainen S., Hassinen S.,Tamminen J., 2015. Comparison of operational satellite SO_2 products with ground-based observations in northern Finland during the Icelandic Holuhraun fissure eruption, Atmospheric Measurement Techniques., 8, 2279–2289. doi:10.5194/amt-8-2279-2015

Kittaka C., Winker D. M., Vaughan M. A., Omar A., Remer L. A., 2011. Intercomparison of column aerosol optical depths from CALIPSO and MODIS-Aqua, Atmospheric Measurement Techniques., 4, 131–141. doi:10.5194/amt-4-131-2011

Krotkov N. A., McLinden C. A., Li C.,Lamsal L. N., Celarier E. A., Marchenko S. V., Swartz W. H., Bucsela E. J., Joiner J., Duncan B. N., Boersma K. F,

Veefkind J. P.,Levelt P. F., Fioletov V. E, Dickerson R. R., He H., Lu Z, Streets D. G., 2016. Aura OMI observations of regional SO_2 and NO_2 pollution changes from 2005 to 2015, Atmospheric Chemistry and Physics., 16, 4605–4629. doi:10.5194/acp-16-4605-2016

Kuebbeler M.,Lohmann U.,Feichter J., 2012. Effects of stratospheric sulfate aerosol geo-engineering on cirrus clouds, Geophysical Research Letters, 39, L23803, 1-5. doi:10.1029/2012GL053797

Langmann B., 2014. On the Role of Climate Forcing by Volcanic Sulphate andVolcanic Ash, Advances in Meteorology, Article ID 340123, 17 pages. doi.org/10.1155/2014/340123

Lee C., Martin R. V., van Donkelaar A., O'Byrne G.,Krotkov N., Richter A., Huey L. G.,Holloway G. S., 2009. Retrieval of vertical columns of sulfur dioxide from SCIAMACHY and OMI: Air mass factor algorithm development, validation, and error analysis, Journal of Geophysical Research., 114, D22303.doi:10.1029/2009JD012123

Levy R. C.,Mattoo S., Munchak L. A., Remer L. A., Sayer A. M., Patadia F., Hsu N. C., 2013. The Collection 6 MODIS aerosol products over land and ocean, Atmospheric Measurement Techniques., 6, 2989–3034. doi:10.5194/amt-6-2989-2013

Li C., Krotkov N. A., Carn S., Zhang Y.,Spurr R. J. D., Joiner J., 2016. New-generation NASA Aura Ozone Monitoring Instrument (OMI) volcanic SO_2 dataset: Algorithm description, initial results, and continuation with the Suomi-NPP Ozone Mapping and Profiler Suite (OMPS), Atmospheric Measurement Techniques and Discuss., doi:10.5194/amt-2016-221, 2016

Liu Z., Vaughan M., Winker D., Kittaka C., Getzewich B., Kuehn R., Omar A., Powell K., Trepte C., Hostetler C., 2009. The CALIPSO Lidar Cloud and Aerosol Discrimination: Version 2 Algorithm and Initial Assessment of Performance, Journal of Atmospheric and Oceanic Technology, 26, 1198-1213. doi: 10.1175/2009JTECHA1229.1

Mahmood I., Shazad M.I., Iqbal M.F., Ullah K., Waqas A. and Kidwai A.A., 2016. Satellite based detection of volcanic SO_2 over Pakistan, Global NEST Journal, 18, 591-598.

Miffre A., David G., Thomas B., RairouxP., Fjaeraa A. M., Kristiansen N. I.,Stohl A., 2012. Volcanic aerosol optical properties and phase partitioning behavior after long-range advection characterized by UV-Lidar measurements, Atmospheric Environment., 48, 76-84. doi:10.1016/j.atmosenv.2011.03.057

Muthers S., Arfeuille F., Raible C. C., Rozanov E., 2015. The impacts of volcanic aerosol on stratospheric ozone and the Northern Hemisphere polar vortex: separating radiative-dynamical changes from direct effects due to enhanced aerosol heterogeneous chemistry, Atmospheric Chemistry and Physics., 15, 11461–11476. doi:10.5194/acp-15-11461-2015

Pöschl U., 2005. Atmospheric Aerosols: Composition, Transformation, Climate and Health Effects, Angewandte Chemie International Edition 44, 7520–7540. DOI: 10.1002/anie.200501122

Pitari G., Cionni I., Di Genova G., Visioni D., Gandolfi I., Mancini E., 2016. Impact of Stratospheric Volcanic Aerosols onAge-of-Air and Transport of Long-Lived Species, Atmosphere, 7, 149; doi:10.3390/atmos7110149

Pitari G., Di Genova G., Mancini E., Visioni D., Gandolfi I.,Cionni I., 2016. Stratospheric Aerosols from Major Volcanic Eruptions: A Composition-Climate Model Study of the Aerosol Cloud Dispersal and e-folding Time, Atmosphere, 7, 75; doi:10.3390/atmos7060075

Robock A., 2000. Volcanic eruptions and climate, Reviews of Geophysics, 38, 191-219

Romero J.E., Morgavi D.,ArzilliF., DagaR., Caselli A.,ReckziegelF.,ViramonteJ.,Díaz-Alvarado J.,PolacciM., Burton M., Perugini D., 2016. Eruption dynamics of the 22–23 April 2015 Calbuco

Volcano (Southern Chile): Analyses of tephra fall deposits, Journal of Volcanology and Geothermal Research., 317, 15–29

Ruiz-Arias J. A., Dudhia J., Gueymard C. A.,Pozo-V´azquez D, 2013. Assessment of the Level-3 MODIS daily aerosol optical depth in the context of surface solar radiation and numerical weather modeling, Atmospheric Chemistry and Physics, 13, 675–692. doi:10.5194/acp-13-675-2013

Safarpour S., Abdullah K, Lim K. S., Dadras M., 2014. Accuracy assessment of Terra-MODIS aerosol optical depth retrievals, IOP Conf. Series: Earth and Environmental Science, 20, 1-8. doi:10.1088/1755-1315/20/1/012059

Sawamura P., Vernier J. P., Barnes J. E.,Berkoff T. A., Welton E. J., Alados-Arboledas L.,Navas-Guzman F., Pappalardo G., Mona L., Madonna F., Lange D., Sicard M., Godin-Beekmann S., Payen G., Wang Z., Hu S., Tripathi S. N., Cordoba-Jabonero C., Hoff R. M., 2012. Stratospheric AOD after the 2011 eruption of Nabro volcano measured by lidars over the Northern Hemisphere, Environmental Research Letters, 7, 034013. doi:10.1088/1748-9326/7/3/034013

Schmidt A., Leadbetter S., Theys N., Carboni E., Witham C. S., Stevenson J. A., Birch C. E., Thordarson T., Turnock S., Barsotti S., Delaney L., Feng W., Grainger R. G., Hort M. C., Höskuldsson A., Ialongo I., Ilyinskaya E., Jóhannsson T., Kenny P., 2015. Satellite detection, long-range transport, and air quality impacts of volcanic sulfur dioxide from the 2014–2015 flood lava eruption at Bárðarbunga (Iceland), Journal of Geophysical Research. Atmospheres, 120, 9739–9757, doi:10.1002/2015JD023638

Shikwambana L., Sivakumar V., 2016. Observation of Clouds Using the CSIR Transportable LIDAR: A Case Study over Durban, South Africa, Advances in Meteorology, Article ID 4184512, 9 pages. doi:10.1155/2016/4184512

Shin D., Müller D., Lee K., Shin S., Kim Y. J., Song C. K., Noh Y. M., 2015. Lidar observations of Nabro volcano aerosol layers in the stratosphere

over Gwangju, Korea, Atmospheric Chemistry and Physics Discussions., 15, 1171–1191. doi:10.5194/acpd-15-1171-2015

Stein A. F., Dra xler R. R., Rolph G. D., Stunder B. J. B., Cohen M. D., Ngan F., 2015. NOAA'S transport and dispersion modeling system, Bulletin of the American Meteorological Society, doi:10.1175/BAMS-D-14-00110.1

Vaughan M., Young S., Winker D., Powell K., Omar A., Liu Z., Hu Y., Hostetler C., Fully automated analysis of space-basedlidar data: an overview of the CALIPSO retrieval algorithms and data products, Proceedinds of SPIE Vol. 5575, 16-30. doi: 10.1117/12.572024

Vernier J.-P., Thomason L. W., Pommereau J.-P., Bourassa A.,Pelon J., Garnier A., Hauchecorne A., Blanot L.,Trepte C., Degenstein D., Vargas F., 2011. Major influence of tropical volcanic eruptions on the stratospheric aerosol layer during the last decade, Geophysical Research Letters, 38, L12807, doi:10.1029/2011GL047563

Winker D. M., Pelon J., Coakley Jr. J. A., Ackerman S. A., Charlson R. J., Colarco P. R., Flamant P., Fu Q., Hoff R. M., Kittaka C., Kubar T. L., Le Treut H., Mccormick M. P.,Mégie G., Poole L., Powell K., Trepte C., Vaughan M. A., Wielicki B. A., 2010. The CALIPSO Mission: A Global 3D View of Aerosols and Clouds, Bulletin of the American Meteorological Society, doi:10.1175/2010BAMS3009.1

Winker D. M., Tackett J. L., Getzewich B. J., Liu Z., Vaughan M. A., Rogers R. R., 2013. The global 3-D distribution of tropospheric aerosols as characterized by CALIOP, Atmospheric Chemistry and Physics, 13, 3345–3361. doi:10.5194/acp-13-3345-2013

Chapter 7

Summary and Future work

7.1 Summary

In Chapter 1 the motivation and objectives of this study are given. In Chapter 2 an in-depth background on the structure of the atmosphere, atmospheric aerosols, scattering theory and remote sensing are given. The instruments used in this study are discussed in Chapter 3. Measurements were carried out in the different parts of South Africa using the CSIR mobile LIDAR system, MODIS, CALIPSO, the HYSPLIT model, the MERRA-2 model, the GOCART model and OMI.

In Chapter 4, the main objective was to study the optical properties of clouds using LIDAR and satellite. The measurements were carried out in Durban on 20 – 22 November 2012 using the CSIR LIDAR and CALIPSO data. The key findings are listed:

- Low cloud layers showed high extinction coefficient values ranging from 0.0009 m^{-1} to 0.0044 m^{-1}.
- High cloud layers showed low extinction coefficient values ranging between 0.000001 to 0.000002 m^{-1}.
- The vast difference in the extinction coefficient suggest that there are remarkable differences in optical characteristics between low and high level clouds.
- Comparable LIDAR and CALIPSO data was available on 20 and 22 November 2012 and indicated that the CALIPSO could observe high level clouds while the CSIR LIDAR could not.
- The CSIR LIDAR and CALIPSO complement each other well to describe the cloudy condition.

The main aim of Chapter 5 was to study the aerosol optical characteristics and distribution of various aerosols in South Africa using LIDAR, satellite data and models. The main findings from MERRA-2 were as follows:

- Seasonal studies conducted revealed that BC aerosols were more dominant in the eastern parts of SA during spring and less dominant in autumn.
- Sulphate aerosols were more dominant in the eastern parts of SA during summer and less dominant in winter.
- Dust aerosols were more dominant in the north-western parts of SA during summer and less dominant in winter.
- Sea salt aerosols were more dominant in the coast area, Indian Ocean and north eastern parts of SA during summer and spring, and less dominant during autumn and winter.

Furthermore in Chapter 5, the main findings from the GOCART model and CSIR LIDAR were as follows:

- Sulphates were the dominant contributing factor towards total anthropogenic AOD when compared with contributions due to dust and BC.
- The highest Sulphate AOD was observed in summer and the lowest Sulphate AOD was observed in winter.
- The high sulphate concentration in summer was as a result of an increase in relative humidity which favours the production of sulphates.
- The CSIR mobile LIDAR indicated a layer of aerosols in the morning which decreased during the day.
- CALIPSO observations were found to be in good agreement with the measurements by the CSIR mobile LIDAR.
- CALIPSO classified those aerosols as polluted dust and smoke.

The objective of Chapter 6 was to study aerosols being transported into South Africa. A case study of the Calbuco volcano eruption was carried out to illustrate the transport of aerosols from one continent to another. The main findings from this study were as follows:

- MODIS and OMI+AIRS showed AOD SO_2 aerosols leaving Chile in an easterly direction.
- OMI further showed SO_2 aerosols travelling over SA on 28 April 2015, which was in agreement with the HYSPLIT model.

- The extinction coefficient profile and total backscatter height-time-colour map from CALIPSO also confirmed the presence of aerosols at a height of 8 km on 28 April 2015.
- The VFM and aerosol type from CALIPSO were used to classify the particles as a mixture of cloud and aerosols polluted dust, which corresponds with presence of SO_2.

7.2 Future work

The University of KwaZulu-Natal currently has two LIDAR systems in operation, a fixed system and a portable 2-D scan system. The fixed LIDAR system operates with two acquisition channels, a high altitude channel (channel A) and a low altitude channel (channel B). Channel A is used to study parameters such as temperature and aerosols extinction coefficient profiles in the stratosphere. On the other hand, channel B can be used to study low altitude clouds and aerosol optical depth in the troposphere. The portable 2-D scan LIDAR system is primarily aimed for atmospheric backscatter measurements in the lower troposphere. One of the focus of the future is to run both LIDAR systems simultaneously daily for a year or so to retrieve data that could be used for seasonal studies. This data could be used with models and satellite data to study the atmospheric parameters in the region.